5-1-2023

SYNTHESIS, SINTERING, AND ELECTRONIC CONDUCTIVITY STUDIES OF MEDIUM- AND HIGH-ENTROPY PEROVSKITE OXIDES

Sai Ram Gajjala
Southern Illinois University Carbondale, sairam.gajjala@gmail.com

SYNTHESIS, SINTERING, AND ELECTRONIC CONDUCTIVITY STUDIES OF MEDIUM- AND HIGH-ENTROPY PEROVSKITE OXIDES

by

Sai Ram Gajjala

B.Tech., Jawaharlal Nehru Technology University Hyderabad, 2014
M.S., Southern Illinois University Carbondale, 2017

A Dissertation
Submitted in Partial Fulfillment of the Requirements for the
Doctor of Philosophy Degree

College of Engineering, Computing, Technology, and Mathematics
in the Graduate School
Southern Illinois University Carbondale
May 2023

DISSERTATION APPROVAL

SYNTHESIS, SINTERING, AND ELECTRONIC CONDUCTIVITY STUDIES OF MEDIUM-
AND HIGH-ENTROPY PEROVSKITE OXIDES

by

Sai Ram Gajjala

A Dissertation Submitted in Partial

Fulfillment of the Requirements

for the Degree of

Doctor of Philosophy

in the field of Engineering Science

Approved by:

Dr. Rasit Koc, Chair

Dr. Peter Filip

Dr. Emmanuel Nsofor

Dr. Geoffrey Swift

Dr. Sabrina Nilufar

Dr. Jebaraj Asirvatham

Graduate School
Southern Illinois University Carbondale
April 5, 2023

AN ABSTRACT OF THE DISSERTATION OF

Sai Ram Gajjala, for the Doctor of Philosophy degree in Engineering Science, presented on April 5, 2023, at Southern Illinois University Carbondale.

TITLE: SYNTHESIS, SINTERING, AND ELECTRONIC CONDUCTIVITY STUDIES OF MEDIUM- AND HIGH-ENTROPY PEROVSKITE OXIDES

MAJOR PROFESSOR: Dr. Rasit Koc

The application of the entropy concept to stabilize oxide systems opens the possibility of discovering new materials with unique structural and functional properties. High-entropy alloys and oxides, which are based on the entropy stabilization concept and composed of multi-principal elements, have the potential to tailor structural and functional properties to meet specific needs. The study of lanthanum-based perovskite materials that benefit from the entropy stabilization approach is a promising area of research.

However, the inherent randomness of multi-principal elements presents new challenges, making it difficult to predict their behavior. To understand these difficulties, we have initiated a methodical investigation of La-based medium- and high-entropy perovskite oxides. This study focuses on the synthesis, characterization, sintering mechanism, and electrical conductivity properties of nine $La_{1-x}Ca_x(A_{1/3}, B_{1/3}, C_{1/3})O_3$ medium-entropy perovskite oxide systems (A, B, and C = three combination of Cr or Co or Fe or Ni or Mn) and one $La_{1-x}Ca_x(Cr_{0.2}Co_{0.2}Fe_{0.2}Ni_{0.2}Mn_{0.2})O_3$ high-entropy perovskite oxide system (for x = 0.1 to 0.3). This research aims to provide better understanding of: (1) synthesis process, (2) temperature of single-phase formation, (3) the impact of various combinations of multiple B-site transitional elements and Ca doping on crystal structure, and microstructure (4) sintering mechanism and (5) electrical conductivity properties.

ACKNOWLEDGMENTS

DEDICATION

I would like to dedicate this dissertation to my loving wife, my family, including parents,

brother, and in-laws, as well as my sisters- and brother-in-law, and my church family at Calvary

Campus Church for their unwavering belief in and support of me. Lastly, I offer my deepest

gratitude to my Heavenly Father, who is my savior, and for making this dissertation possible.

PREFACE

This dissertation is comprised of ten chapters. The first chapter provides a background on low-, medium-, and high-entropy perovskites and reviews previous research on their applications. The second and third chapters discuss the synthesis and characterization of medium- and high-entropy perovskite oxides (M-HEPO). The fourth chapter provides a theoretical prediction of the crystal structure, using the Goldschmidt tolerance factor, as well as the actual crystal structures of M-HEPO powders. The fifth chapter presents the initial results of the first synthesized $La_{1-x}Ca_x(Cr_{1/3}Fe_{1/3}Ni_{1/3})O_3$ medium-entropy perovskite oxide. The sixth chapter examines the impact of substituting M = Co, Fe and Ni in $La_{1-x}Ca_x(Cr_{1/3}Mn_{1/3}M_{1/3})O_3$, focusing on synthesis, crystal structure, microstructure and electrical conductivity. The seventh chapter investigates the microstructure and electrical conductivities of $La(Cr_{1/3}Fe_{1/3}Co_{1/3})O_3$, $La(Cr_{1/3}Ni_{1/3}Co_{1/3})O_3$, and $La(Fe_{1/3}Ni_{1/3}Co_{1/3})O_3$ MEPO. The eighth chapter explores the effect of doping Ni and Co in the MEPO systems of $La_{1-x}Ca_x(Fe_{1/3}Mn_{1/3}Ni_{1/3})O_3$, and $La_{1-x}Ca_x(Co_{1/3}Fe_{1/3}Mn_{1/3})O_3$. The ninth chapter provides firsthand information about development and characterization of calcium-doped $La(Cr_{0.2}Co_{0.2}Fe_{0.2}Mn_{0.2}Ni_{0.2})O_3$ HEPO system. The tenth chapter concludes with final remarks and provides an outlook on the future potential of M-HEPOs.

TABLE OF CONTENTS

LIST OF TABLES

vii

viii

LIST OF FIGURES

LIST OF ABBREVIATIONS

ABBREVIATION	DEFINATION
CGO	Gadolinium-Doped Ceria
EC	Electrical conductivity
EDTA	Ethylenediamine tetra-acetic acid
EDS OR EDXS	Energy-dispersive X-ray spectroscopy
GSTF	Gold Schmidt tolerance factor
HEO	High-entropy oxides
HEPO	High-entropy perovskite oxides
MEPO	Medium-entropy perovskite oxides
PPM	Polymerizable precursor method
SEM	Scanning electron microscopy
SOEC	Solid oxide electrolysis cell
SOFC	Solid oxide fuel cell
TD	Theoretical density
TEC	Thermal expansion coefficient
TM	Transitional Metals
XPS	X-ray photoelectron spectroscopy
XRD	X-ray diffraction
YSZ	Yttria-stabilized zirconia

CHAPTER 1

BACKGROUND AND LITERATURE REVIEW

1.1 An overview of high-entropy materials

This section provides a background on the medium- and high-entropy perovskite oxides (HEPO), which is the focus of our research. In 2004, the discovery of high-entropy alloys (HEA) was made. These alloys, also known as multi-principal element alloys or multi-component materials, bring a new concept to modern material science. This concept involves having five or more principal elements in nearly equal atomic proportions [1, 2].

There are several definitions used to describe HEAs. Yeh and team proposed two definitions. The first definition is based on the elemental composition and states that a material is considered HEA if it contains more than five elements in near equal ratios, each element with an atomic concentration between 5% and 35%. The second definition is based on configurational entropy (S-conf), where a multi-component equiatomic alloy is defined as HEA if its configurational entropy is $\geq 1.5R$ (R is the ideal gas constant), regardless of its phase purity at room temperature. In this research, the term "high-entropy" is used for solid solutions that have S-conf $\geq 1.5R$, based on the definitions and guidelines proposed by Yeh and group [1, 3, 4].

The study by Rost et al., demonstrated the feasibility of synthesizing five equiatomic ratios of cations in a single-phase oxide, which they referred to as the "entropy stabilized oxide" due to its structural stability through entropy [5]. Further research by Berarden et al., found that the functional properties of high-entropy oxides were superior to those of binary or doped oxide solutions. As high-entropy oxides occupy the uncharted center of a multinary phase diagram, there is potential for unexpected results [6–15].

The entropy stabilization concept involves stabilizing a single-phase crystal structure or obtaining a crystal structure with a single phase by increasing its configurational entropy (S-conf). This is typically achieved by adding more cations to the same sublattice sites or by increasing the formation temperature [14]. As more cations are added to the system, the S-conf increases and reaches its maximum when all elements are present in equiatomic ratios. Materials with five elements can have a maximum S-conf of 1.61R.

According to Murty and team, a multi-component material with S-conf > 1.5R as high-entropy, with S-conf between 1.5R and 1R as medium-entropy, and S-conf less than 1R as low-entropy [4]. High temperatures can be favorable in forming medium- or high-entropy systems. When S-conf >1.5R, a single-phase system is usually formed. However, previous research [3, 4], has shown that S-conf > 1.5R does not always guarantee the formation of a single-phase system. This concept can be used to precisely tailor the functional characteristics of materials [4]. Equation 1 is used to calculate S-conf:

$$S - conf = -R\left[\left(\sum_{i=1}^{N} x_i \ln x_I\right)_{cation} + \left(\sum_{j=1}^{M} x_j \ln x_j\right)_{anion}\right] \quad (1)$$

Where x_i and x_j are the mole fractions of cations and anions present in the system, R is the universal gas constant, and N and M are the numbers of cations and anions, respectively.

Since 2015, various new compositions of high-entropy oxides (HEOs) have been studied and investigated [5]. These studies have shown improved functional properties, such as a higher dielectric constant [6], decreased thermal conductivity [8], and enhanced ionic conductivity at low temperatures [7]. In the consequent years, the concept of multi-component materials was expanded to include diborides, carbides, sulfides, and fluorides [5, 10–12]. The recently developed HEOs are now used in energy production as anode electrodes in lithium cells [12]. HEOs have the advantage of having multiple elements and structural diversity, making them

2

suitable for synthesizing various combinations of solid solutions and studying their functional properties. The entropy stabilization concept is rapidly growing in other areas, and elevated temperature energy generation devices, such as solid oxide fuel cell components, can utilize this concept [13].

In 2018, Jiang et al. conducted the first study on high-entropy perovskite oxide (HEPO) materials with a traditional ABO_3 perovskite cubic structure ($Pm\overline{3}m$). They evaluated 13 different compositions, with Ba and Sr cations on the A-site and a five-element combination of Ce, Gd, Hf, Mn, Sn, Y, and Zr on the B-site. The study found a correlation between the Goldschmidt tolerance factor, t, and the possibility of achieving a single-phase solid solution with 't' values ranging from 0.97 to 1.03 [9].

In the same year, Sarkar et al., synthesized 11 different HEPOs by simultaneously doping A and B sites. They chose cations for the A-site from Gd, La, Nd, and Sm and cations for the B-site from Cr, Co, Fe, Ni, and Mn. They prepared the following compositions of (5A-site)(Cr or Co)$O_{3-\delta}$, (Gd or La)(5B-site) $_{3-\delta}$ and (5A-site)(5B-site) $_{3-\delta}$ using nebulized spray pyrolysis (NSP) method and achieved six single-phase perovskites out of 11 compositions with an orthorhombic perovskite (Pbnm) structure. These single-phase solid solutions corresponded well with the theoretical Goldschmidt tolerance factor, varying between 0.9 and 0.96, and showed entropic stabilization in the studied compositions. The magnetic properties of these single-phase compositions were later studied, with a focus on magnetic ordering temperature, and found to be strongly correlated with the Goldschmidt tolerance factor, demonstrating that the properties of HEPOs can be tailored through cation selection [16].

In 2020, Dabrowa and team applied the HEO concept to the air electrode in solid oxide fuel cell (SOFC) for the first time. They synthesized a series of $La_{1-x}Sr_x(B5)_{3-\delta}$ (for x=0.0-0.5, B=Co, Cr, Fe, Mn, and Ni) and found that the solubility limit of Sr was ≤ 30 mol%. They also found that the synthesized materials exhibited a single-phase rhombohedral ($R\overline{3}c$) structure. The material with x = 0.3 showed maximum conductivity of 16 S/cm at 950°C, which falls within the range considered appropriate for electrode materials and yielded a promising power density value of 550 mW/cm^2 when tested in a button fuel cell setup. The research showed the potential of applying the high-entropy and entropy stabilization concept to SOFC electrodes and suggested that the entropy stabilization concept could resolve the shortcomings of present SOFC electrodes [13]. Further research is required to understand and fully utilize the potential of the high-entropy method for designing SOFC electrodes.

1.2 Perovskite oxide structure (ABO_3) and Goldschmidt tolerance factor "t"

Most of the attractive characteristics of perovskite oxides are due to their crystal structure ABO_3 (Figure 1-1). The crystal structure of the perovskite oxides depends on A-and B-site elements. In perovskite oxide materials, functional characteristics are majorly driven by the Goldschmidt tolerance factor. The unique structure of perovskite oxides ABO_3 has functional characteristics that allow them to be used in various fields, such as a SOFC electrodes [17], a proton-conductors [18], a catalysts [19], dielectric materials [33], and multiferroic materials [21]. The unique crystal structure of perovskite oxides makes them ideal for creating complex and distinctive systems by adding or substituting cations. To predict the structural stability of these new perovskite oxides, the "structural tolerance factor" was introduced by Goldschmidt in 1926, also known as the "Goldschmidt tolerance factor" [22].

$$t = \frac{Ra+Ro}{\sqrt{2}(Rb+Ro)} \tag{2}$$

In equation 2, R_a is the A-site cation radius, R_b is the B-site cation radius, and R_o is the oxygen radius. If $0.9 \leq t \leq 1.0$, a perfect cubic phase is formed; if $t > 1.0$, a hexagonal or tetragonal phase is expected, and if $t < 0.9$, an orthorhombic or rhombohedral phase can be observed [23].
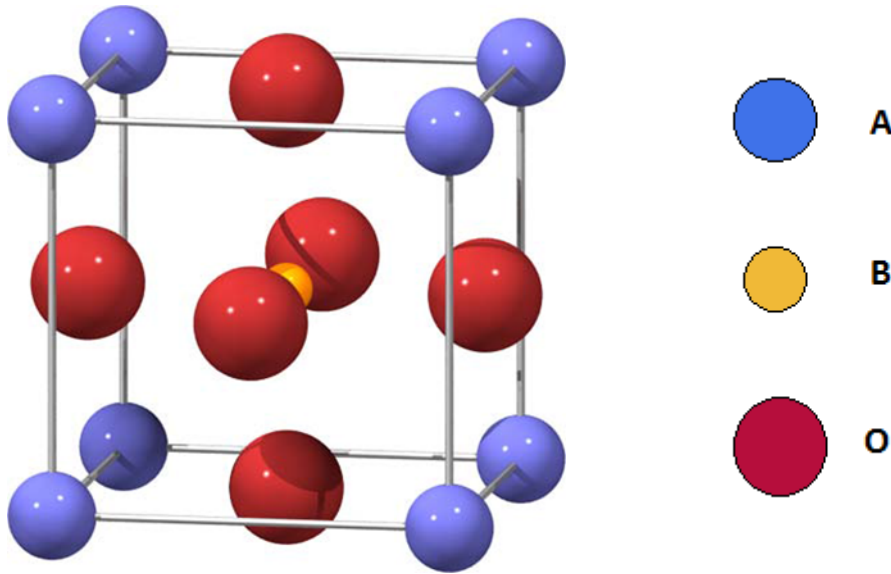
Figure 1-1 ABO_3 perovskite oxide structure

The A-site in ABO_3 is typically occupied by a combination of rare earth and divalent alkaline earth elements, while the B-site has one or more trivalent transition metal elements. The functional properties of perovskite oxides are determined by the B-site transition metal (TM) ions. Substituting a portion of these ions with another TM ion in the same lattice site can influence the functional properties. Additionally, incorporating divalent alkaline earth ions into the A-site can enhance the properties [18, 21–23]. When creating a new perovskite oxide, it's important to consider doping various cations onto both the A- and B-sites [22, 23]. The structural stability of these new materials depends greatly on the Goldschmidt structural factor "t" and the size of the cations occupying the A- and B-sites [28–31]. A couple of recent studies have shown that the addition of multiple cations, or doping, to the B-site of ABO_3 perovskite oxides can be

used to adjust several physical properties at once. This can be very helpful in meeting the complex requirements of practical applications, such as fuel cells [32–35]. SOFC cathode perovskite oxide materials can benefit from the entropy stabilization concept, new materials can be prepared and studied to further improve their functional properties.

1.3 Existing La-based perovskite oxides

Most La-based perovskite materials are utilized as electrodes in SOFCs. Previous research focused on incorporating two B-site transition metals and doping one divalent cation on the A-site with La (S-conf < 1R, low-entropy). It is necessary to fully comprehend the effect of entropy stabilization in perovskite oxides with three or more transition metals on the B-site (medium- and high-entropy) and explore the feasibility of tailoring their performance or functional characteristics based on the application. This section discusses the advantages and limitations of some of the most used La-perovskite oxides with one or two B-site elements.

1.3.1 LaNiO$_3$

Perovskite Nickelate (LaNiO$_{3-\delta}$) exhibits good electrical conductivity of 40 S cm^{-1} at 800°C. It remains stable under reducing conditions below 1000°C but dissociates into La$_2$NiO$_{4+\delta}$ and NiO at 1000°C. This dissociation at temperatures above 1000°C restricts the use of LaNiO$_3$ based perovskite materials. However, the properties of LaNiO$_{3-\delta}$ can be improved by doping other TM in the B-site. For example, LaNi$_{1-x}$Fe$_x$O$_3$ based cathode materials are resistant to chromium disintegration and have shown the same thermal expansion coefficient (TEC) as other fuel cell material [44–46, 47].

1.3.2 LaCoO$_3$

Cobalt-based perovskite materials possess higher ionic and electronic conductivities, reaching 103 S cm^{-1} at 1000°C. However, due to extensive substitution of cobalt, they have high

TEC [40]. Adding Sr to the A-site in $LaCoO_3$ improves the oxygen diffusivity, but doesn't

improve the TEC [48]. A study on the Ca-doped $LaCoO_3$ system found that adding 20 mol% Ca

to the A-site reduced TEC in the 200-400°C range. The same study observed that the 20% Ca

addition resulted in a charge imbalance of Co ions, creating a large number of oxygen vacancies

at temperatures above 800°C and increasing TEC of $La_{0.8}Ca_{0.2}CoO_3$ [49].

1.3.3 $LaFeO_3$

      $LaFeO_3$ is more stable than $LaCoO_3$ due to Fe^{3+} ions stable electronic configuration $(3d^5)$.

The electrical conductivity of $LaFeO_3$ is 0.36 S cm^{-1} at 800°C. The TEC of this perovskite

cathode is close to the TECs of yttria-stabilized zirconia (YSZ) and Gadolinium-doped ceria

(CGO) electrolytes [43–45]. $La_{1-x}Sr_xFeO_3$ cathode showed no degradation over 500 h operations

can be used in low-temperature solid oxide fuel cells (LT-SOFC). However, it reacts with YSZ

electrolyte, leading to the substitution of Zr in the B-site perovskite [46,47]. The

$(La_{1-x}Sr_x)(Co_{1-y}Fe_y)O_{3-\delta}$ system with y=0.8 has several advantages: it has high electrical

conductivity and oxygen surface diffusion, does not react with ceria-based electrolytes, and has

matching TEC with other cell components. It is also highly stable. However, one disadvantage is

that it has lower electrical conductivity when Sr-doping is reduced, and it is not compatible with

the YSZ electrolyte. This results in a higher degradation rate due to Sr-depletion [48–52].

1.3.4 $LaCrO_3$

      $LaCrO_3$ is most widely used cathode material due to its decent electrical conductivity

(0.6-1 S cm^{-1} at 800°C), moderate stability in SOFC working conditions, matching TEC, and

compatibility with other SOFC components [57, 58]. Studies have shown that when temperatures

exceed 800°C in oxidizing conditions, chromium volatilization occurs, resulting in the formation

of CrO_3 and $CrO_2(OH)_2$. This Cr volatilization leads to the development of pores on the cathode surface and degrades the SOFC performance [58, 59].

Research has indicated that doping A-site and B-site perovskite oxides with alkaline earth metals and transition metals has led to more desirable outcomes than traditional perovskite oxides, as seen in studies on $(La, Ca)(Cr, Co)O_3$, and $(La, Sr)(Cr, Mn)O_3$ [49, 57, 60]. A study on the $La_{0.9}Ca_{0.1}Cr_{1-x}M_xO_{3-\delta}$ system, where M = Al, Co, or Mg, revealed that the addition of cobalt to the B-site increased the electrical conductivity (43 S/cm at 1000°C) in comparison to undoped $La_{0.9}Ca_{0.1}CrO_{3-\delta}$ (19.5 S/cm at 1000°C) [57].

1.3.5 LaMnO₃

$LaMnO_3$- and $LaCrO_3$-based cathodes and interconnects without doping on the A-site are sensitive to reducing atmospheres [56]. Cathode materials with acceptor doping on $LaMnO_3$ are usually used due to their stability in oxidizing atmospheres and electrical conductivity at 1000°C. Among them, $(La, Sr)MnO_3$ is the most widely used cathode material due to its stability and compatibility with the YSZ electrolyte as well as other cell materials. However, the disadvantage of Sr-doped $LaMnO_3$ is that it is less stable in reducing conditions and begins to lose oxygen and experience a substantial decrease in conductivity. At 1000°C, strontium-doped $LaMnO_3$ dissociates into La_2O_3, $SrMnO_3$, and MnO, and becomes structurally unstable, potentially causing cell to fail or perform poorly [56].

1.3.6 Three B-site

At the time of this research, there was limited information available regarding the effect of three B-site TM ions doping and La on the A-site. Ozcan and group conducted research on Sr^{+2}-doped $La(CrMnCo)O_3$ (with non-equiatomic ratios of B-site TMs) and found that the electrical conductivity increased with the increase of Co content, forming highly conductive Co

paths. However, the same research also revealed that an increase in Mn reduced the electrical conductivity and increased the activation energy, due to charge carriers being trapped in the Mn site [58]. There is a need for further exploration in the area of multiple TMs ($\geq$3) on the B-site with La on the A-site to understand the unique functional properties of these materials.

1.3.7 Four B-site

In a previous study conducted by Abhigna Kolisetty on low-entropy La(Ni,Fe,Co,Cr)O_3 systems, five samples were produced: La(Cr$_{0.7}$Co$_{0.1}$Fe$_{0.1}$Ni$_{0.1}$)O_3, La(Co$_{0.7}$Cr$_{0.1}$Fe$_{0.1}$Ni$_{0.1}$)O_3, La(Ni$_{0.7}$Cr$_{0.1}$Fe$_{0.1}$Co$_{0.1}$)O_3, La(Fe$_{0.7}$Ni$_{0.1}$Cr$_{0.1}$Co$_{0.1}$)O_3, as well as La(Cr$_{0.25}$Co$_{0.25}$Fe$_{0.25}$Ni$_{0.25}$)O_3. The samples with low Cr content showed good electrical conductivity (15-55 S/cm at 800°C) and sintering properties. However, the sample with high Cr content could not be sintered because of chromium volatilization [59].

A study on a calcium-doped (0-30 mol%) medium-entropy perovskite oxide of La(Cr$_{0.25}$Co$_{0.25}$Fe$_{0.25}$Ni$_{0.25}$)O_3 showed that calcium addition reduced sintering temperatures, and produces fully dense pellets. This, in turn, improved electrical conductivity from 21 S/cm for La(Cr$_{0.25}$Co$_{0.25}$Fe$_{0.25}$Ni$_{0.25}$)O_3 to 50 S/cm for La0.7Ca0.3(Cr$_{0.25}$Co$_{0.25}$Fe$_{0.25}$Ni$_{0.25}$)O_3 and reduced activation energies [60].

The current cathode materials used in SOFCs have many benefits, along with some limitations. To address these limitations, new materials are needed that have high electronic conductivity, excellent stability at high temperatures, desirable thermal expansion characteristics, and can be easily manufactured by sintering in a way that is compatible with other cell components. This can be achieved by modifying the existing alkaline earth and transition metal-based cathodes. By studying these new materials, the goal is to enhance electrical conductivity,

lower the required sintering temperature, and improve stability through adjusting the doping properties.

Previous work on the parent members of $LaCrO_3$, $LaCoO_3$, $LaMnO_3$, $LaFeO_3$, and $LaNiO_3$ mainly focused on adding one or two elements to either the A-site or B-site. However, past research showed that doping three or four elements onto the B-site improves electrical conductivity and sintering properties [58–60]. Additionally, adding calcium to the A-site was found to enhance electrical conductivity in the intermediate temperature zone (500-750°C) [45,60].

1.4 Materials processing

There are several methods used for synthesizing perovskite oxides, including solid-state, drip pyrolysis, sol-gel, citrate gel, and several other methods such as polymerizable precursor method (PPM), glycerin nitrate, freeze-drying, and spray drying EDTA [20, 65–73]. Out of all these methods, PPM, EDTA, and glycerin nitrate are the most commonly used. In this study, PPM was used to synthesize the materials, as it has been found to be suitable for producing homogeneous nano-sized particles in the previous research [63, 64]. It is important to note that the synthesis method, doping elements at the A- and B-sites, calcination temperatures, and sintering conditions all play a significant role in determining the characteristics and functional properties of perovskite oxides [71–74].

This new study explores the effects of doping the B-site with three (S-conf = 1.01R, medium-entropy perovskite oxide, MEPO) and five transitional metal ions (S-conf = 1.61R, high-entropy perovskite oxide, HEPO) in equal atomic ratios and the A-site with La and Ca. We synthesized different compositions using the PPM method, and will examine their properties, including phase purity, crystal structure, grain structure of sintered pellets, sintered densities, and

electrical conductivity. The is to understand how different combinations of three and five transitional metals on the B-site and Ca doping on the A-site affect these properties. It is believed that these synthesized materials will have unique functional properties compared to their parent members.

CHAPTER 2

EXPERIMENTAL METHODOLOGY

2.1 Synthesizing process

Various MEPO and HEPO compositions presented in this dissertation were prepared using the PPM [70]. Synthesis procedures varied depending on the perovskite oxide system's composition. This section gives a general process for the powder synthesis; any additional information on the synthesis procedure will be provided in the relevant chapters.

2.2 Apparatus

Equipment used to synthesize powders were a 600 mL beaker, a one-liter beaker, a metal spatula, a weight balance, a glass rod for stirring, a magnetic stirrer, and a tray for weighing the materials. The starting materials were lanthanum carbonate, chromium nitrate, calcium carbonate, iron nitrate, nickel nitrate, cobalt nitrate, manganese carbonate, citric acid, and ethylene glycol.

2.3 Mixing of materials

The synthesis process starts with the careful batch calculation of all the starting materials according to the stoichiometric proportions. After the initial batch calculations, starting materials were added to a 600 mL beaker with varying amounts of citric acid and ethylene glycol, depending on the perovskite oxide system. After adding these chemicals to the beaker, the mixture was stirred with a glass rod at room temperature. Later the whole setup was placed on a hot plate and heated at 60°C for 4-6 hours, and a magnetic stirrer was added to the mixture to mix the materials.

The hot plate temperature was increased to 95°C and maintained for another 4-6 hours. As excess amount of water evaporated during the heating process, a polymer-like resin was

formed through an accelerated polyesterification reaction. Once the resin-like substance was formed, the hot plate temperature was increased to 350-400°C to complete the polyesterification process. At 350°C, white grayish fumes appeared. The hot plate was turned off after the fumes stopped, and the setup was cooled to room temperature.

2.4 Calcination

After cooling, the material from the previous step was taken into a ceramic crucible for calcination and heated in a box furnace between 900-950°C for 8-9 hours. The calcination process evaporates excess water, unreacted materials, volatile substances, sulfur, nitrites, carbonate, and carbon dioxide [75]. At the time of calcination, partial or complete oxidization occurs.

2.5 Ball milling

Calcined powders were added to a plastic vial with 1 or 2 methacrylate balls for ball milling. The whole setup was placed in a miller and milled for 20 minutes. Methacrylate balls agitated the material throughout the mixing process. Ball milled powders were subjected to x-ray diffraction to check the phase purity of the materials.

2.6 Pellet preparation

After determining the phase purity of the synthesized materials using X-ray diffraction, all single-phase materials were pressed into pellets. The powder materials were taken in a plastic vial with a PVA binder and methacrylate balls and were milled for 20 to 30 minutes. The powders were pelletized into circular discs (diameter 13mm), called green pellets, with a pressure of 14 mPa. The green pellets' densities (green densities) were calculated using their dimensions and mass.

2.7 Sintering

Green pellets from the previous step were sintered at 1200, 1300, and 1400°C for 2 hours in atmospheric air. During the sintering process, material microstructures develop through various sintering processes, and this densifies and strengthens the pellets. After sintering, the pellets were cooled to room temperature to determine their sintered densities. Sintered densities were determined using the Archimedes immersion principle, as shown in equation 3.

$$\text{Sintered density} = \left(\frac{ma}{ma - ml}\right) \text{x density of liquid} \qquad (3)$$

Where m_a and m_l are the masses of the pellets in air and liquid, respectively. The density of the liquid is 1 for distilled water.

2.8 Polishing

The sintered materials were polished until mirror finishing was achieved. For the pellets polishing, suspension liquid, polishing medium (45, 12, 9, 6, 3, and 1 micron), and fiber. Later polished pellets were thermally etched at 100°C below their sintering temperature for one hour. This opened the pores and grains on the surface and made it easier to observe the grain structure, boundaries, and pores under a scanning electron microscope.

CHAPTER 3

CHARACTERIZATION TECHNIQUES

3.1 X-ray diffraction (XRD) and crystal structure analyzation

Various techniques were used to characterize the synthesized materials. The general

description of the methods used for characterization is mentioned in this chapter. XRD was first

used to study the crystal structure of calcined and ball-milled final powders. A Rigaku D/Max-B

diffractometer, with Cu Kα radiation, was used to study the structure of the materials at room

temperature. XRD patterns were recorded for a 2θ range of 20-80° using a stepwise scan method

(scan rate of 0.02°/sec).

The obtained crystal structure of the powder material was analyzed by the search-match

function in the Jade 11 program, which searches and matches the pattern to the materials

available in the ICDD (International Center for diffraction data) database. Data from the XRD

was later used to calculate the unit cell parameters such as lattice constants, unit cell volume,

crystallite size, pseudo lattice constant and full width half maxima (FWHM). The position,

height, and width of the peaks in the XRD spectrum can be used to study and determine many

attributes of the materials' crystal structure.

3.2 Crystallite size measurement

The crystallite sizes of the synthesized materials were calculated from their respective

XRD graphs by using the Scherrer equation [76].

$$\tau = \frac{K\lambda}{\beta \cos \theta} \tag{4}$$

Here τ is the crystallite size in nanometers; K is the shape factor constant, which is 0.94 for

orthorhombic structure; β is the value for full width at half maximum in radians; λ is the

wavelength of Kα radiation of Cu target x-ray tube, which is 1.540598 Å, and θ is the Braggs

diffraction angle in degrees.

3.3 Scanning electron microscope (SEM) & energy dispersive spectroscopy (EDS or EDXS)

Microstructural studies of thermally etched pellets were carried out using an FEI Quanta FEG 450 SEM. SEM images of the samples at various magnification levels were taken to analyze the grain size, boundaries, and pores. To study the interfacial reactions and surface chemistry of the etched pellets, OXFORD Instruments INCA Energy 200 X-Ray Detector was used.

3.4 Measurement of electrical conductivity (EC)

Sintered pellets of perovskite oxides fired at 1400°C were cut into rectangular bars (3x3x10mm) and then coated with platinum ink for electronic conductivity studies. The four-probe method (shown in Figure 3-1) was utilized to study the electronic conductivity of the rectangular bars using an A.C. resistance Bridge (Liner Research Inc. LR-700, San Diego, CA) in atmospheric air at temperatures of 300-1000°C. First, the pellet was heated to 1000°C and left at this temperature for 12 hours to stabilize the resistance of the pellet. At every 100°C decrement in temperature, the pellet was held until a constant resistance reading was obtained. This allows to collect an accurate resistance reading of the pellets. Electrical conductivity values were calculated using the below equations.

$$\text{Electrical resistivity, } \rho = \frac{RA}{L} \tag{5}$$

$$\text{Electrical conductivity, } \sigma = \frac{1}{\rho} \tag{6}$$

In this formula, R is resistance, A is the area of cross-section of the pellet, and L is the length of the pellet.
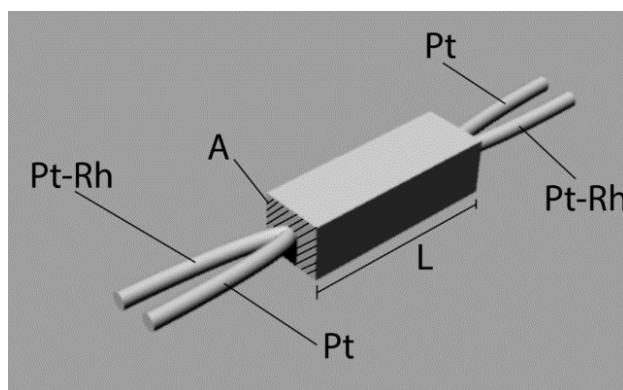
Figure 3-1 Electrical conductivity measurement of a pellet

Table 3-1 Various compositions of MEPOs and HEPOs synthesized and characterized in the present study

Name	Compositions	Perovskite type	S-conf
System 1	$La_{1-x}Ca_x(Cr_{1/3}Fe_{1/3}Ni_{1/3})O_3$	MEPO	1.01R
System 2	$La_{1-x}Ca_x(Cr_{1/3}Mn_{1/3}Co_{1/3})O_3$	MEPO	1.01R
System 3	$La_{1-x}Ca_x(Cr_{1/3}Mn_{1/3}Ni_{1/3})O_3$	MEPO	1.01R
System 4	$La_{1-x}Ca_x(Cr_{1/3}Mn_{1/3}Fe_{1/3})O_3$	MEPO	1.01R
System 5	$La_{1-x}Ca_x(Cr_{1/3}Fe_{1/3}Co_{1/3})O_3$	MEPO	1.01R
System 6	$La_{1-x}Ca_x(Cr_{1/3}Ni_{1/3}Co_{1/3})O_3$	MEPO	1.01R
System 7	$La_{1-x}Ca_x(Fe_{1/3}Mn_{1/3}Ni_{1/3})O_3$	MEPO	1.01R
System 8	$La_{1-x}Ca_x(Co_{1/3}Fe_{1/3}Mn_{1/3})O_3$	MEPO	1.01R
System 9	$La_{1-x}Ca_x(Fe_{1/3}Ni_{1/3}Co_{1/3})O_3$	MEPO	1.01R
System 10	$La_{1-x}Ca_x(Cr_{0.2}Co_{0.2}Fe_{0.2}Mn_{0.2}Ni_{0.2})O_3$	HEPO	1.61R

Table 3-1 shows the various compositions of MEPOs and HEPOs synthesized using PPM and studied in the present research along with their S-conf values.

CHAPTER 4

GOLDSCHMIDT STRUCTURAL TOLERANCE FACTOR

A modified Goldsmith structural tolerance factor (GSTF), t, was used to check the

structure of the perovskite oxides in the present study [22]. The standard GSTF equation (shown

in equation 2), couldn't be used for the complex perovskite oxide systems of the present study, so

a modified equation previously described by Trofimenko [77,78] was used instead. The GSTF

was calculated using the ionic radii of cations and anions (see Table *4-1*) proposed by Shannon

[79]. Equations 7 and 8 show the modified tolerance factors for complex perovskites like MEPO

and HEPO, respectively.

$$t = [(1-x) * R_{La}^{3+} + (x) * R_{Ca}^{2+} + R_O^{2-}] / \sqrt{2} * [1/3 (R_1^{3+} + R_2^{3+} + ^{3+}) + R_O^{2-}] \qquad (7)$$

$$t = [(1-x) * R_{La}^{3+} + (x) * R_{Ca}^{2+} + R_O^{2-}] / \sqrt{2} * [1/5 (R_1^{3+} + R_2^{3+} + R_3^{3+} + R_4^{3+} + R_5^{3+}) + R_O^{2-}] (8)$$

where R_{La}, R_{Ca}, R_1, R_2, , R_3, R_4, R_5 and R_O^{2-} are the ionic radius of lanthanum, calcium, B-site

transitional metal cations, and oxygen anion, respectively, and x is the calcium mole fraction.

Table 4-2 shows that the modified GSTF failed to predict the formation of actual

perovskite structures. Instead, the XRD results showed the formation of orthorhombic and

rhombohedral systems, whereas the modified GSTF predicted only cubic perovskite structure for

all perovskite oxide systems.

The addition of smaller ionic radius of Ca^{+2} (1.34Å) with the larger ionic radius size of

La^{+3} (1.36Å) slightly changed the, t, value, but it remained close to 1, indicating a stable

perovskite structure for MEPO and HEPO. Past research has shown that when t=1, the bond

angle of B-O-B (transitional-oxygen-transitional) equals 180° and such perovskite material has

good electronic conductivity [32]. The close proximity of the present MEPO and HEPO, t values

to 1 suggests that they are expected to have good electronic conduction [32]. Interestingly, the

MEPO systems 4 and 7 with GSTF < 0.97 showed the least electrical conductivity values (< 10S/cm) compared to the other oxide systems with GSTF > 0.97. More information on the electrical conductivity of these oxide systems will be discussed in subsequent chapters.

Table 4-1 Ionic radius for the cations and anions

Cation	Ionic radii (Å)
La^{+3}	1.36
Ca^{+2}	1.34
Cr^{+3}	0.615
Co^{+3}	0.545 (High spin)
Fe^{+3}	0.645 (High spin)
Ni^{+3}	0.56 (Low spin)
Mn^{+3}	0.645 (High spin)
O^{-2}	1.4

Table 4-2 Goldschmidt structural tolerance factor (GSTF, t)

MEPO systems	Ca 0 mol%	Ca 10 mol%	Ca 20 mol%	Ca 30 mol%	Predicted perovskite oxide structure	Observed perovskite oxide structure from XRD
1	0.9725	0.9718	0.9711	0.9704	Cubic	Orthorhombic
2	0.9749	0.9742	0.9735	0.9728	Cubic	Orthorhombic
3	0.9725	0.9718	0.9711	0.9704	Cubic	Orthorhombic
4	0.9590	0.9583	0.9576	0.9569	Cubic	Orthorhombic
5	0.9749	0.9742	0.9735	0.9728	Cubic	Orthorhombic
6	0.9889	0.9882	0.9875	0.9868	Cubic	Rhombohedral and Orthorhombic
7	0.9677	0.9670	0.9687	0.9680	Cubic	Orthorhombic
8	0.9701	0.9694	0.9687	0.9680	Cubic	Orthorhombic
9	0.9840	0.9832	0.9825	0.9818	Cubic	Rhombohedral and Orthorhombic
10	0.9748	0.9741	0.9734	0.9727	Cubic	Orthorhombic

CHAPTER 5

PRELIMINARY STUDIES ON THE SYNTHESIS AND CHARACTERIZATION OF CALCIUM-

DOPED $La(Cr_{1/3}Fe_{1/3}Ni_{1/3})O_3$ MEPO SYSTEM

5.1 Introduction

This chapter presents the synthesis and study of the first MEPO system,

$La_{1-x}Ca_x(Cr_{1/3}Fe_{1/3}Ni_{1/3})O_3$ (system 1) prepared using modified PPM. Phase purity,

microstructures and functional properties were analyzed and characterized through XRD, SEM,

and electrical conductivity measurement. Results show the possibility of synthesizing single-

phase powders by optimizing the calcination temperature. The XRD data validated the solubility

of Ca in the material to be ≤ 30 mol%, beyond which the increase in Ca content resulted in the

formation of secondary phases of CaO and NiO. The materials were found to adopt an

orthorhombic perovskite structure with space group Pbnm for $0.0 \leq x \leq 0.3$. The EDXS data

confirmed a uniform distribution of A and B site elements in all compositions, with a gradual

reduction in the unit cell volume observed upon substitution of calcium for lanthanum. SEM

images revealed the transition from open-porous grains to a closed-porous grain structure and

improved sinterability upon the addition of calcium. Addition of calcium also improved the

electrical conductivity and lowered the activation energy. This initial study provided a

foundation for understanding the synthesis process, and subsequent materials were adjusted

accordingly.

5.2 XRD results

The first sample of system 1 (sample 1.1), was initially calcined at 850°C; the XRD

spectrum showed the presence of unreacted secondary phases, as seen in Figure 5-1. Later, the

calcination temperature of sample 1.1 was increased to 950°C, which prevented the formation of

secondary phases. This suggests that the optimal calcination temperature for sample 1.1 was around 950°C. According to XRD results, materials calcined at 850 and 950°C have the same perovskite structure as $LaFeO_3$ (Pbnm, space group: 62), but the sample calcined at 850°C also shows the presence of La_2O_3 (hexagonal) and FeO (cubic) phases. Figure 5-1b shows that with the increase in calcination temperature to 950°C, the secondary phases disappear. The presence of La_2O_3 and FeO in Figure 5-1a indicates an incomplete reaction at 850°C, which is consistent with the results from Figure 5-1b that show a reduction in secondary phases when calcined at 950°C. The remaining samples 1.2-1.5 containing Ca 10-40 mol% were calcined at 950°C for 9 hours.

In Figure 5-2, all peaks of samples 1.2-1.4 are indexed with respect to the orthorhombic perovskite structure of $LaFeO_3$, which belongs to the Pbnm space group. XRD patterns of samples 1.3 and 1.4 reveal the presence of minor secondary peak of FeO (cubic). The resurfacing of the secondary peak can be attributed to the increase of Ca doping levels.

The major peak of sample 1.3 shows asymmetric shape, which can be due to the crystal lattice distortion in the powder sample. Another notable mention is the shifting of the major peak from its initial 2θ position for the samples 1.2 and 1.3 and returning to its initial position for sample 1.4 (see Figure 5-3). The shifting of the major peak is expected in this type of perovskite oxide solution due to the change in lattice parameters of the unit cells caused by the introduction of the slightly smaller Ca^{+2} ion in the La^{+3} site [79].
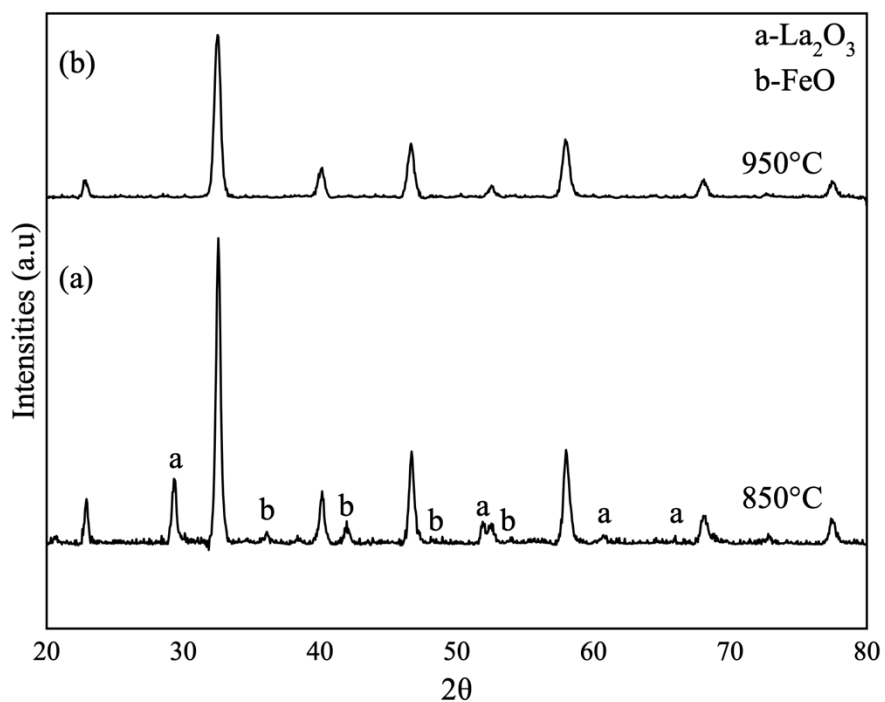
Figure 5-1 XRD graphs of sample 1.1 calcined at 850 and 950°C for 9 hours
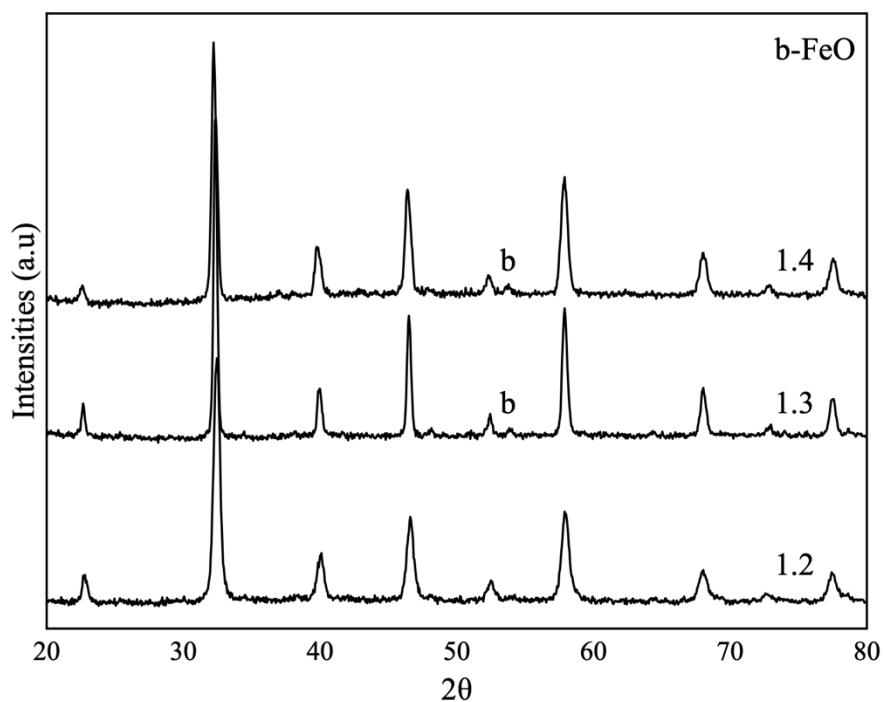
Figure 5-2 XRD graphs of samples 1.2-1.4 (Ca 10-30 mol%) calcined at 950°C for 9 hours
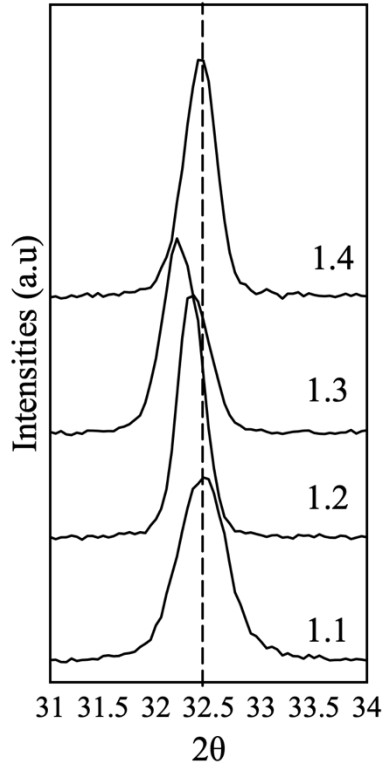
Figure 5-3 Magnified view of the highest peak between 31-34° 2θ values of system 1 samples

The XRD pattern of sample 1.5, which contains 40 mol% Ca on the A-site, calcinated at 950, 1050, and 1150°C, are shown in Figure 5-4. The initial calcination at 950°C for 9 hours resulted in secondary phases of CaO and NiO, indicating an incomplete reaction. When the powder was later calcinated at 1050°C for 9 hours and 1150°C for 12 hours, the secondary phases did not dissolve completely. This questions the solubility of 40 mol% Ca in $La(Cr_{1/3}Fe_{1/3}Ni_{1/3})O_3$ crystal structure.

As a result, it is believed that the solubility of Ca substitution in $La(Cr_{1/3}Fe_{1/3}Ni_{1/3})O_3$ perovskite solid solution should be less than 40 mol%. The presence of single-phase solid solutions was only achieved when Ca substitution was ≤ 30 mol%. Therefore, the samples with 40 mol% Ca were not studied further because they produced secondary phases. In this study, all synthesized and characterized perovskite systems were doped with Ca in the range of 10-30 mol% on the A-site, due to solubility limitations of Ca with La.

24
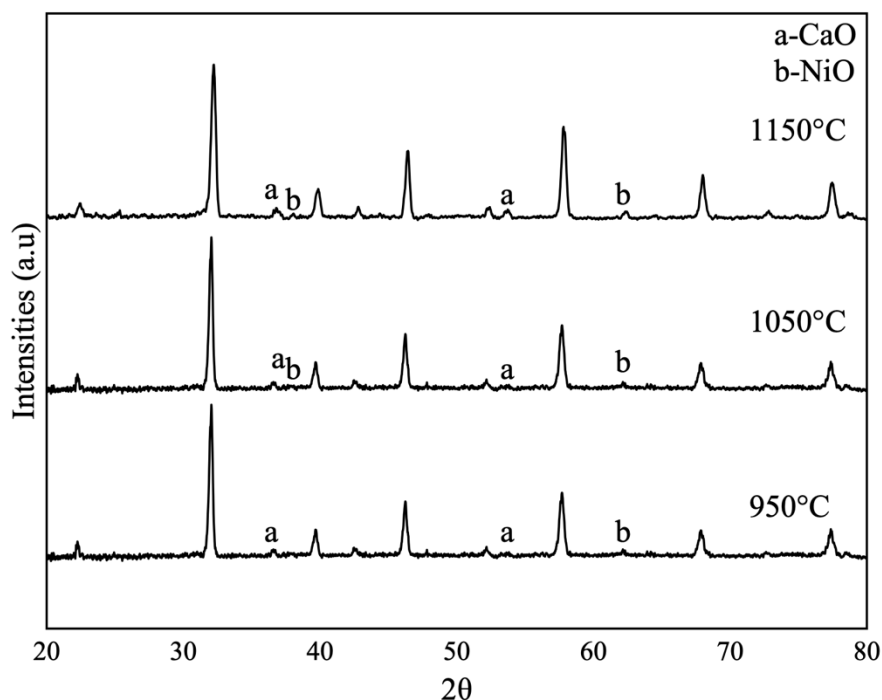
Figure 5-4 XRD graphs of sample 1.5 (Ca 40 mol%) calcined at 950°C (9 hours), 1050°C (9 hours) and 1150°C (12 hours)

5.2.1 Lattice Parameters

The peak positions of (002), (112), (202), (004), (141), (024), (025), and (116) were used to calculate the lattice parameters and unit cell volume, as shown in Table 5-1. The lattice constants decreased as the Ca content increased. The unit cell volume and parameters shrunk linearly, with the c-axis shrinking by about 0.5% and the b-axis shrinking by 1% for the sample with 30 mol% Ca substitution (sample 1.4). The overall volume shrinkage from 0 to 30 mol% Ca substitution was around 4%, which was the sum of the shrinkage in all three axes. The reduction in unit cell volume of the perovskite solid solution was slightly higher than the difference in cation size (La =1.36 Å and Ca =1.34 Å), suggesting that charge-compensating oxygen vacancies influence the reduction. This linear reduction in the cell volume of the perovskite oxide system is consistent with previous reports on A-site doped materials [87].

25

Table 5-1 System 1 lattice parameters, unit cell volume, crystallite size, and pseudo cubic lattice constant

Compositions	Space group	a (Å)	b (Å)	c (Å)	Unit cell volume (Å³)	Crystallite size (nm)	Pseudo cubic lattice a_0 (Å)
1.1	Pbnm	5.52	5.69	7.81	245.073	26.3	3.94226
1.2	Pbnm	5.51	5.66	7.79	243.004	25.14	3.93113
1.3	Pbnm	5.5	5.66	7.79	242.007	24.04	3.92575
1.4	Pbnm	5.49	5.63	7.77	240.244	23.03	3.91619

5.2.2 Crystallite size and pseudo cubic lattice parameter

The XRD patterns of each perovskite material shown in Figure 5-1 and Figure 5-2 were used to calculate crystallite size using Scherrer law; the values are given in Table 5-1. The crystallite sizes reduced as the level of Ca doping in the La-site increased. Table 5-1 also provides the pseudo cubic lattice parameter (a_0) for each perovskite material, which was obtained using the equation 9.

$$a_0 = \left(\frac{v}{z}\right)^{\frac{1}{3}} \tag{9}$$

In the formula, "v" is the unit cell volume and "z" represents how much larger the orthorhombic unit cell is compared to the pseudo cubic unit cell.

Table 5-1 shows a clear correlation between the Ca doping levels and the calculated structural parameters, like pseudo cubic lattice parameters, and crystallite size. All parameters reduced as the Ca content increased from 10-30 mol% with La. This reduction, which was caused by the smaller Ca replacing larger La, indicates the dependence of the cell parameters on the Ca content.

5.3 SEM studies

Figure 5-5 shows SEM micrographs of pellets sintered in air at temperatures of 1200-1400°C for two hours. Table 5-2 summarizes the sintered densities calculated using the Archimedes immersion technique. The sample without calcium (sample 1.1) was difficult to sinter from 1200-1400°C, and reached a low sintered density of only ~75% due to the lack of calcium. With calcium doping (samples 1.2-1.4), the sintered densities increased to 88%-92%. Interestingly, sintered densities of calcium-doped pellets increased with the concentration of calcium.

SEM images of sample 1.1 reveal non-homogeneous grains with open pores, whereas the calcium-doped samples have a relatively homogenous microstructure with fewer open pores. The low relative density and less-sintered microstructure of the calcium-free sample can be attributed to the absence of liquid phase.

As seen in Table 5-2, relative densities of the 10, 20, and 30 mol% Ca-doped pellets attained their maximum value after sintering at an initial temperature of 1200°C. Further increase in sintering temperature had little impact on the sintered density. It is well known from previous research that the addition of calcium improves the sintering characteristics by reducing the sintering temperature and improving the relative density [81–83].

Table 5-2 Relative sintered densities (%) of system 1 pellets sintered at 1200, 1300, and 1400°C for 2 hours

MEPO Samples	1200°C	1300°C	1400°C
1.1	70	71	75
1.2	88	86	88
1.3	90	90	91
1.4	92	91	92

The average grain sizes of the pellets, calculated through the line intercept method, are shown in

Table 5-3. At all sintering temperatures, the calcium-doped pellets had larger grain sizes compared to the calcium-free pellets. The average grain size of the calcium-doped samples decreased as the calcium doping levels increased. SEM images of the calcium-doped pellets showed well-defined and curved grain boundaries as shown in Figure 5-5, indicating that the pellets were sintered in a liquid phase.

Table 5-3 Average grain size (μm) of system 1 pellets sintered at 1200, 1300, and 1400°C for 2 hours

MEPO Samples	1200°C	1300°C	1400°C
1.1	1.12	0.27	1.31
1.2	1.42	1.45	1.76
1.3	1.56	1.54	1.68
1.4	1.27	1.44	1.51
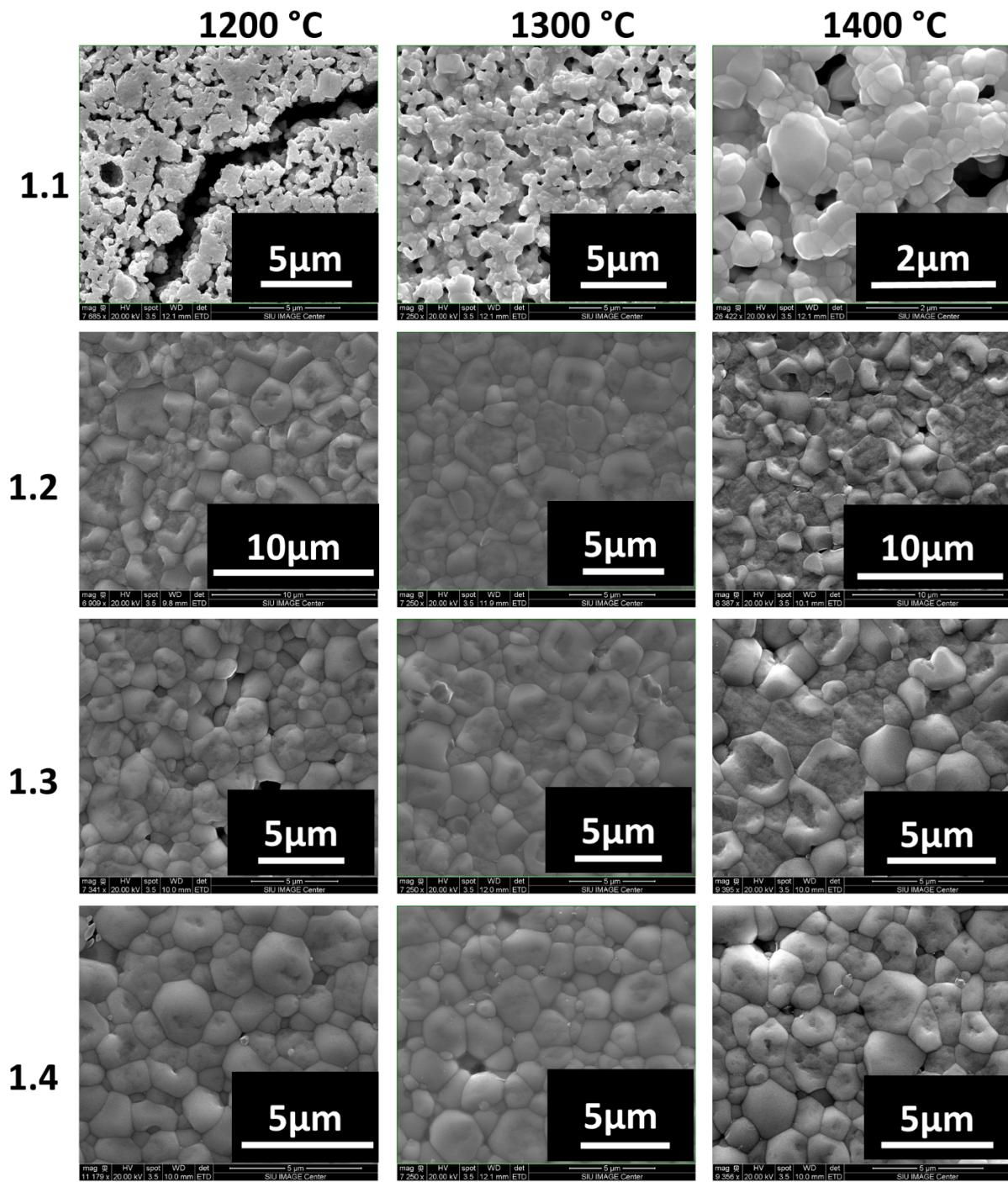
Figure 5-5 SEM images of system 1 pellets sintered at 1200, 1300, and 1400°C for 2 hours

Previous experiments have proven that calcium doping enhances sintering through the creation of a transient liquid phase in $LaCrO_3$ materials due to a temperature-sensitive calcium oxychromate $(Ca_m(CrO_4)_n)$ phase [81–83]. The low-melting calcium oxychromate is believed to promote the sintering of calcium-doped $La(Cr_{1/3}Fe_{1/3}Ni_{1/3})O_3$ by a transient liquid phase sintering. The calcium oxychromate phase melts incongruently and increases mass transport by reacting with $La_{1-x}Ca_x(Cr_{1/3}Fe_{1/3}Ni_{1/3})O_3$ and, thereby, rapidly densifies the samples [81]. With increased calcium doping, a secondary liquid phase may form during the sintering process. As the concentration of the liquid phase increases, the diffusion distance also increases, leading to a decrease in grain size [84]. The grain size of the calcium-doped samples increases with sintering temperature, as previously described in the literature [53, 89–91].

5.4 EDXS maps

The elemental analysis of system 1 samples sintered in air at 1400°C for 2 hours is shown in Figure 5-6 and Table 5-4. The analysis was done using EDXS and aimed to evaluate the uniform distribution of A and B site elements in system 1. The results from EDXS confirmed the presence of La, Cr, Fe, and Ni in sample 1.1 and La, Ca, Cr, Fe, and Ni in the samples 1.2-1.4. The EDXS maps show the homogeneity of sample 1.1 and the localization of Ca in the Ca-doped samples 1.2-1.4.

Table 5-4 Results of EDXS elemental analysis of system 1 MEPO sintered at 1400°C

MEPO system	La (wt%)	Ca (wt%)	Cr (wt%)	Fe (wt%)	Ni (wt%)
1.1	54.33	-	14.26	16.56	14.86
1.2	34.18	23.97	13.48	15.19	13.19
1.3	41.29	11.83	15.06	16.38	15.43
1.4	39.28	24.29	12.16	12.44	11.84
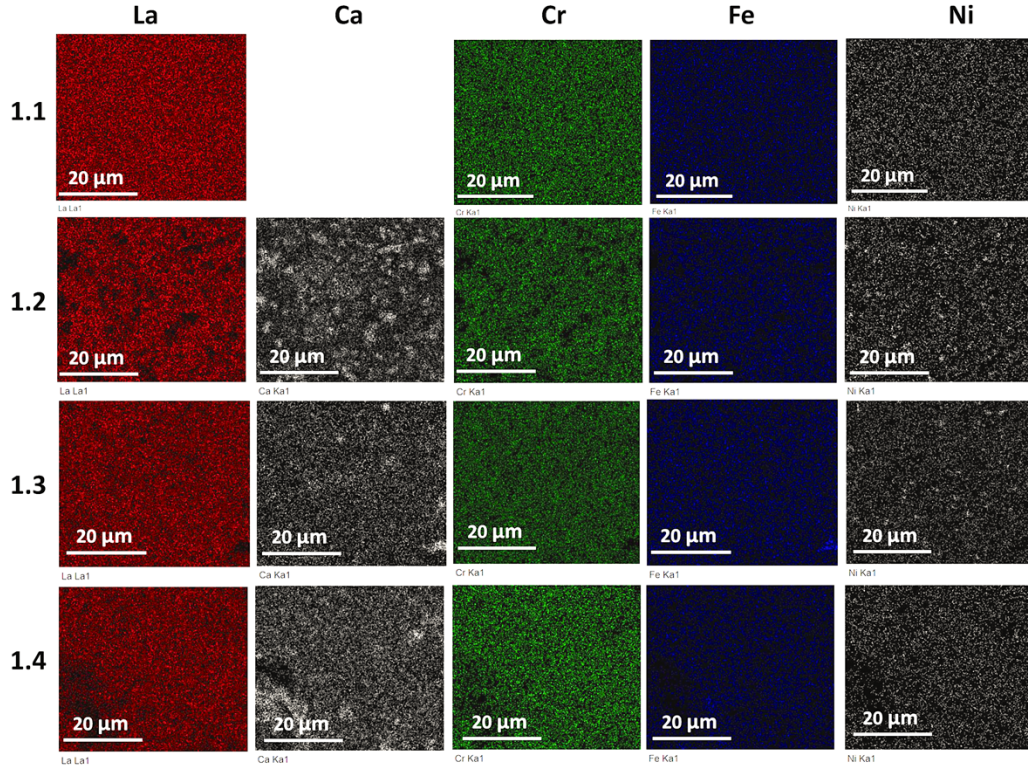
Figure 5-6 EDS elemental maps of system 1 MEPO compositions

5.5 Temperature dependence electrical conductivity

Measurements for electrical conductivity in perovskite oxide system 1 were carried out in atmospheric air at temperatures ranging from 300°C to 900°C. All four samples of system 1 showed thermal-activated electronic conduction, meaning that their electronic conductivity increased as temperature increased, as shown in Figure 5-7. The conductivity graph was linear, indicating that the conductivity of the system was due to the hopping of small p-type polarons in the BO_6 tetragonal network [32]. The electrical conductivity through a small polaron hopping mechanism is represented by the equation 10:

$$\sigma = \frac{C}{T} exp\left(-\frac{E_a}{kT}\right) \qquad (10)$$

where, C represents the available site occupied by charge carriers, T is the absolute temperature, E_a is the activation energy, σ the electrical conductivity, and k is the Boltzmann constant.
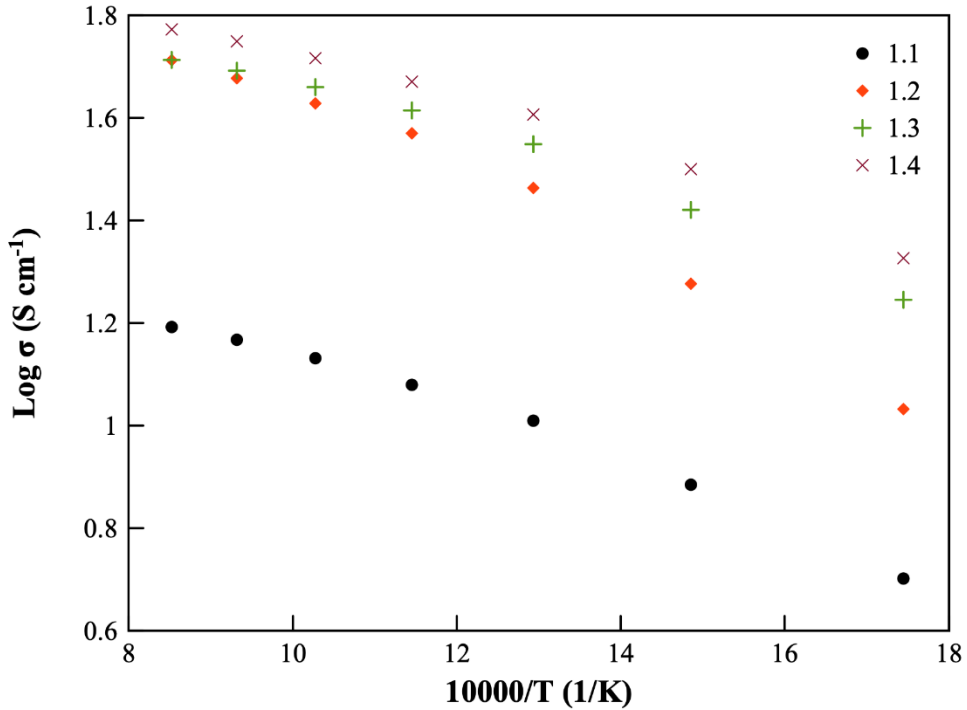
Figure 5-7 Log(σ) vs. 10000/T of system 1 in atmospheric air

The electrical conductivity and activation energy values at 800°C are presented in Table 5-5. The electronic conductivity of the calcium-free sample was 15 S/cm at 800°C. The conductivities of sample 1.2 (Ca 10 mol%) and 1.3 (Ca 20 mol%) were three times the calcium-free sample. The conductivity of sample 1.4 (highest calcium-doped sample), was almost four times that of a calcium-free sample. The significant improvement in conductivity can be related to the divalent calcium (Ca^{+2}) doping in the A-site with trivalent lanthanum (La^{+3}). The addition of divalent calcium to the A-site in perovskite oxides, such as system 1, which creates a charge imbalance that can be compensated by either oxidizing the B-site transition metal ions from +3 to +4 or increasing oxygen vacancies. In general, electrical conductivity in ABO_3 materials is improved if the charge imbalance creates +4 valence states of B-site elements and improves further when the ratio of B^{+3}/B^{+4} couples (B-site couples) is 1:1 [32]. These B-site couples act as

32

small polaron hopping sites and enhance electronic conduction by facilitating the mobility of charge-carrying polarons [32].
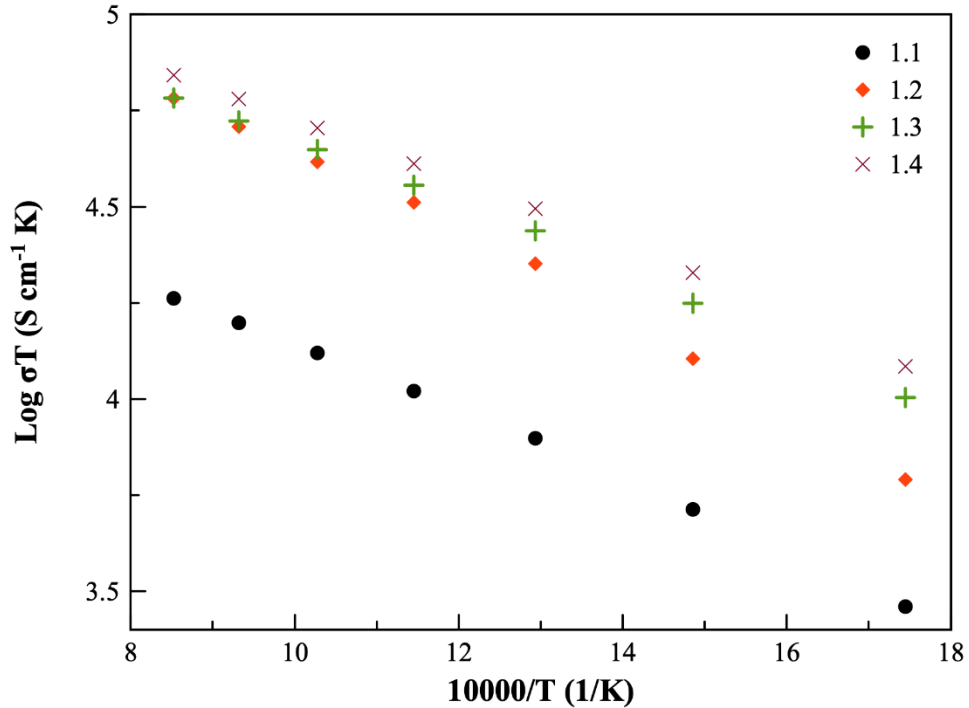
Figure 5-8 Arrhenius plots of system 1

The electrical conductivity data of system 1 indicates that an increase in divalent cations in the A-site leads to an increase in small polaron hopping sites and, therefore, in electrical conductivity. The activation energies were calculated from the slopes of the linear plots in Figure 5-8. The data indicate that the addition of calcium affected the activation energies of the samples. The highest activation energy of 0.96 eV at 800°C was observed for the sample 1.2 and can be attributed to the strong localization of small polarons. Such behavior has been observed previously [47, 88–90]. The addition of further calcium in samples 1.3 (20 mol% Ca) and 1.4 (30 mol% Ca) reduced the activation energy (results are shown in Table 5-5). The reduction in activation energy in these samples suggests that the Fermi levels moved closer to the valence band as a result of incremental calcium doping [88–90].

Table 5-5 Activation energy and electrical conductivity values system 1 at 800°C

Samples	Activation Energy (eV)	Electrical conductivity at 800°C (S/cm)
1.1	0.77	15
1.2	0.96	48
1.3	0.75	50
1.4	0.73	57

5.6 Conclusions

The present chapter provides the initial information regarding synthesis, characterization, and functional properties of system 1. The XRD results show the possibility of preparing single-phase powders using PPM, while change in calcination temperature aids in the reduction of unreacted phases. The XRD data also validated the solubility of Ca is ≤ 30 mol% as increase in Ca above 30 mol% produced secondary phases of CaO and NiO. The $La_{1-x}Ca_x(Cr_{1/3}Fe_{1/3}Ni_{1/3})O_3$ materials adopt an orthorhombic perovskite structure with space group Pbnm for $0.0 \leq x \leq 0.3$. The EDS data confirms a uniform random distribution of A and B site elements in all compositions. A gradual substitution of lanthanum with calcium reduces the volume of unit cells. SEM images of the calcium-free sample (sample 1.1) display the transitioning from open porous grains to a closed porous grain structure. SEM images also confirmed that the incremental addition of calcium reduced the porosity and improved sinterability via liquid phase sintering. Calcium doping also improved the electrical conductivity while lowering the activation energy. The highest electrical conductivity of 57 S/cm with activation energy of 0.73 eV, occurred for the sample with maximum calcium doping.

The synthesis of system 1 provided much needed information with respect to the duration of mixing, temperatures for each step of synthesis, amount of citric acid and ethylene glycol

necessary, and the overall purity of the powders. Systems 2-10 utilized the modified synthesis of

system 1; their results will be discussed in the following chapters.

CHAPTER 6

SYNTHESIS, CHARACTERIZATION, AND ELECTRICAL CONDUCTIVITY STUDIES OF

$La_{1-x}Ca_x(Cr_{1/3}Mn_{1/3}M_{1/3})O_3$ MEPO SYSTEM (x = 0-30 mol% and M = Co, Ni and Fe)

6.1 Introduction

Based on the synthesis process of system 1, the MEPO powders of

$La_{1-x}Ca_x(Cr_{1/3}Mn_{1/3}Co_{1/3})O_3$ (system 2), $La_{1-x}Ca_x(Cr_{1/3}Mn_{1/3}Ni_{1/3})O_3$ (system 3), and

$La_{1-x}Ca_x(Cr_{1/3}Mn_{1/3}Fe_{1/3})O_3$ (system 4) for x=0-30 mol% were synthesized and tested for phase

evolution, microstructures and functional properties using XRD, SEM, and 4-probe conductivity

measurement. Also, the effects of doping Ca on the A-site and replacing the third B-site

transitional element (TM) with Co, Ni and Fe was studied. The results XRD showed the presence

of orthorhombic perovskite structure for all three systems, with secondary phases of La_2O_3 and

FeO present in system 4 when calcined at 950°C. Increasing the calcination temperature to

1050°C resulted in single-phase perovskite oxide powders. The lattice parameters and unit cell

volumes were affected by the introduction of Ca. SEM images showed distinct grain structures

with varying grain sizes and shapes depending on the sintering temperature and Ca substitution

levels. The addition of Ca was found to reduce porosity and improve grain homogeneity in

systems 2 and 3 but had a minimal effect on system 4. The sintered densities of systems 2 and 3

increased with increasing sintering temperature and Ca doping levels, reaching maximum

densities at different temperatures for each system.

The electrical conductivity of systems 2 and 3 increased linearly with temperatures, while

samples 4.1 and 4.2 stayed flat and displayed behavior similar to undoped $LaCrO_3$ and $LaMnO_3$.

System 2 recorded the highest overall electrical conductivity, and the addition of divalent Ca

(10-30 mol%) improved the conductivity. In systems 3 and 4, the addition of 10 mol% Ca^{+2}

reduced conductivity values by at least 10% due to the charge carrier trapping by Cr and Mn, but the addition of 20-30 mol% Ca^{+2} improved the conductivity. The activation energy was found to decrease with the increase of A-site substitution of Ca^{+2} in systems 2 and 3, while it varied for system 4. The results highlight that the addition of Ca^{+2} in MEPO systems can improve the electrical conductivity by creating +4 states of B-site elements, and the microstructure can be optimized through sintering temperature and Ca doping levels.

6.2 XRD results

XRD data of three perovskite oxide systems reveal the presence of an orthorhombic perovskite structure. Figure 6-1, Figure 6-2, and Figure 6-3 show the XRD results for the three systems. After calcining at 950°C for 8 hours, the XRD spectra of system 4 displayed secondary phases of La_2O_3 (hexagonal) and FeO (cubic) (see Figure 6-3). When the calcination temperature of the system 4 was increased to 1050°C for 9 hours, single-phase perovskite oxide powders were produced (see Figure 6-4). The unreacted secondary phases of La_2O_3 and FeO disappeared because of higher calcination temperature. The presence of La_2O_3 and FeO in all the compositions of system 4 calcined at 950°C suggests a partial reaction when calcined at this lower temperature.

Table 6-1 shows the lattice parameters and unit cell volumes of the systems 2, 3, and 4. The results highlight the reduction of lattice parameter values due to the incremental substitution of Ca^{+2} with La^{+3} on the A-site. This reduction is due to the smaller ionic radius of Ca^{+2} (1.34 Å) compared to that of La^{+3} (1.36 Å) in the same lattice site. Also, the prominent XRD peak (2θ values of 31.5-33.5°) of the systems 2, 3, and 4 deviates from its original position due to the substitution of Ca^{+2} in the A-site (see Figure 6-5). The single-phase perovskite oxide powders of

the systems 2, 3, and 4 are indexed based on the orthorhombic structures of LaCrO$_3$ Pnma,

LaCrO$_3$ Pbnm, and La$_{0.97}$Mn$_{0.97}$O$_3$ Pnma, respectively, with the space group 62.
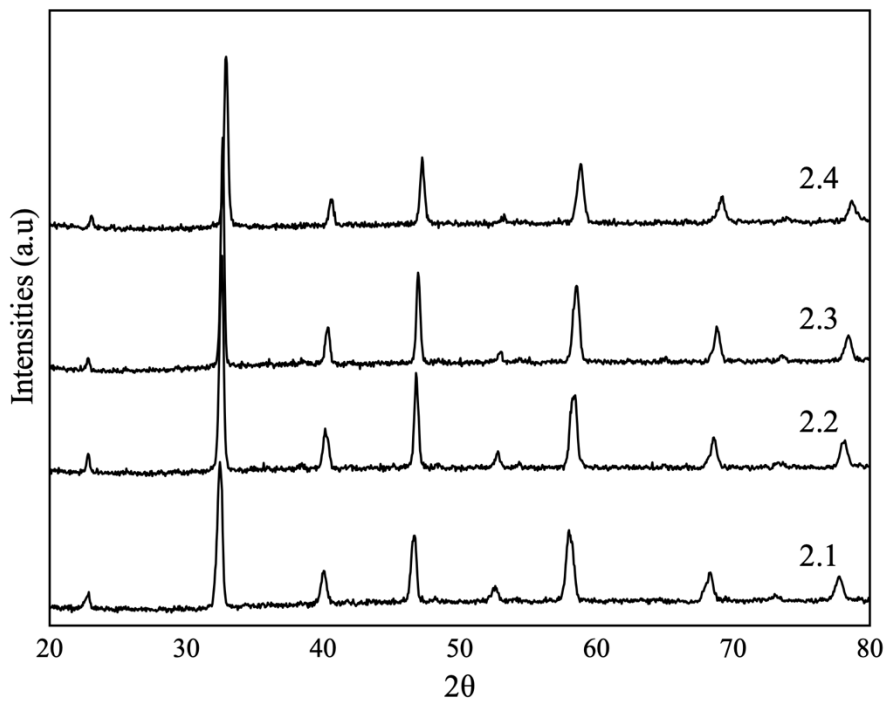
Figure 6-1 XRD patterns of system 2 calcined at 950°C for 9 hours
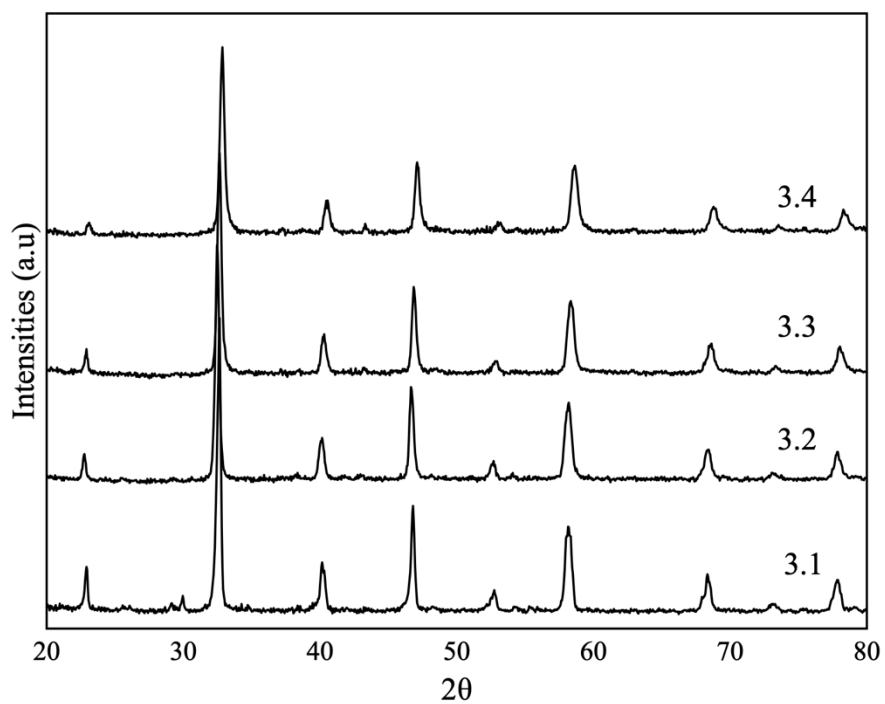
Figure 6-2 XRD patterns of system 3 calcined at 950°C for 9 hours
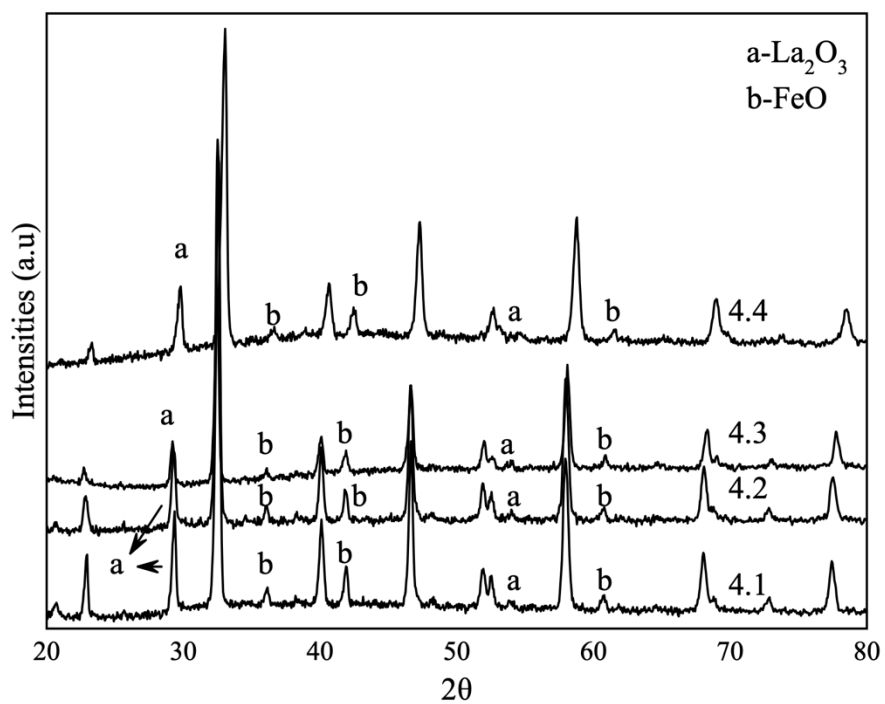
Figure 6-3 XRD patterns of system 4 calcined at 950°C for 9 hours

39
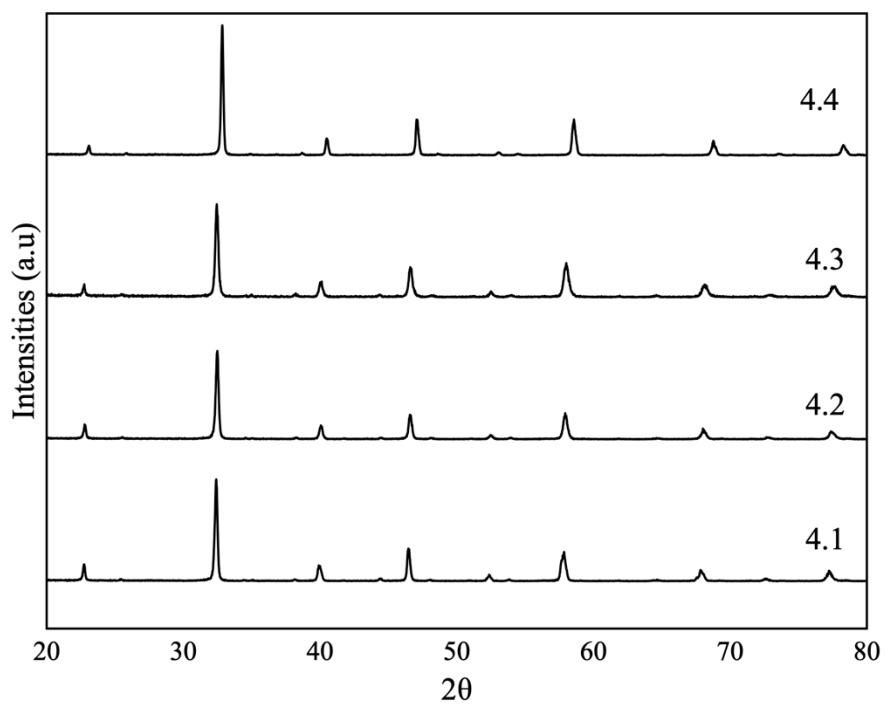
Figure 6-4 XRD patterns of system 4 calcined at 1050°C for 9 hours
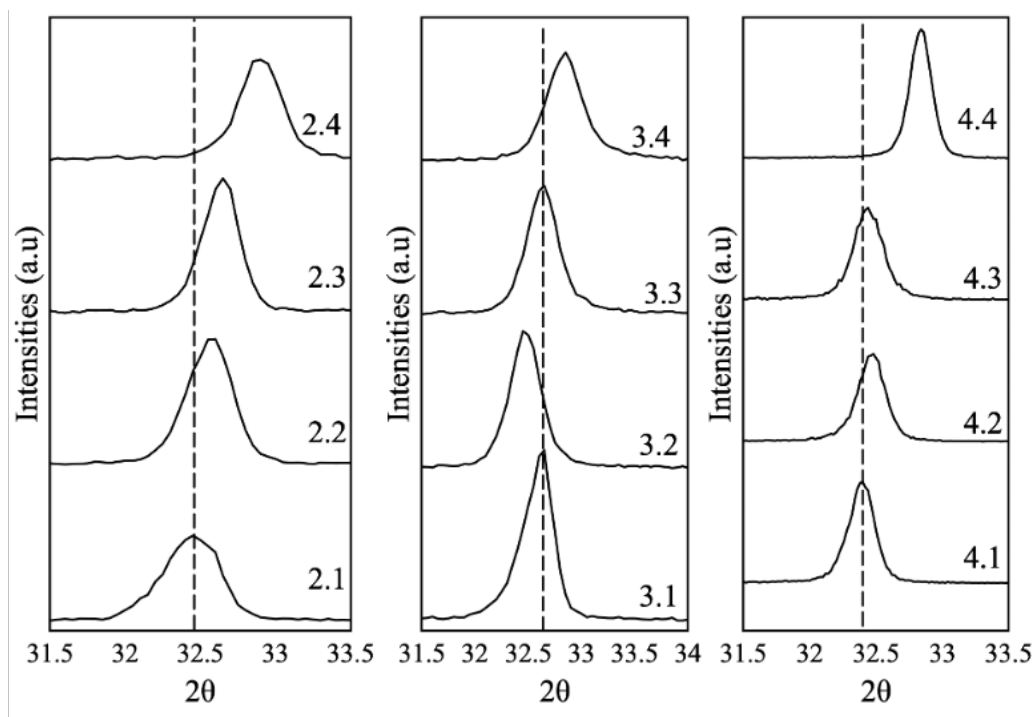
Figure 6-5 Magnified view of the major peak between 2θ values of 31.5-33.5°

Table 6-1 Lattice constants (a, b and c), unit cell volume, crystallite size and pseudo cubic lattice of systems 2-4

Compositions	Space group	a (Å)	b (Å)	c (Å)	Unit cell volume (Å³)	Crystallite size (nm)	Pseudo cubic lattice a_0 (Å)
2.1	Pnma	5.49	7.76	5.64	240.736	17.3634	3.91886
2.2	Pnma	5.47	7.75	5.56	235.869	27.4878	3.89227
2.3	Pnma	5.44	7.78	5.47	231.594	23.3987	3.86862
2.4	Pnma	5.41	7.75	5.44	227.971	19.1874	3.84834
3.1	Pbnm	5.49	5.66	7.79	241.856	22.4045	3.92493
3.2	Pbnm	5.47	5.59	7.77	237.327	22.0308	3.90028
3.3	Pbnm	5.46	5.6	7.74	236.449	19.7592	3.89547
3.4	Pbnm	5.4	5.58	7.72	232.631	16.8857	3.87438
4.1	Pnma	5.52	7.81	5.64	243.366	30.333	3.93308
4.2	Pnma	5.48	7.8	5.63	241.081	28.088	3.92074
4.3	Pnma	5.48	7.79	5.62	240.159	24.4968	3.91573
4.4	Pnma	5.43	7.73	5.56	233.457	34.2125	3.87896

The reflection positions of (002), (112), (202), (004), (141), (024), (025), and (116) were used for the calculation of unit cell parameters. The calculated unit cell volumes reduced linearly for all systems due to the doping of smaller Ca in the La lattice site. A similar trend was observed in other Ca-doped perovskite oxide powders [88–90]. In all three perovskite oxide systems, the a-axis shrank by 1.5%, the b-axis shrinkage was between 0.12-1.37%, and the c-axis shrinkage ranged from 0.9-3.8% with the addition of Ca^{+2} in the range of 10-30 mol%. The volume shrinkage was equivalent to the sum of lattice constant shrinkage. The unit cell volumes

of the oxide systems reduced when Fe was replaced with Ni and Co, with the decrement order of average ionic radii of B-site TM ions. Therefore, there is a correlation between the average ionic radii of B-site TMs and the unit cell volume.

6.2.1 Crystallite size
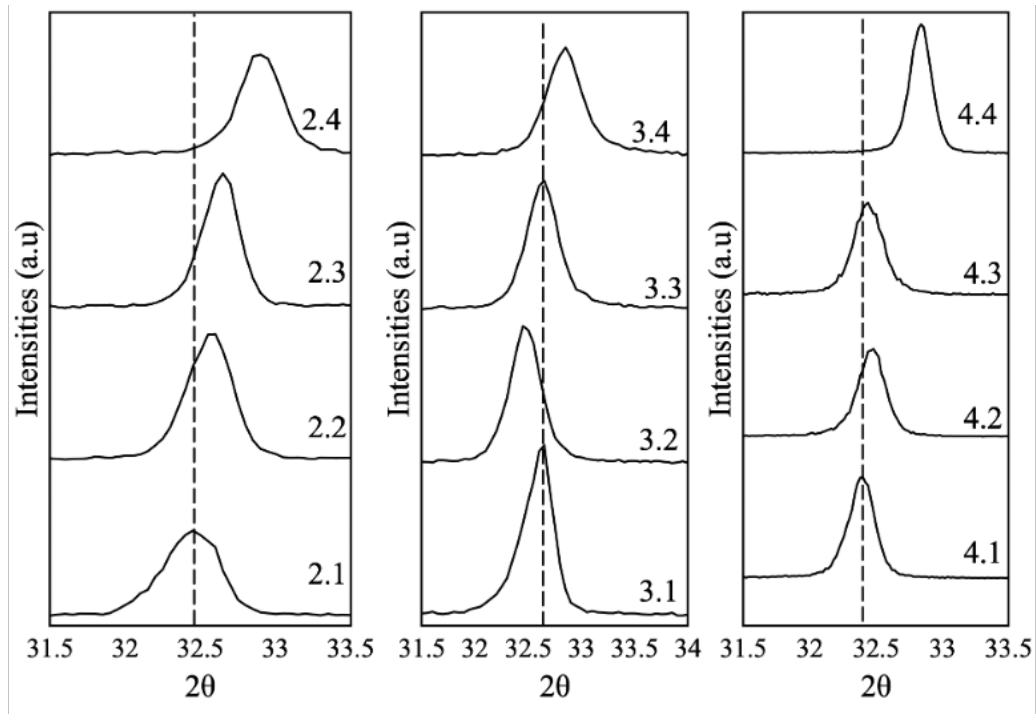
Figure 6-5 Magnified view of the major peak between 2θ values of 31.5-33.5°

Table 6-1 gives the average crystallite size calculated using the Debye-Scherrer's equation. There was a linear decrease in the calculated values in system 3, but this trend was not observed in the other two systems. It's worth noting that the average crystallite values of the undoped samples of systems 2, 3, and 4 decreased in the same order as the average ionic radii of the B-site cations.

6.2.2 Pseudo cubic lattice parameters

The pseudo cubic lattice parameters (a_0) of the present perovskite systems were calculated using the equation 9 and their values are given in Table 6-1. In general, the orthorhombic unit cell is four times that of the cubic unit cell. The values of the pseudo cubic lattice parameters of all three systems reduced due to the addition of Ca on the A-site. Interestingly, the obtained values of systems 2, 3, and 4 are in the same order as their average B-site ionic radii.

6.3 Sintering studies

The effects of doping on the A- and B-sites were studied by sintering systems 2, 3, and 4 at three different temperatures. Sintered discs were polished and thermally etched for microstructure study. Their SEM images are shown separately in Figure 6-6, Figure 6-7, and Figure 6-8. SEM micrographs show the creation of distinctive grains with various grain structures, such as hexagonal grains with rounded corners, coarsened grain structures, and connected grain-like structures. The following paragraphs explain the formation of different grain structures.

Calculated average grain sizes were found to vary in the sintered discs of all systems with respect to sintered temperatures and Ca partial substitution. The Ca-substituted discs' average grain size was more than Ca-undoped discs (see Table 6-2). The increased grain size is a result of the oxygen vacancies introduced by the substitution of Ca that led to the enhancement of grain growth [80]. The discs of all systems that were sintered at the initial temperature of 1200°C displayed the smallest grain size values. The average grain size of the discs sintered at 1300°C was slightly larger than that of the discs sintered at 1200°C and 1400°C; this discrepancy in size was a result of the grain reorganization during the intermediate sintering temperature.

Furthermore, the grain size of the discs sintered at 1400°C was found to be smaller than that of the discs sintered at 1300°C and larger than that of the discs sintered at 1200°C.

The SEM images of calcium-free discs of system 2 (see Figure 6-6) show the presence of non-homogeneous grain shapes along with the pores around the grain intersections in all discs sintered in different temperatures. Addition of calcium reduced the porosity drastically by 41% (see Table 6-3) and improved the grain homogeneity. The grains of calcium-doped discs have a slightly rounded hexagonal shape, which is typical of a perovskite oxide that has undergone liquid-phase sintering.
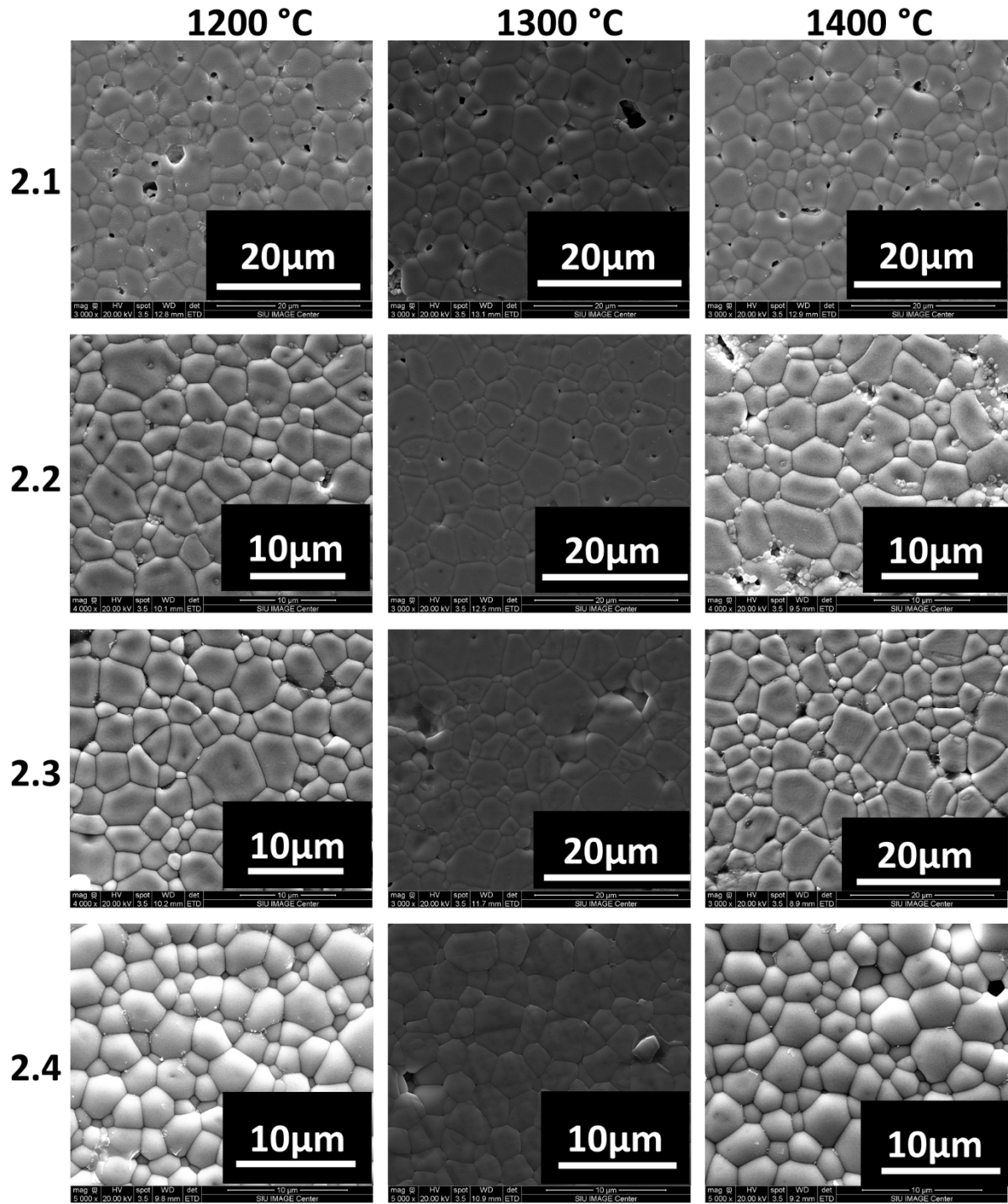
Figure 6-6 SEM images of polished and thermally etched pellets of system 2 MEPO
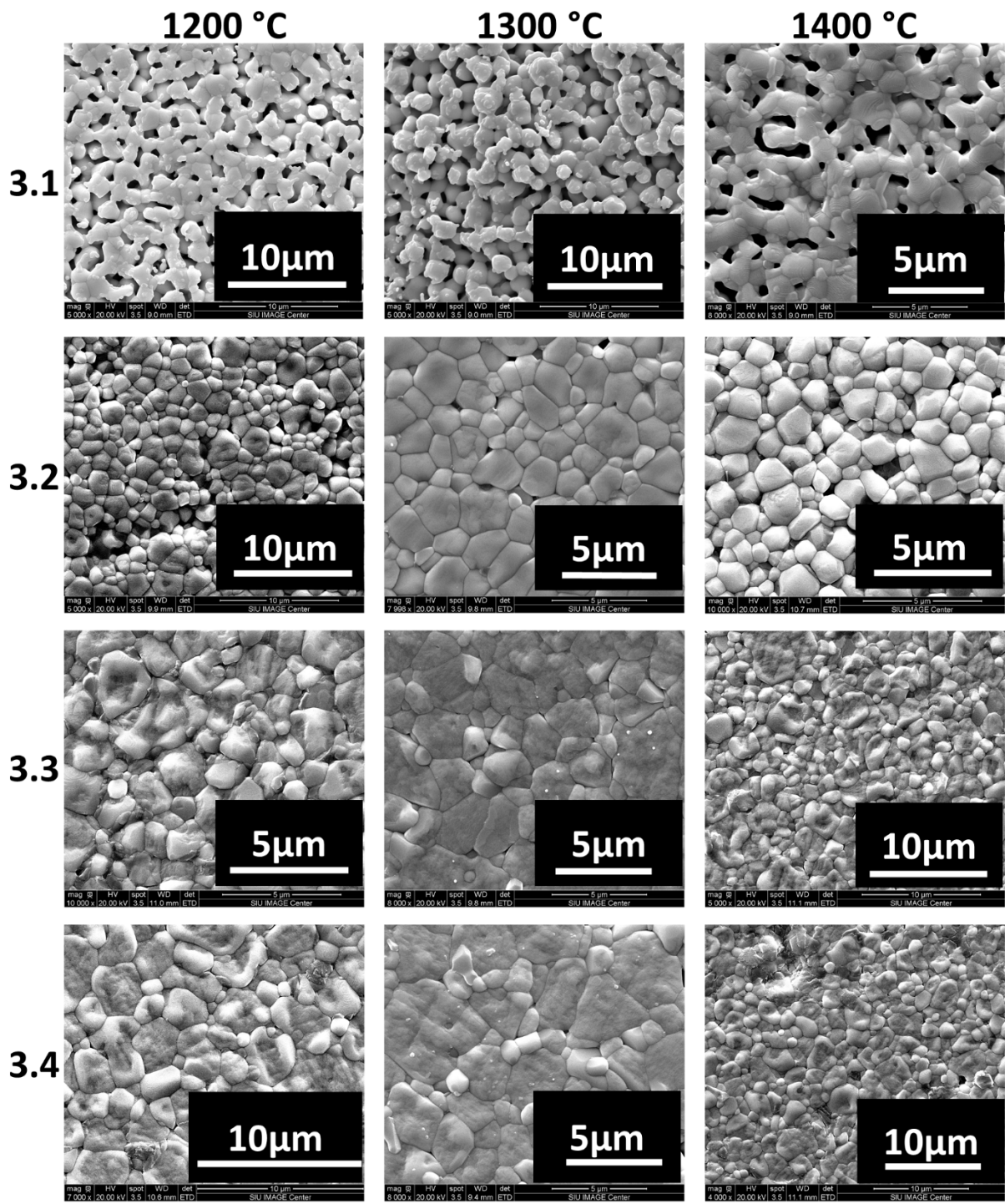
Figure 6-7 SEM images of polished and thermally etched pellets of system 3 MEPO
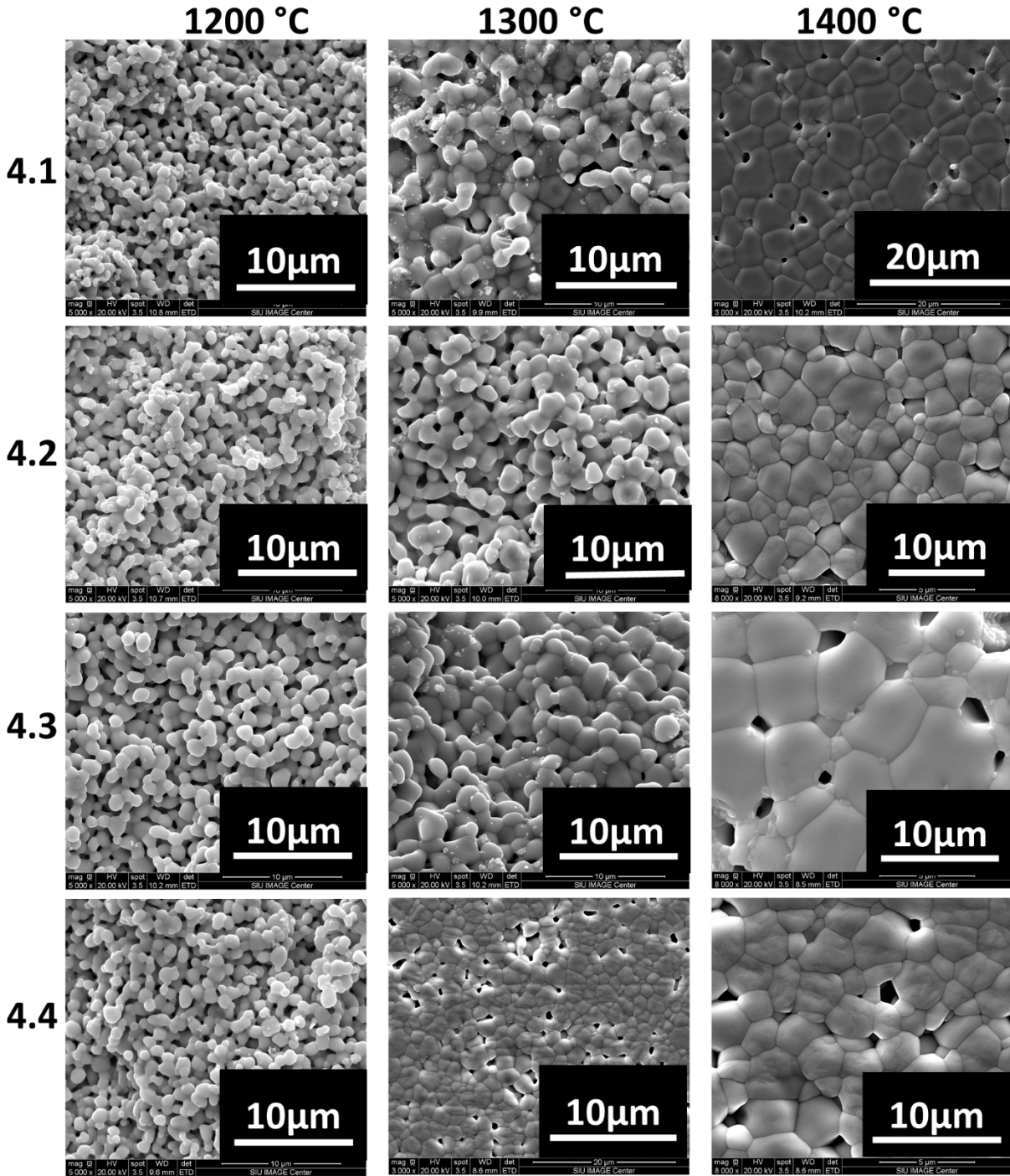
Figure 6-8 SEM images of polished and thermally etched pellets of system 4 MEPO

SEM images of calcium-free discs of system 3 (see Figure 6-7) sintered in different

temperatures show the presence of clustered grain shape along with open-interconnected pores.

The surface porosity reduced at least by 21% after adding calcium, and a uniform and rounded

grain structure is observed in the SEM images. Due to the round grain shape, it is believed that the discs of system 3 sintered through a transient liquid phase.

Figure 6-8 illustrates the SEM images of system 4 discs that have been sintered in three different temperature zones. The discs sintered at 1200 and 1300°C display a high level of surface porosity and the addition of calcium appears to have a minimal effect on the grain shape and size. Despite the addition of calcium, the porosity of these discs remains largely unchanged and does not demonstrate the same level of improvement observed in systems 1, 2, and 3.

All discs of system 2 and discs of system 3 with Ca 10 mol% were sintered in transient liquid phase at all temperatures. The transient liquid phase is evident from the rounded hexagonal grain structure of the SEM micrographs. Later system 3 discs with higher levels of Ca (20 and 30 mol%) underwent solid-state sintering as the liquid phase disappeared in the earlier stage of sintering due to the increased Ca substitution levels in all sintering temperatures. Transitioning to solid-state sintering is supported by the coarsening of grains in the micrographs (see Figure 6-7). Sintering temperatures were also found to affect the grain shape and relative densities of the system 3 discs.

Systems 2 and 3 sintered densities increased (shown in Table 6-3) as the sintering temperature and Ca doping levels increased. The initial addition of Ca (10 mol%) in systems 2 and 3 greatly improved the densities for all temperatures. The discs of system 2 attained their maximum sintered density at 1400°C. Disc 2.4 reached its highest TD of 90% after sintering at 1300°C and maintained the same density after sintering at 1400°C. The system 3 discs with varying amounts of Ca reached their maximum sintered density either at 1300°C (for 3.2 and 3.4 discs) or at 1400°C (for 3.1 and 3.3 discs) and achieved sintering densities of 83-88%TD. The

least amount of Ca needed to reach TD > 85% for system 3 and system 2 was 20 mol% and 30 mol%, respectively.

The sintered density of system 4 discs increased with the Ca substitution levels and sintering temperatures. Discs 4.1 and 4.2 achieved maximum sintered densities of 98 and 93% at 1400°C respectively. While disc 4.3 reached 99%TD after sintering at 1300°C and reduced to 96%TD density after sintering at 1400°C. The disc with the highest Ca level (4.4) fully densified at the initial sintering temp of 1200°C. Further increase in temperature reduced the sintering density.

The sintered density of system 4 was found to be higher than that of systems 2 and 3 across all temperatures, although system 4 showed high surface porosity. The high porosity and high sintered density observed in system 4 can be explained by the liquid-phase sintering process that the sample underwent. The presence of a greater amount of liquid phase during sintering is believed to have facilitated the densification process of these discs in all temperature regions. It has been observed that the addition of Ca improves the sintering properties by creating temperature-sensitive melting phases of B-site transitional elements, which melt at lower temperatures, forming a transient liquid phase that densifies the disc [91].

From the sintered density results of these three systems, it is clear that the amount of liquid phase varied due to Ca addition, and calcium's reaction with B-site elements and sintering temperatures. From the sintering studies, it is evident that the amount of Ca doping necessary to achieve TD greater than 85% is at least 10 mol% for all three systems.

Among all systems, the partial addition of Ca improved sintering properties. It is also observed that certain discs reached maximum sintering density at initial sintering temperatures, others reached highest sintering density at the intermediate sintering temperature, and the rest

reached highest sintering density at 1400°C. It's worth noting that the sintering temperatures play

a crucial role in the sintering process of the present systems.

Table 6-2 Average grain sizes of systems 2-4 pellets sintered at 1200, 1300, and 1400°C in atmospheric air for 2 hours

MEPO Samples	1200°C	1300°C	1400°C
2.1	2.25	3.4	2.2
2.2	2.35	3.62	2.33
2.3	2.67	3.88	3.5
2.4	2.23	2.34	2.28
3.1	0.91	1.06	1.12
3.2	0.98	1.52	1.23
3.3	1.28	1.67	1.82
3.4	1.24	2.09	1.83
4.1	0.85	1.98	3.05
4.2	1.07	1.82	1.3
4.3	1.25	1.8	1.36
4.4	1.1	1.33	1.66

Table 6-3 Relative sintered densities of systems 2-4 pellets sintered at 1200, 1300, and 1400°C in atmospheric air for 2 hours

MEPO Samples	1200°C	1300°C	1400°C
2.1	73	78	84
2.2	84	85	85
2.3	86	86	87
2.4	82	90	90
3.1	72	79	83
3.2	78	86	83
3.3	88	88	88
3.4	83	87	86
4.1	75	80	98
4.2	87	91	93
4.3	98	99	96
4.4	99	97	98

6.4 EDS maps

EDS spectra of the discs of systems 2, 3, and 4 fired at 1400°C for 2 hours are given in Figure 6-9 and their elemental compositions are shown in the Table 6-4. Moreover, their elemental compositions showed the presence of doped transitional elements of B-site and La and Ca on A-site.
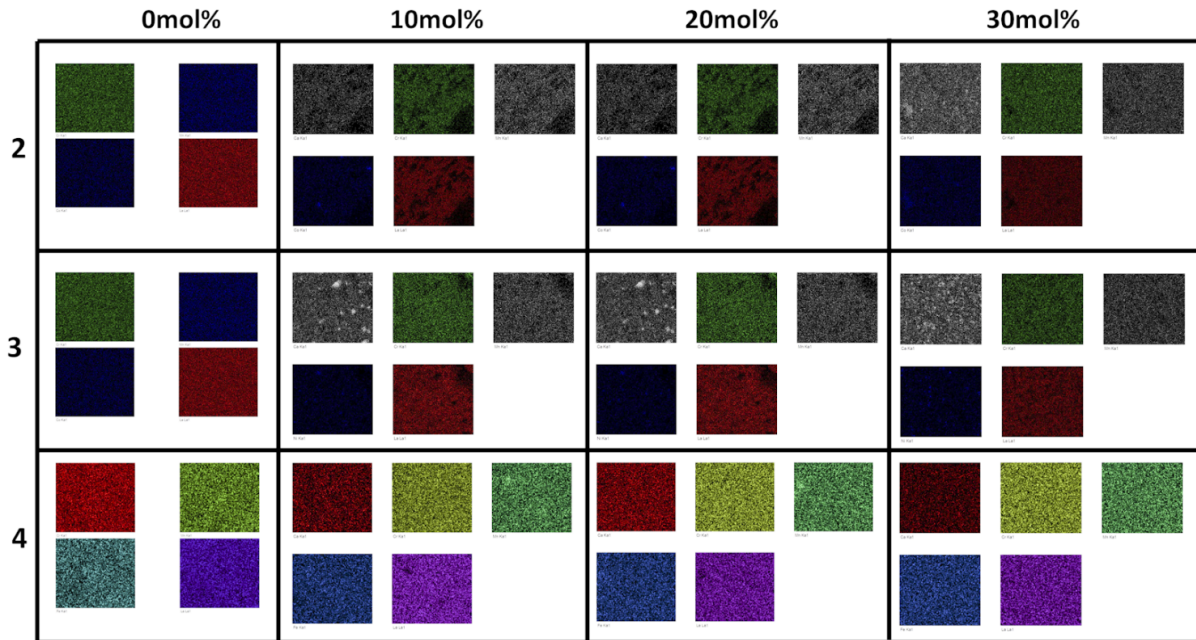
Figure 6-9 EDS mapping of systems 2-4 pellets sintered at 1400°C

Table 6-4 EDS elemental analysis of systems 2-4 sintered at 1400°C

MEPO samples	La (wt%)	Ca (wt%)	Cr (wt%)	Fe (wt%)	Mn (wt%)	Ni (wt%)	Co (wt%)
2.1	50.2	-	16.97	-	16.95	-	15.88
2.2	44.04	6.01	14.84	-	16.34	-	18.77
2.3	35.26	18.98	15.58	-	14.56	-	15.61
2.4	31.93	20.42	15.67	-	15.03	-	16.94
3.1	50.58	-	16.42	-	15.61	17.39	-
3.2	40.03	12.49	15.43	-	15.67	16.38	-
3.3	35.95	20.47	14.6	-	13.67	15.31	-
3.4	31.74	23.74	15.14	-	15.13	14.25	-
4.1	49.58	-	15.3	17.91	17.2	-	-
4.2	44.17	5.22	15.66	17.93	17.03	-	-
4.3	39.97	10.45	14.57	18.09	16.92	-	-
4.4	34.16	16.09	15.18	17.97	16.6	-	-

6.5 Temperature dependence electrical conductivity

Electrical conductivity graphs of MEPO systems 2-4 obtained over the temperature range of 300-900°C are shown in Figure 6-10. The electrical conductivity of the MEPO materials displayed linearity over the temperature range of 300-900°C, except for 4.1 and 4.2. The electrical conductivity of 4.1 and 4.2 materials remained at around 0.5 S/cm up to a temperature of 500°C, displaying a behavior similar to that of undoped $LaCrO_3$ and $LaMnO_3$ [56]. However, the electrical conductivities of 4.1 and 4.2 later increased and exhibited a thermally activated behavior, similar to the rest of the materials. This thermally activated behavior is typical for high-temperature semiconductors where the charge is transported through the hopping of small

polarons among B-site transition metal ions. Equation 10 was used to calculate the activation

energies of these thermally activated materials obtained from the slopes of linear graphs.

Calculated activation energies are given in Table 6-5.
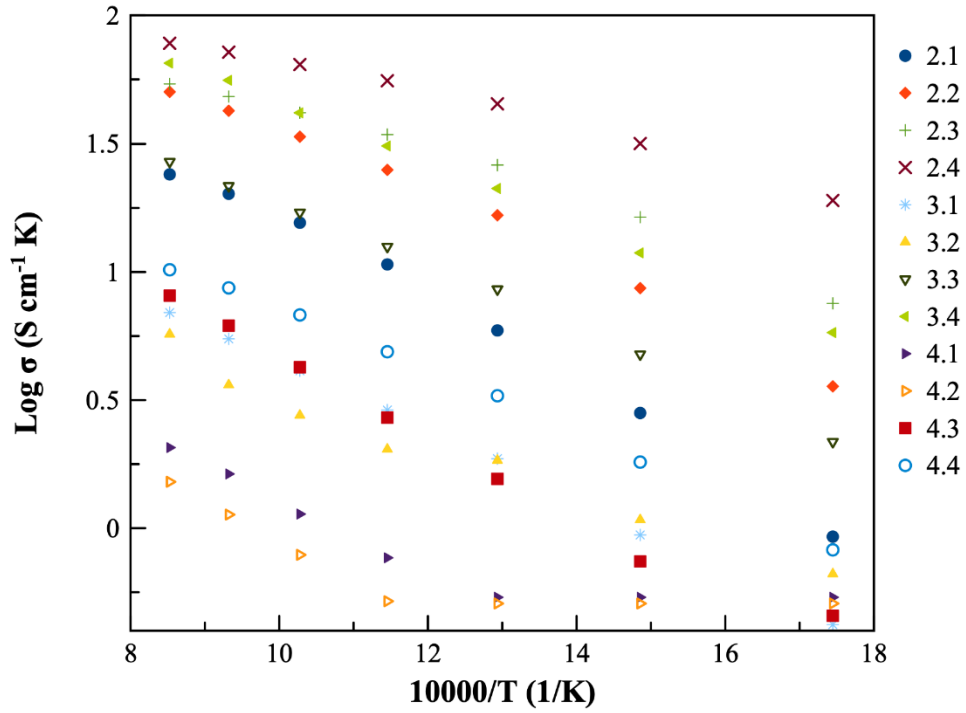
Figure 6-10 Log σ vs. 10000/T of MEPO systems 2-4
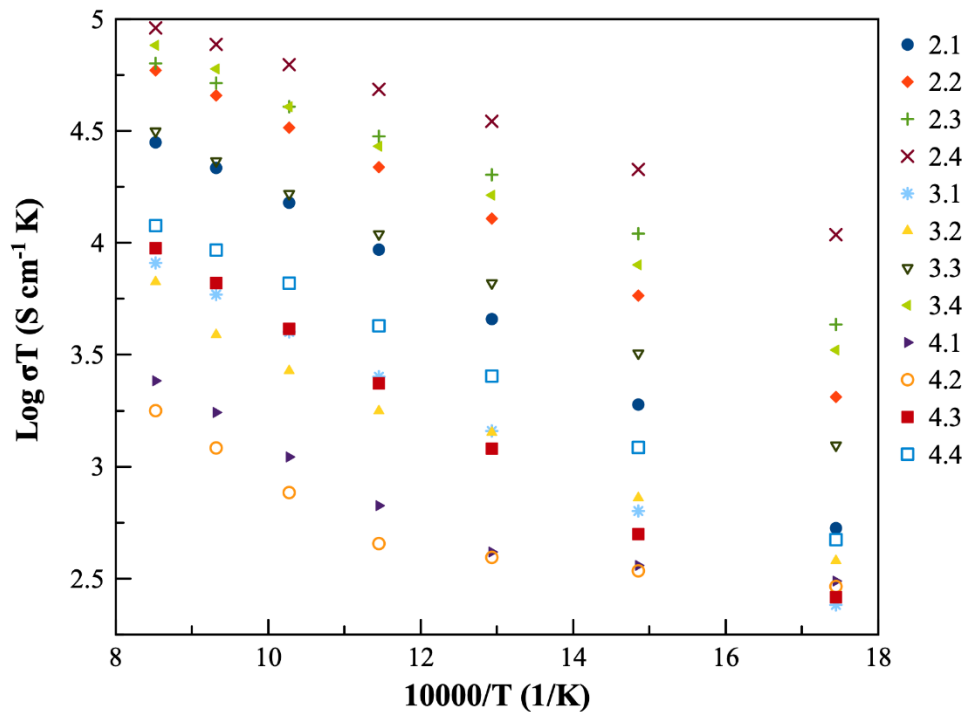
Figure 6-11 Arrhenius graphs of MEPO systems 2-4
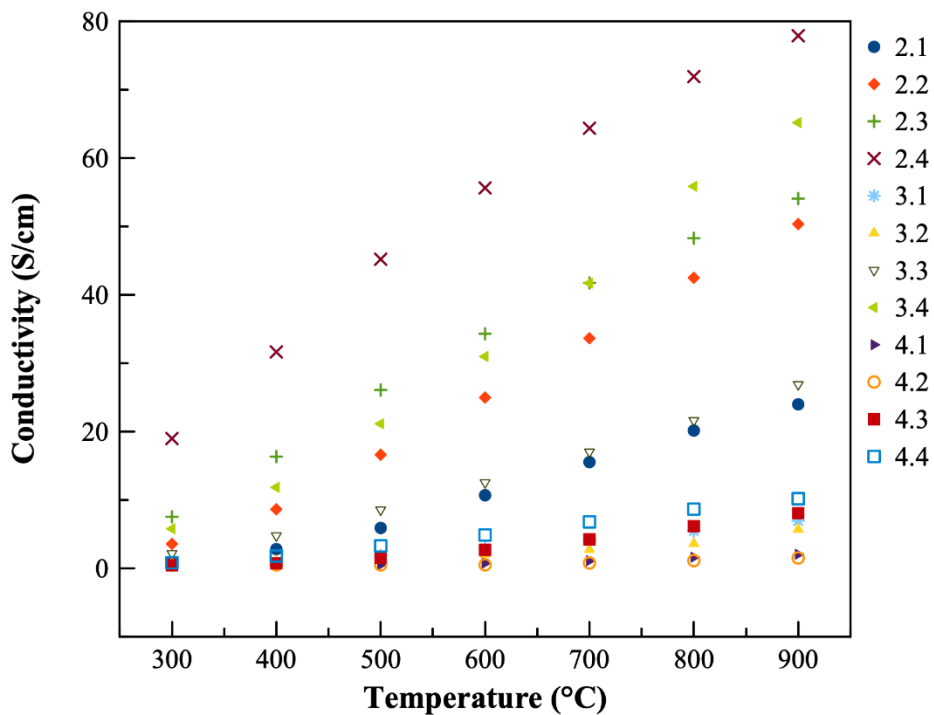
Figure 6-12 Electrical conductivity vs. temperature of MEPO systems 2-4

Table 6-5 Apparent electrical conductivity, activation energies of MEPO systems 2-4 at 800°C in atmospheric air

MEPO Systems	Conductivity at 800°C (S/cm)	Activation energies (eV)
2.1	20	1.68
2.2	43	1.41
2.3	48	1.11
2.4	72	0.89
3.1	5.5	1.48
3.2	4	1.44
3.3	22	1.35
3.4	56	1.3
4.1	1.7	0.88
4.2	1.5	0.726
4.3	6.2	1.56
4.4	8.7	1.36

Of the three MEPO systems discussed in this chapter, system 2 recorded the highest overall electrical conductivity. Among undoped materials, sample 2.1 possesses the highest electrical conductivity value of 20 S/cm at 800°C when compared to the undoped samples of system 3 and 4. The initial addition of divalent Ca (10 mol%) in system 2, doubled the electrical conductivity at 800°C. Further addition of Ca in the range of 20 and 30 mol% has enhanced the conductivity (48 and 72 S/cm, respectively). Like other MEPO systems in the present study, substitution of Ca^{+2} for La^{+3} in system 2 creates a charge disproportion. To counter this, either +4 states of B-site elements or oxygen ions are formed. Electrical conductivity numbers are

expected to rise if the charge disproportion is countered by the creation of +4 states of B-site elements rather than the formation of O^{-2}. The addition of Ca^{+2} created +4 states of Cr, Mn, and Co ions and improved the conductivity of system 2. Another reason for the high electrical conductivity values of system 2 materials is the presence of two low-energy sites of Mn and Co in the oxide series rather than just one low-energy Mn site in systems 3 and 4 [92]. Activation energies of system 2 reduced gradually with the incremental additions of Ca^{+2}.

In systems 3 and 4, substituting Ca 10 mol% (samples 3.2 and 4.2) reduced the conductivity values by at least 10% in comparison to their Ca-free samples. The suppression of conductivity is believed to be due to the trapping of small polarons by the +2 and +4 pairs of B-site elements. As a result, adding 10 mol% Ca does not fully complete the charge balance mechanism and does not produce conductive polarons in systems 3 and 4. However, substituting 20 mol% Ca^{+2} (samples 3.3 and 4.3), the conductivity numbers increased by four times. Furthermore, the substitution of 30 mol% Ca^{+2} (samples 3.4 and 4.4) improved the conductivity numbers by 14 and 6 times compared to samples 3.2 and 4.2, respectively (see Table 6-5). This is because the addition of 20 and 30 mol% Ca^{+2} in systems 3 and 4 compensates the charge imbalance by producing +4 states of B-site elements, which enhances conductivity.

The activation energy obtained from the line slopes of Figure 6-11 was found to decrease with the increase of A-site substitution of Ca^{+2} in systems 2 and 3. For system 4, the activation energy reduced for 4.2, increased for 4.3, and later decreased for 4.4. An increase in activation energy of system 4 samples can be due to the trapping of conductive polarons among the energetically lower Mn and Cr sites. Similar observations were made in the mixed oxides of $LaMnO_3$ [91,93] and Ca-doped $LaCrO_3$ [94]. When the concentration of Cr and Mn is lower than 30%, Cr^{+2}-Cr^{+4}, Mn^{+2}-Mn^{+4} pairs trap the polarons produced at the adjacent B-

site elements, causing the increase of activation energy (and reduction of conductivity). The trapping mechanism of the polaron was controlled when the concentrations of energetically lower sites were greater than 31% or increased in the doping levels of a divalent cation such as Ca and Sr on A-site [99, 101–103]. A similar trapping mechanism might be affecting the conductivity of system 4 series, i.e., Cr and Mn pairs trapping the polarons produced by the Fe ions. Reduced conductivity values and increased activation energy for 4.3 and 4.4 materials support this assumption.

6.6 Conclusions

In conclusion, XRD data of three perovskite oxide systems 2, 3, and 4 showed the presence of an orthorhombic perovskite structure, and secondary phases of La_2O_3 and FeO were present when system 4 was calcined at 950°C. Increasing the calcination temperature to 1050°C resulted in single-phase perovskite oxide powders. The lattice parameters and unit cell volumes of all three systems were affected by the introduction of Ca^{+2}, with a reduction in values and a correlation between average ionic radii of B-site TMs and unit cell volume. The average crystallite size also decreased linearly in system 3. The pseudo cubic lattice parameters of all systems were also reduced as a result of Ca doping.

The effects of doping on the A and B-sites of perovskite oxide systems 2, 3, and 4 were studied by sintering at different temperatures and observing the resulting microstructures. SEM images showed the formation of distinct grain structures, with varying grain sizes and shapes depending on the sintering temperature and Ca substitution levels. The addition of Ca led to a reduction in porosity and improved grain homogeneity in systems 2 and 3 but had minimal effect on system 4. The SEM images also showed that systems 2 and 3 sintered through a transient liquid phase at lower temperatures but transitioned to solid-state sintering at higher temperatures

58

and higher levels of Ca substitution. The sintered densities of systems 2 and 3 increased with increasing sintering temperature and Ca doping levels, reaching maximum densities at different temperatures for each system.

The electrical conductivity results showed linearity from 300-900°C, except for 4.1 and 4.2, which displayed a behavior similar to undoped $LaCrO_3$ and $LaMnO_3$. System 2 recorded the highest overall electrical conductivity, and the addition of divalent Ca (10-30 mol%) improved the conductivity. The addition of Ca^{+2} created +4 states of Cr, Mn, and Co ions in system 2 and improved the conductivity. In systems 3 and 4, the addition of 10 mol% Ca^{+2} reduced the conductivity values by at least 10% but the addition of 20-30 mol% Ca^{+2} improved the conductivity. The activation energy decreased with the increase of A-site substitution of Ca^{+2} in systems 2 and 3, while it varied for system 4. Overall, the results show that the addition of Ca^{+2} in MEPO systems can improve the electrical conductivity by creating +4 states of B-site elements.

CHAPTER 7

STUDY OF MICROSTRUCTURE AND ELECTRICAL CONDUCTIVITY OF CALCIUM-

SUBSTITUTED $La(Cr_{1/3}Fe_{1/3}Co_{1/3})O_3$, $La(Cr_{1/3}Ni_{1/3}Co_{1/3})O_3$ and $La(Fe_{1/3}Ni_{1/3}Co_{1/3})O_3$ MEPO SYSTEMS

7.1 Introduction

In this chapter, the crystal structures, electrical conductivities, and sintered densities of

three mixed rare earth perovskite oxide systems, $La_{1-x}Ca_x(Cr_{1/3}Fe_{1/3}Co_{1/3})O_3$ (system 5),

$La_{1-x}Ca_x(Cr_{1/3}Ni_{1/3}Co_{1/3})O_3$ (system 6) and $La_{1-x}Ca_x(Fe_{1/3}Ni_{1/3}Co_{1/3})O_3$, (system 9) were

investigated with varying levels of Ca doping. XRD results indicated that the addition of Ca

caused a transition from a rhombohedral to an orthorhombic phase in systems 6 and 9, attributed

to the reduction of weighted average of A-site ionic radii. Furthermore, the electrical

conductivity of these systems was found to be driven by small polaron hopping, with the addition

of Ca increasing the conductivity and reducing the activation energy. In addition to these

electrical properties, the study also investigated the impact of Ca doping on the sintered densities

and grain growth of the pellets. The results showed that the addition of Ca improved sinterability

by forming a transient liquid phase, and that the Ca presence and sintering temperatures played a

crucial role in the sintered densities and grain growth.

7.2 XRD results

Figure 7-1, Figure 7-2, and Figure 7-3 depict the XRD graphs of systems 5, 6, and 9. All

powders of the MEPO systems were calcined at 950°C for 9 hours. System 5 was indexed

according to an orthorhombic perovskite phase of $LaFe_{0.6}Co_{0.4}O_3$ (Pnma, space group: 62, COD

#00-044-0362). The peaks were indexed as follows (002), (112), (202), (004), (024), (025), and

(116). After calcination at 950°C, the powders of Ca 0-20 mol% showed a single phase, while

the powder with 30 mol% Ca showed a minor cubic phase of Cr (Im3m, 229, 01-085-1336). The

60

absence of extra peaks in Ca 0-20 mol% samples indicated the reaction was complete. The main

peak (30-35) of the present MEPO system deviated from the original position due to the addition

of Ca (as shown in Figure 7-4).
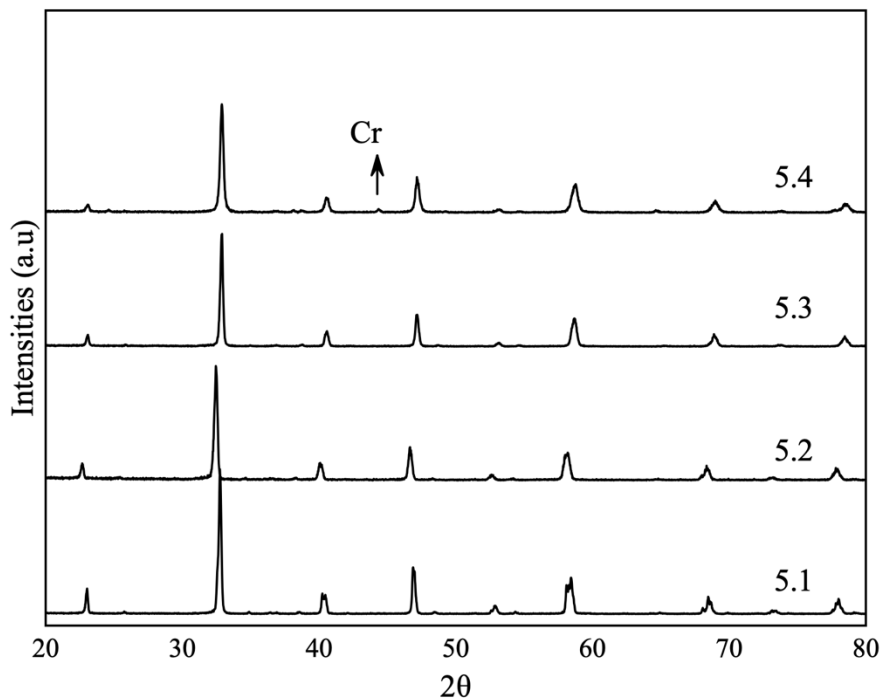
Figure 7-1 XRD patterns of system 5 calcined at 950°C for 9 hours in atmospheric air
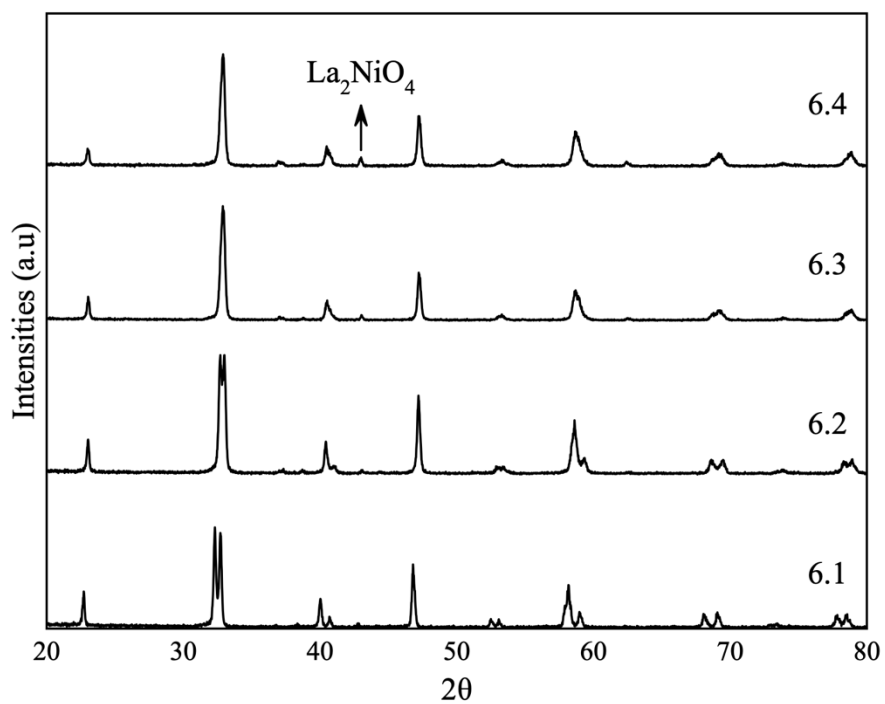
Figure 7-2 XRD of patterns system 6 calcined at 950°C for 9 hours in atmospheric air
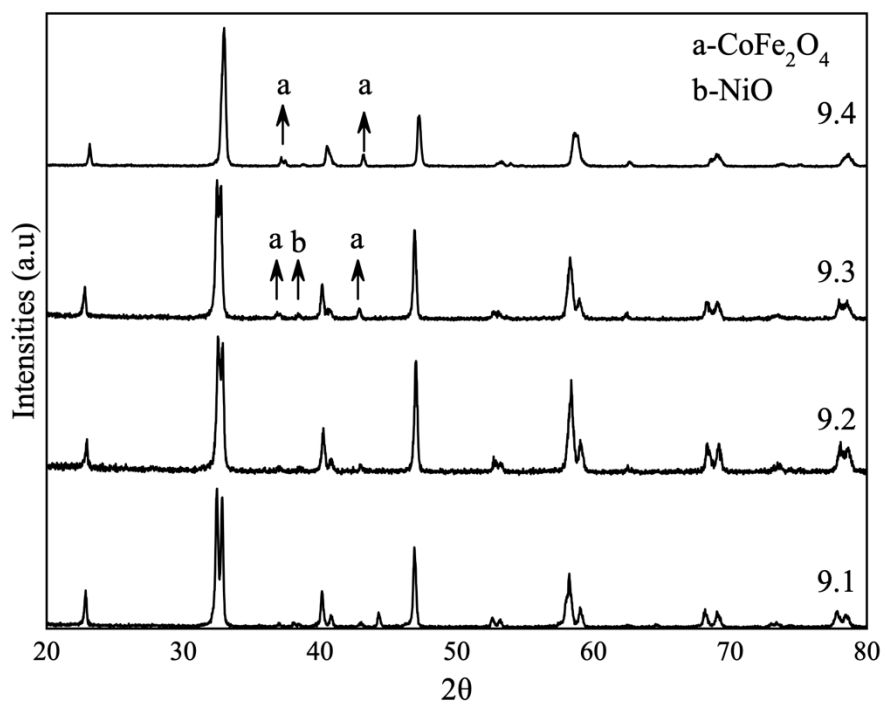
Figure 7-3 XRD of patterns system 9 calcined at 950°C for 9 hours in atmospheric air
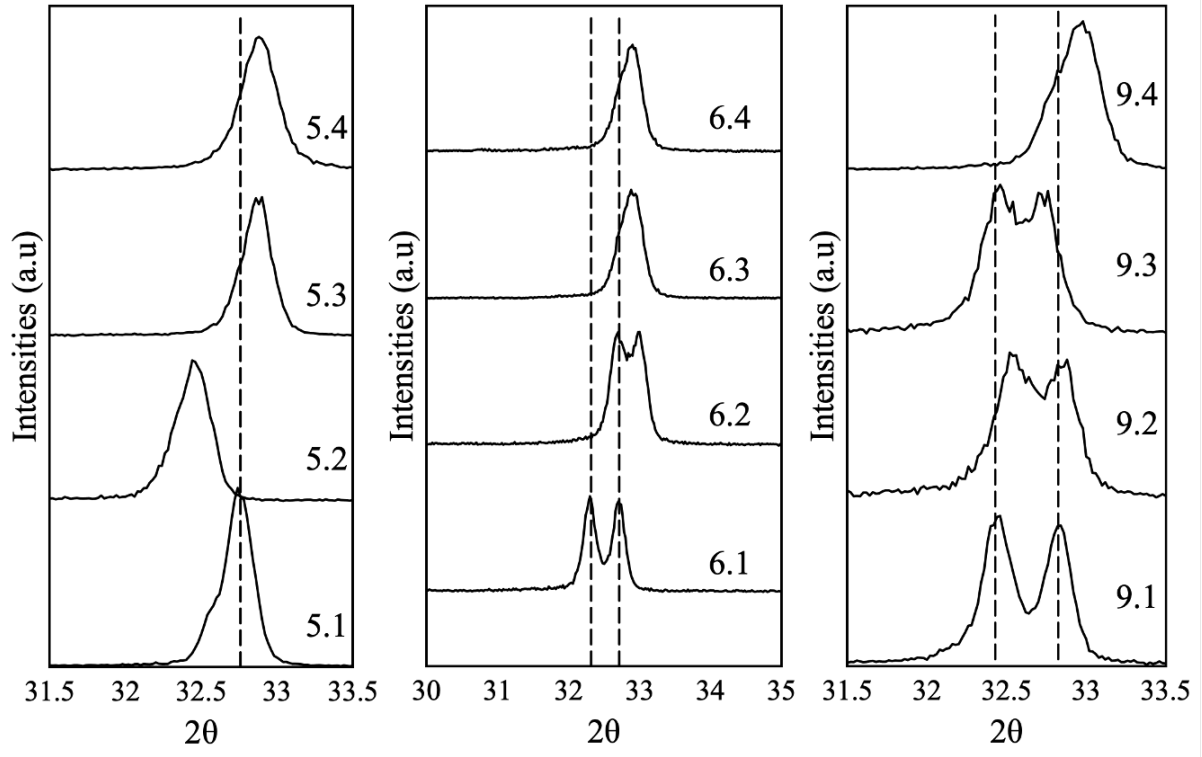
Figure 7-4 Magnified view of the major peak between 2θ values of 30-35° of systems 5, 6, and 9

Table 7-1 Structural properties of systems 5, 6, and 9

Compositions	Space group	a (Å)	b (Å)	c (Å)	Unit cell volume (Å³)	Crystallite size (nm)	Pseudo cubic lattice a_0 (Å)
5.1	Pbnm	5.49354	5.60691	7.76793	239.2664	30.82	3.9108
5.2	Pbnm	5.39354	5.59691	7.74793	233.8879	27.28	3.8813
5.3	Pbnm	5.41562	5.56487	7.71222	232.4251	24.36	3.8732
5.4	Pbnm	5.43.064	5.54244	7.71032	232.0730	21.72	3.8712
6.1	R$\bar{3}$c	5.62507	5.59025	13.2662	357.0383	32.93	3.9041
6.2	R$\bar{3}$c	5.49347	5.55516	13.4035	351.790	27.73	3.8848
6.3	Pbnm	5.42849	5.60004	7.67938	233.4513	26.86	3.8789
6.4	Pbnm	5.446	5.53376	7.68914	231.7265	22.10	3.8693
9.1	R$\bar{3}$c	5.60462	5.5789	13.2779	355.2544	35.98	3.8975
9.2	R$\bar{3}$c	5.57988	5.57119	13.25435	353.1368	32.6	3.8898
9.3	R$\bar{3}$c	5.55886	5.54542	13.2444	351.371	29.89	3.8833
9.4	Pbnm	5.43647	5.59601	7.69378	234.0646	20.93	3.8823

When x=0-0.1 (for 0-10 mol% Ca) in system 6, and (for 0-20 mol% Ca) in system 9, the powders' crystal structure was in the rhombohedral phase, and their peaks were similar to La(Cr$_{0.6}$Ni$_{0.4}$)O$_3$ (R$\bar{3}$c, space group: 167, COD #01-087-0016). As the Ca level increased to x=0.2 and 0.3 in system 6, the crystal structure of the powders changed to the orthorhombic phase, which is the same crystal structure as La$_{0.8}$Ca$_{0.2}$CrO$_3$ (Pbnm, space group: 62, COD #01-086-1134). The powder with x=0.3 had an additional minor orthorhombic phase of the spinel La$_2$NiO$_4$ (Bmab, space group: 64, COD #01-087-0217). On the other hand, when x=0.3 in system 9, the powders' crystal structure transitioned to an orthorhombic main phase similar to

64

La$_{0.8}$Ca$_{0.2}$CrO$_3$ (Pbnm, space group: 62, COD #01-086-1134), and also comprises very weak

peaks of CoFe$_2$O$_4$ (R$\bar{3}$m, space group: 166, COD #01-079-1744) and NiO (Fm$\bar{3}$m, space group:

225, COD #01-073-1523), a B-site spinel phase with rhombohedral and cubic symmetries. The

crystal structure transition can be attributed to the incremental substitution of Ca in the A-site

that reduced the weighted average of A-site ionic radii and changed the cell symmetry from

rhombohedral (low symmetry) to orthorhombic (high symmetry).

For 6 (0-10 mol% Ca) and system 9 (0-20 mol% Ca), system the rhombohedral structure

peaks of (012), (110), (104), (202), (006), (024), (214), (018), (208), (134), and (128) were used

to calculate unit cell volume, and lattice parameters. For 6.3 (Ca 20 mol%), 6.4 (Ca 30 mol%),

and 9.4 (Ca 30 mol%) orthorhombic structural peaks (002), (112), (202), (004), (024), (025), and

(116) (similar to system 5) were used to calculate structural parameters. The calculated crystal

structure parameters of MEPO systems 5, 6, and 9 are listed in Table 7-1. It is evident that the

increase in Ca changed the crystal structure of systems 6 and 9 from rhombohedral to

orthorhombic. The crystal structure changes from rhombohedral to orthorhombic in system 6 for

x = 0.2, 0.3 and in system 9 for x=0.3. The deviation of the prominent peak suggests a change in

the unit cell volume.

7.2.1 Unit cell volume

The calculated lattice constants, unit cell volumes, and pseudo lattice constants of the

MEPO systems 5, 6 and 9 (obtained using equation 9, Z=6 for rhombohedral and Z=4 for

orthorhombic) are given in Table 7-1. All structural parameters are reduced with the introduction

of Ca^{+2} and tend to change with respect to the average ionic radii of B-site dopants. The

reduction in structural parameters regarding Ca doping is due to the lower ionic radii of Ca^{+2}

(1.34Å) compared to that of La^{+3} (1.36Å) in the same lattice site. Also, doping Ca in fractional

amounts in systems 6 and 9 changes their crystal structure from rhombohedral to orthorhombic.

The lattice parameters in c-axis and unit cell volumes were also impacted. A similar behavior

change was observed in materials with Ni and Co on the B-site [96]. In system 5, cell volume

shrunk by 3% (for Ca 30 mol% powder) compared to its undoped counterpart.

7.2.2 Crystallite size

Table 7-1 shows the average crystallite size of different compositions of the prepared

perovskites. The average crystallite size was obtained from the XRD peaks using Scherrer's

equation. For all systems, the average crystallite size followed a decreasing trend (similar to the

lattice parameters and unit cell volume) with smaller levels of Ca^{+2} doping. The decreasing trend

is due to the smaller Ca^{+2} (1.34Å) replacing larger La^{+3} (1.36Å).

7.3 SEM studies

The sintering properties of systems 5, 6, and 9 were studied by sintering pressed pellets at

1200, 1300, and 1400°C in atmospheric air for 2 hours. The sintered densities of the pellets are

given in Table 7-2, and the SEM micrographs of the sintered pellets are shown in Figure 7-5,

Figure 7-6, and Figure 7-7. In the present study, Ca was incorporated on the A-site and three TM

ions of (Cr, Fe, Co), (Cr, Ni, Co), and (Fe, Ni, Co) on the B-site to improve the sintering

properties in atmospheric air. Past studies proved that the presence of Ca and Co improves

sintering properties by forming a transient liquid phase and enabling pressure less sintering in air

below 1400°C [53]. A similar effect was observed in the present study.

Table 7-2 shows the sintered densities of systems 5, 6, and 9. The overall sintered

densities of the pellets of system 5, 6, and 9 at all temperatures are in the order of 5 > 9 > 6. For

system 5, the sintered density of the Ca-free pellets increased from 90% TD at 1200°C to 97%

TD at 1400°C. In contrast, the sintered densities of Ca-free pellets of systems 6 and 9 showed no

increase in their densities with a change in temperatures (see Table 7-2). For Ca-free pellets of system 6, the sintered density reached 65% TD at 1200°C. However, a further rise in temperature reduced the sintered density. For undoped pellets of system 9, the sintered densities at all temperatures stayed the same (68% TD). This indicates that at these temperatures the Ca-free pellets of systems 6 and 9 could not be sintered to the required densities pressurelessly.

The sintered density of the 10 mol% Ca pellet of system 5 slightly increased after sintering at 1200°C. When sintering at 1300 and 1400°C, the sintering density further increased to 98 and 99% TD, respectively. This increase in sintered density suggests that a small amount of 10 mol% Ca is sufficient to enhance the sinterability of the pellets. However, when the Ca addition level was increased to 20 and 30 mol%, the sintered densities decreased slightly. This decrease may be attributed to the rapid evaporation of the liquid phase or reduced formation of the liquid phase. The SEM images of the pellets with 20 and 30 mol% Ca reveal that they were sintered in a transient liquid-phase sintering process, as evidenced by the microstructure (see Figure 7-5).

It is worth mentioning that doping of Ca is known to improve sinterability by forming low-temperature melting phases with B-site dopants that melt with rising temperatures, creating a transient liquid phase that densifies the pellets and evaporates at high temperature [53, 105]. In systems 6 and 9, adding Ca with La in 10 and 20 mol% did not improve the sinterability much, but 30 mol% of Ca improved sintering densities drastically (see Table 7-2). The sintered densities of 30 mol% pellets of systems 6 and 9 (6.4 and 9.4) increased by 35% at all temperatures compared to 20 mol% Ca pellets. This indicates that the least amount of Ca with La must be 30 mol% to reach the maximum densities of 96-99%TD when sintered between 1200-1400°C.

To understand the impact of Ca doping on the sintering mechanism of all three MEPO systems, the sintered pellets' grain structure was analyzed through SEM. All sintered pellets were polished and thermally etched for 1 hour at 100°C below their sintering temperatures for SEM analysis. The results are shown in Figure 7-5, Figure 7-6, and Figure 7-7. All SEM images show microstructure formation. Table 7-3 details the average grain size obtained using the line intercept method. The average grain size of the undoped pellets of all three systems showed an increasing trend with temperature. A similar trend was observed for systems 6 and 9 with varying Ca levels.

In contrast, in system 5 the trend was different. The average grain size reduced with an increase in Ca addition. This is likely due to the reduction of oxygen vacancies that reduced the grain growth [80]. The SEM images and calculated grain sizes show that the Ca presence and sintering temperatures played an essential role in the sintered densities and grain growth. SEM images of system 5 show a wide range of grain shapes, including well-rounded boundaries, linear, dendrite cubic structure, well-connected grain structure, and agglomerated grain structure. The SEM images show less surface porosity, which is in agreement with sintered density data. Pellets sintered at 1400°C recorded the largest grain size, while pellets sintered at 1200°C recorded the smallest grain size (see Table 7-3). The data on sintered density and grain size suggest that the pellets were sintered in a transient liquid phase. The liquid phase increased with an increase in temperature. However, sintered densities of the pellets sintered at 1300°C and 1400°C reduced slightly with an increase in Ca content above 10 mol%, indicating the formation of a slightly lower liquid phase to promote liquid phase sintering.
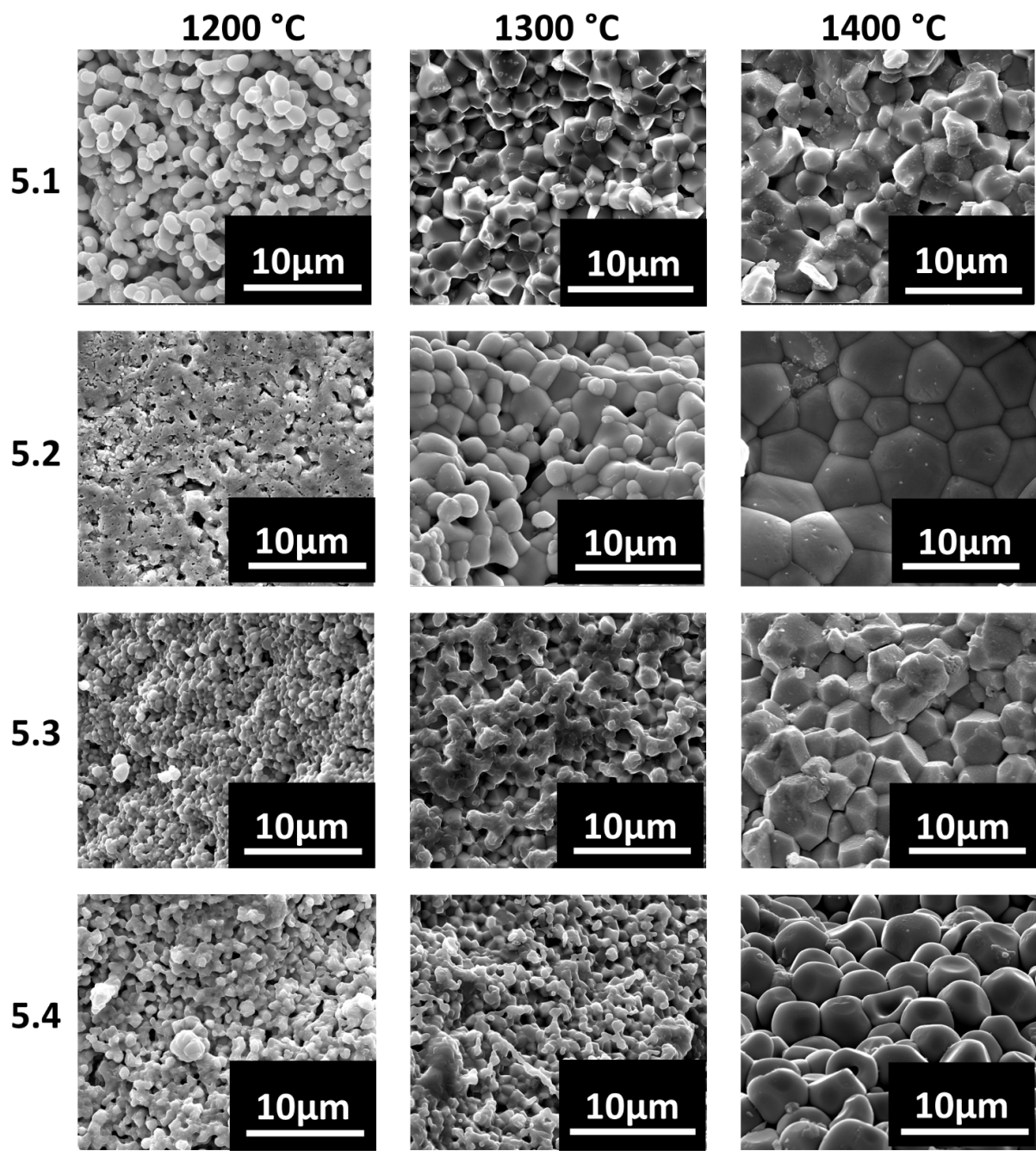
Figure 7-5 SEM images of polished and thermally etched pellets of system 5 MEPO
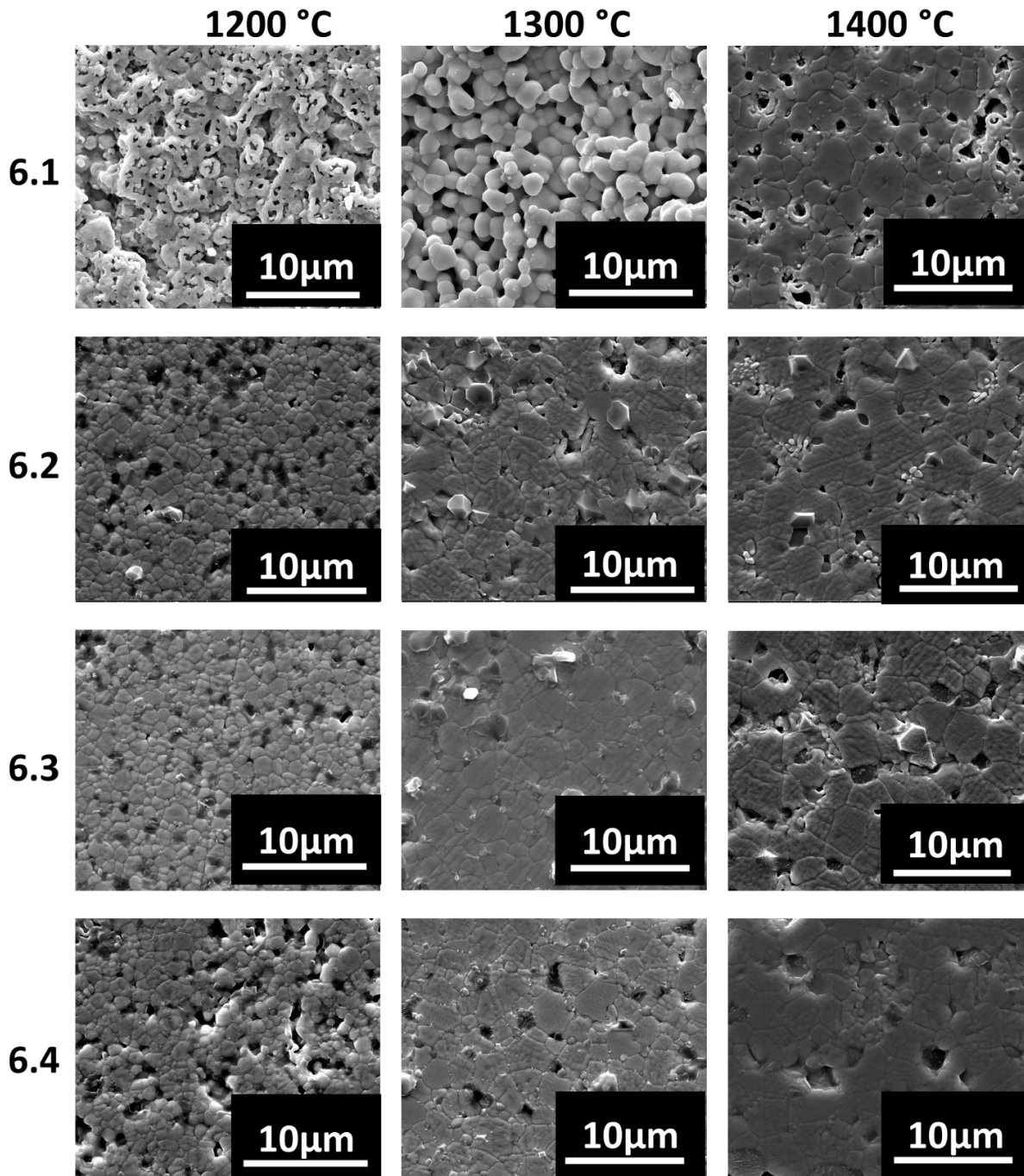
Figure 7-6 SEM images of polished and thermally etched pellets of system 6 MEPO
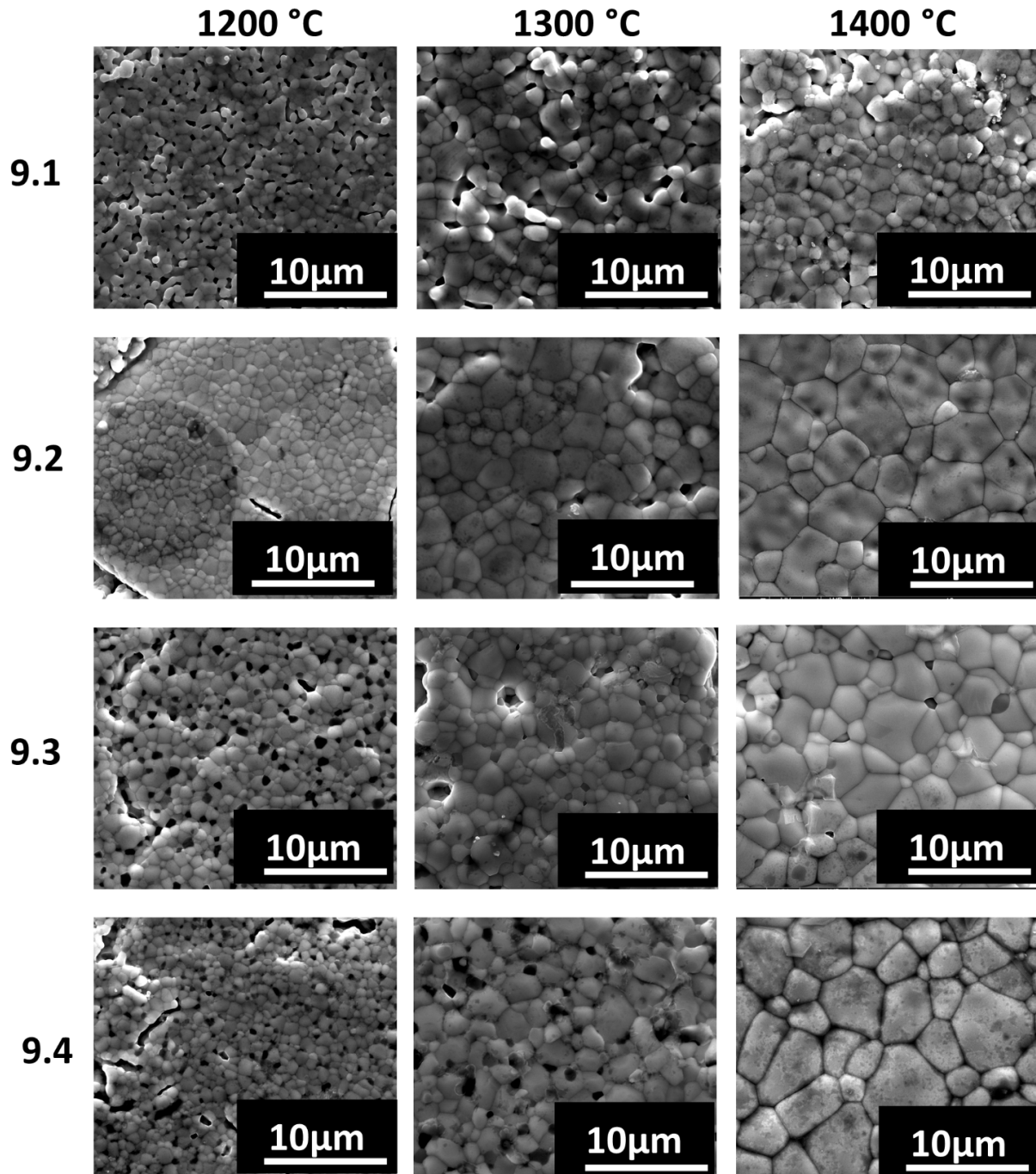
Figure 7-7 SEM images of polished and thermally etched pellets of system 9 MEPO

The undoped pellet of system 6 sintered at 1200°C displayed a clustered, grain-like

structure. As the sintering temperature increased to 1300°C and 1400°C, the grain shape

transitioned from curved to straight boundaries. This transition suggests that the sintering

71

mechanism changed from liquid phase to solid state, as the absence of liquid phase hinders grain rearrangement. On the other hand, system 6 pellets with Ca (10-30 mol%) sintered at 1200°C showed rounded corners, a characteristic of transient liquid phase sintering. As the sintering temperature increased, the grain boundaries of calcium-doped pellets became similar to those of undoped pellets at 1400°C, showing straight boundaries and a coarsened grain structure. SEM images of Ca-doped pellets sintered between 1200-1400°C also support this change in sintering mechanism from liquid phase to partial liquid phase, as the grain shape changed from round to straight. Additionally, pellets of system 6 sintered at 1400°C recorded the largest grain size of 1.94~2.4μm.

SEM images of the pellets of system 9 sintered at different temperatures showed varying grain structures. The images of pellets sintered at 1400°C showed larger average grain size compared to those sintered at 1200 and 1300°C, with the largest grain size of 4.14um obtained for the 30 mol% Ca pellet sintered at 1400°C. The smallest grain size of 0.98um was obtained for the 30 mol% Ca pellet sintered at 1200°C. The SEM images showed a well-rounded grain boundary, indicating that the pellets underwent liquid phase sintering. The amount of liquid phase increased with the addition of Ca, as evident from the sharp increase in sintered densities of Ca 20 and 30 mol% pellets compared to Ca-free and Ca 10 mol% pellets. This increase in liquid phase led to an enhancement of the sintered density.

Thus, the addition of Ca in systems 5, 6, and 9 increases the amount of liquid phase necessary for sintering. A Ca addition of 10 mol% in system 5 was sufficient to fully densify the pellet, while lower amounts of Ca, such as 10 and 20 mol%, were insufficient to fully densify the pellets of systems 6 and 9. To fully densify the pellets of systems 6 and 9, at least 30 mol% of Ca is required.

Table 7-2 Relative sintered densities of systems 5, 6, and 9 pellets sintered at 1200, 1300, and 1400°C in atmospheric air for 2 hours

MEPO samples	Sintering temperatures		
	1200°C	1300°C	1400°C
5.1	90	91	97
5.2	92	98	99
5.3	94	98	98
5.4	94	97	95
6.1	65	62	63
6.2	69	69	67
6.3	70	70	71
6.4	97	98	99
9.1	68	68	69
9.2	77	68	72
9.3	75	71	74
9.4	96	97	99

Table 7-3 Average grain sizes of systems 5, 6, and 9 pellets sintered at 1200, 1300, and 1400°C in atmospheric air for 2 hours

MEPO samples	Average grain size (μm)		
	1200°C	1300°C	1400°C
5.1	1.2	1.52	2.78
5.2	1.43	1.2	2.42
5.3	1.23	0.71	2.06
5.4	0.96	0.73	2.48
6.1	1.12	1.23	1.94
6.2	0.96	2.1	2.17
6.3	0.98	2.16	2.4
6.4	1.15	1.78	2.2
9.1	1.18	1.8	1.8
9.2	1.137	2.24	3.32
9.3	0.99	1.7	2.65
9.4	0.98	1.83	4.14

7.4 EDS maps

EDS mapping was performed on the pellets sintered at 1400°C; their images are given in Figure 7-8 and their elemental compositions are provided in Table 7-4. The results show the presence and distribution of La, Ca, Cr, Co, Fe, and Ni. Based on the EDS maps, it can be inferred that the substitution of three TM ions on the B-site with La and Ca is complete.
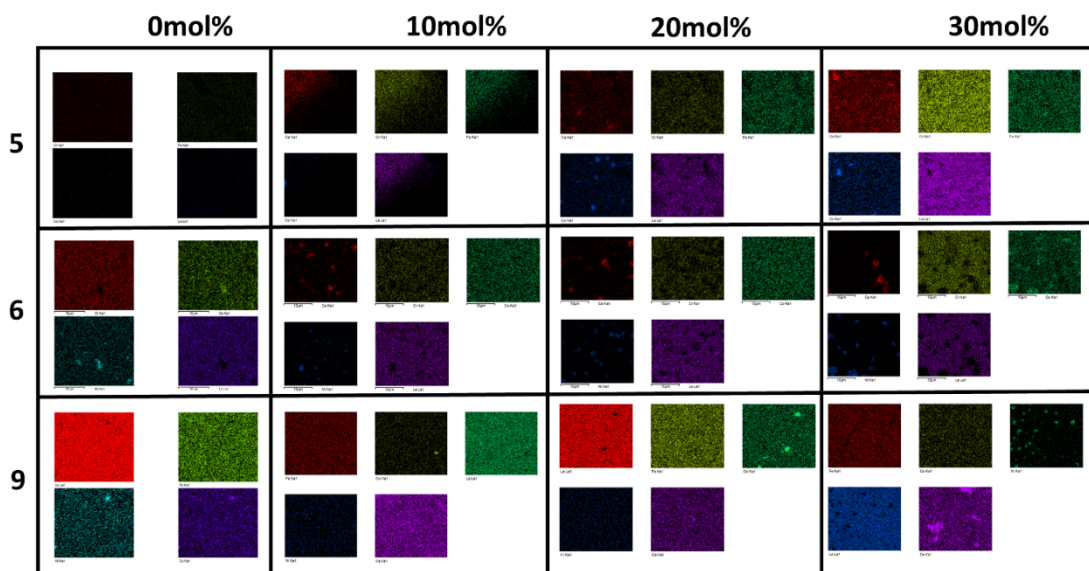
Figure 7-8 EDS elemental analysis of MEPO systems 5, 6, and 9 sintered at 1400°C

Table 7-4 Elemental compositions of MEPO systems 5, 6, and 9 sintered at 1400°C

MEPO samples	La (wt%)	Ca (wt%)	Cr (wt%)	Co (wt%)	Fe (wt%)	Ni (wt%)
5.1	47.62	-	15.95	18.99	17.43	-
5.2	37.37	7.08	19.24	16.74	19.57	-
5.3	42.56	7.84	15.91	16.19	17.5	-
5.4	39.94	11.92	18.52	9.69	19.93	-
6.1	49.52	-	16.4	17.6	-	16.49
6.2	41.64	9.01	15.37	17.31	-	16.66
6.3	39.29	9.44	15.71	18.07	-	17.49
6.4	36.61	10.55	16.41	20.55	-	15.69
9.1	56.24	-	-	17.19	15.92	10.66
9.2	45.16	5.94	-	14.77	17.61	16.52
9.3	39.13	9.15	-	17.54	18.36	15.81
9.4	37.01	14.76	-	14.77	15.23	15.36

7.5 Temperature dependence electrical conductivity

Figure 7-9 illustrate the electrical conductivities for MEPO systems 5, 6, and 9 in the range of 300-900°C. The linear nature of the conductivity graphs indicates that the electrical conductivity of these systems is driven by small polarons hopping through B-site TM^{+3} ions. Activation energies of the samples were obtained by fitting the small polaron equation 10 to the data shown in Figure 7-10 [106, 107]. The calculated activation energies and electrical conductivity values at 800°C are provided in Table 7-5. The slope of curves decreases with incremental substitution of Ca. This reduces the activation energies.
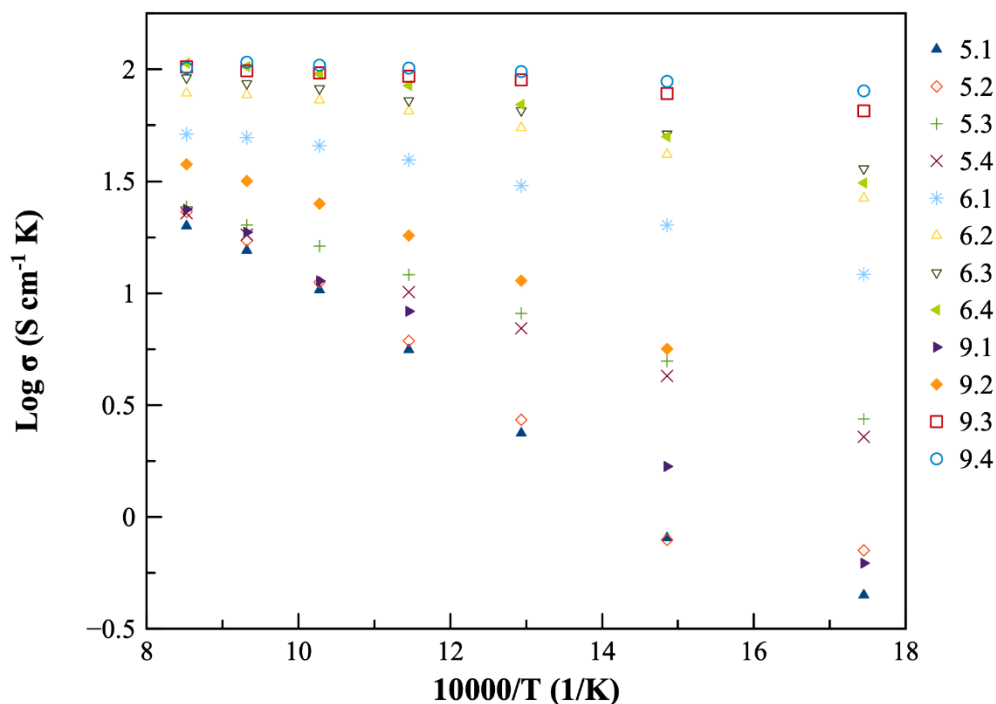
Figure 7-9 Electrical conductivity graphs of MEPO systems 5, 6, and 9 at temperatures 300-900°C in atmospheric air
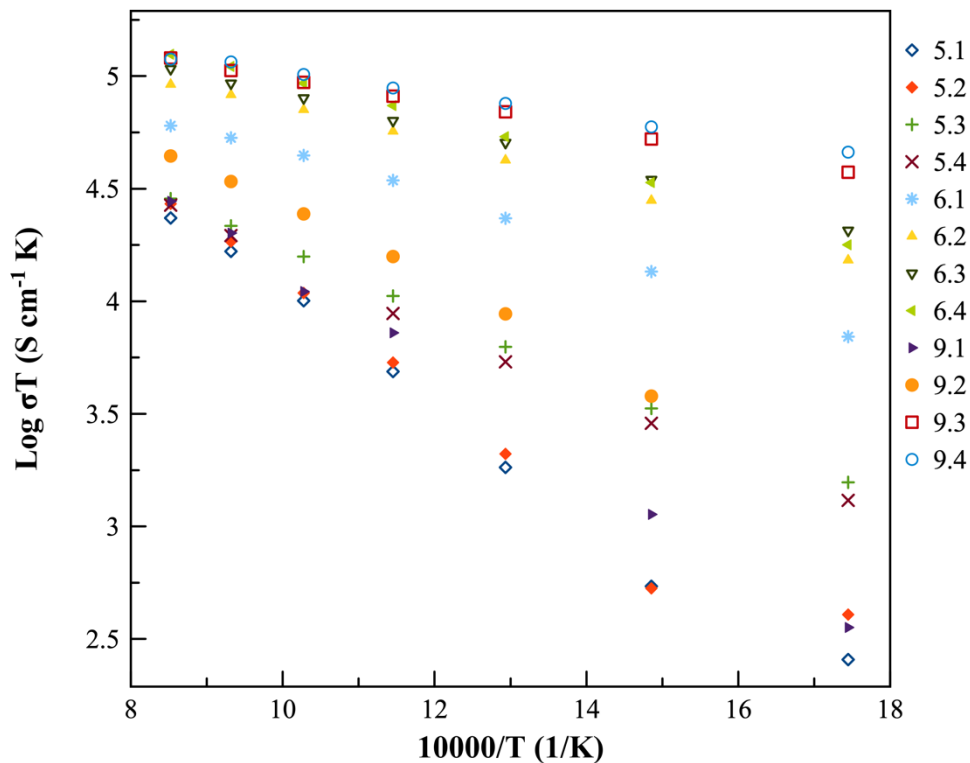
Figure 7-10 Arrhenius graphs of (Log σT vs. Inverse temperature) of MEPO systems 5, 6, and 9 at temperatures 300-900°C in atmospheric air

In the current study, most of the samples exhibited thermally activated behavior typical of a semiconductor in the temperature range of 300-900°C. However, two samples, 6.4 and 9.4 (with 30 mol% Ca doping), showed a gradual transition from semiconductor behavior at temperatures below 800°C to a non-activated, metallic-like behavior at temperatures above 800°C (see Figure 7-9). This behavior is similar to that observed in the parent members (LaCoO$_3$ and LaNiO$_3$) of systems 6 and 9, as reported in the previous study [45, 88, 108–110]. Notably, these samples also had the highest electrical conductivity values at 800°C. The transition from semiconductor to metallic-like behavior in 6.4 and 9.4 is attributed to the narrowing of the band gap between the conduction and valence bands of the transition metals (from Cr to Ni) [103].

The undoped samples of systems 5, 6, and 9 had low electrical conductivity values at 800°C (15, 50, and 19 S/cm respectively). The addition of Ca was found to increase the

conductivity of all three systems. In particular, system 5 saw a slight increase in conductivity

with incremental additions of Ca. One possible reason is that Fe inhibits the formation of

Co^{+3}/Co^{+4} and Cr^{+3}/Cr^{+4} couples, reducing the number of hopping sites and limiting the electrical

conductivity [104]. Conversely, in system 9, the charge disproportionation of Fe^{+3}/Fe^{+5} caused by

calcium doping is thought to improve conductivity. This suggests that the different combinations

of TM ions with Fe can have a significant impact on conductivity properties. Additionally, in

system 6, incremental addition of Ca increased the conductivity due to the increase in B-site

TM^{+3}/TM^{+4} pairs, which facilitated the polaron hopping and improved the conductivity [104].
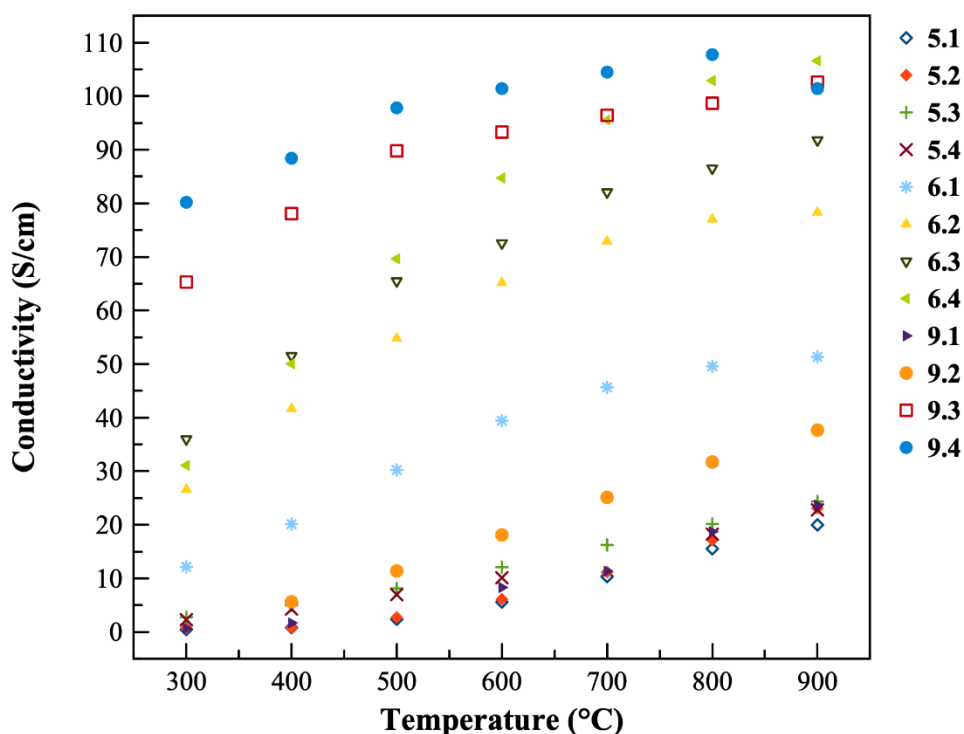
Figure 7-11 Apparent electrical conductivity vs. temperature of MEPO systems 5, 6, and 9 at temperatures 300-900°C in atmospheric air

The addition of divalent Ca in systems 5, 6 and 9 reduces the activation energies, as seen

in Table 7-5. The highest activation energies were found in the Ca-free samples of systems 5, 6,

and 9, while the lowest activation energies were observed in the samples with the highest Ca

doping (30 mol%). The doping of Ca also improves the electrical conductivities of systems 5, 6 and 9.

Table 7-5 Apparent electrical conductivity and activation energies of MEPO systems 5, 6, and 9 at 800°C in atmospheric air

MEPO samples	Electrical Conductivity (S/cm)	Activation energies (eV)
5.1	15	2.01
5.2	17	1.9
5.3	20	1.3
5.4	22	1.3
6.1	50	0.93
6.2	77	0.77
6.3	87	0.77
6.4	103	0.8
9.1	19	1.8
9.2	32	1.13
9.3	99	0.47
9.4	108	0.42

7.6 Conclusions

The XRD patterns of system 5 were indexed as an orthorhombic perovskite phase, while systems 6 and 9 were rhombohedral at lower Ca concentrations and transitioned to an orthorhombic as the Ca level increased. This transition was attributed to the incremental substitution of Ca in the A-site, which reduced the weighted average of A-site ionic radii and changed the cell symmetry from rhombohedral to orthorhombic. The lattice constants, unit cell

volumes, and pseudo lattice constants of the MEPO systems were also impacted by the addition of Ca. Overall, the results of this study demonstrate that the addition of Ca in fractional amounts can change the crystal structure and impact the structural parameters of MEPO systems.

The electrical conductivities of MEPO systems 5, 6, and 9 were found to be driven by small polaron hopping through B-site TM^{+3} ions, as indicated by the linear nature of the conductivity graphs. The addition of Ca was found to increase the conductivity of all three systems and reduce the activation energies. Two samples, 6.4 and 9.4, showed a transition from semiconductor behavior below 800°C to a non-activated, metallic-like behavior at temperatures above 800°C, which was attributed to the narrowing of the band gap between the conduction and valence bands of the transition metals. The different combinations of TM ions with Fe were found to have a significant impact on conductivity properties.

The study of sintered density revealed that the overall densities of pellets from systems 5, 6, and 9 at all temperatures were in the order of 5 > 9 > 6. The density of systems 5 and 9 increased with increasing temperature and Ca doping, but this pattern was not observed in system 6. The minimum amount of calcium needed to densify the pellets from system 5 was 10 mol%, while for systems 6 and 9, the least amount required was 30 mol%. All SEM images show microstructure formation. The average grain size of the undoped pellets of all three systems showed an increasing trend with temperature. A similar trend was observed for systems 6 and 9 with varying Ca levels. The SEM study of systems 5, 6, and 9 has shown that doping of Ca improves sinterability by forming low-temperature melting phases with B-site dopants that melt with rising temperatures, creating a transient liquid phase that densifies the pellets and evaporates at high temperature. The addition of a small amount of Ca is sufficient to enhance the sinterability of the pellets, but with increasing levels of Ca addition, the sintered densities

decreased slightly. Additionally, the study has shown that the Ca presence and sintering temperatures played an essential role in the sintered densities and grain growth. The data on sintering density and grain size suggest that the pellets were sintered in a transient liquid phase.

CHAPTER 8

STUDYING THE EFFECT OF Co AND Ni SUBSTITUTION IN

$La_{1-x}Ca_x(Fe_{1/3}Mn_{1/3}Ni_{1/3})O_3$, and $La_{1-x}Ca_x(Co_{1/3}Fe_{1/3}Mn_{1/3})O_3$ MEPO SYSTEM

8.1 Introduction

This chapter discusses the effect of Co and Ni in $La_{1-x}Ca_x(Fe_{1/3}Mn_{1/3}Ni_{1/3})O_3$ (system 7) and $La_{1-x}Ca_x(Co_{1/3}Fe_{1/3}Mn_{1/3})O_3$ (system 8), and Ca substitution in the A-site regarding crystal structure, sinterability, and electrical conductivity. XRD results revealed that the intensity of reflections 2θ (30-35°) shifted with increasing Ca substitution in the A-site. The unit cell volume, lattice constant, and crystallite values decreased linearly in both systems. Energy-dispersive X-ray spectroscopy confirmed the presence of various elements including La, Ca, Co, Fe, Mn, and Ni. The average grain size of system 7 increased with increasing sintering temperature and decreased with Ca doping level. However, the grain size of system 8 showed a wide variation and increased with sintering temperatures due to oxygen vacancy formation by Ca doping. The sinterability of system 7 improved with partial substitution of Ca, while system 8 sintered better after sintering at 1300°C. The electrical conductivity in both systems was due to the small polaron hopping mechanism, with system 7 showing increased conductivity with Ca substitution until 20 mol% and then reducing for the sample with 30 mol% Ca. On the other hand, the electrical conductivity of system 8 improved with incremental addition of Ca. The activation energies for system 7 reduced with Ca substitution, while for system 8 they increased with Ca substitution, attributed to the presence of Co in system 8.

8.2 XRD results

The XRD data of the synthesized powders of the systems show that the powders mostly crystallized into a single-phase orthorhombic perovskite structure (space group: 62, Pbnm)

after being calcined at 950°C for 9 hours, with the exception of sample 7.4. Sample of 7.4 showed a secondary phase of NiMnO (cubic). The incompleteness of the crystallization process in powder sample 7.4 is likely due to the low calcination temperature and time. However, after being calcined at 1050°C for 10 hours, the crystallization process was completed, and single-phase powders were produced. Their XRD results are shown in Figure 8-1 and Figure 8-2. From the XRD graphs, it is evident that the peak present between the $2\theta=30-35°$, shift to either lower or higher angles with increasing Ca substitution on the A-site (as seen in Figure 8-3). This peak shift depends on the degree of change in the structural parameters caused by doping with Ca on the A-site. This type of peak shift is typical in doped perovskite oxide systems [80].

The structural parameters such as lattice constants (a, b, c), unit cell volume, and pseudo cubic lattice constant were calculated using the significant reflections of (002), (112), (202), (004), (024), (025), and (116) (see Table 8-1). The unit cell volumes, calculated using the formula v=a*b*c, were found to be linearly reducing in system 8, while this trend was not observed in system 7. In system 7, adding Ca in 10 and 30 mol% (samples 7.2 and 7.4) resulted in an increase in the unit cell volume compared to the undoped (sample 7.1) and 20 mol% Ca (sample 7.3) samples. Notably, the highest reflection of the samples with 10 and 30 mol% Ca (samples 7.2 and 7.4) moved to lower 2θ angles, which increased the cell volume. In contrast, for samples 7.1, 7.3, and system 8 samples, the highest reflection moved to higher angles, reducing the cell volume due to the minor addition of Ca in the La site. The addition of 30 mol% Ca had a different impact on the unit cell volume in these samples, which may be due to the different combinations of B-site TM ions. The unit cell volume of 7.4 was reduced by less than 0.5% from its undoped powder, while the cell volume of 8.4 was reduced by 5% from its

undoped sample. The unit cell volume was found to be higher for system 8 samples than system 7 samples, which may be due to the substitution of Co for Ni on the B-site of system 8.
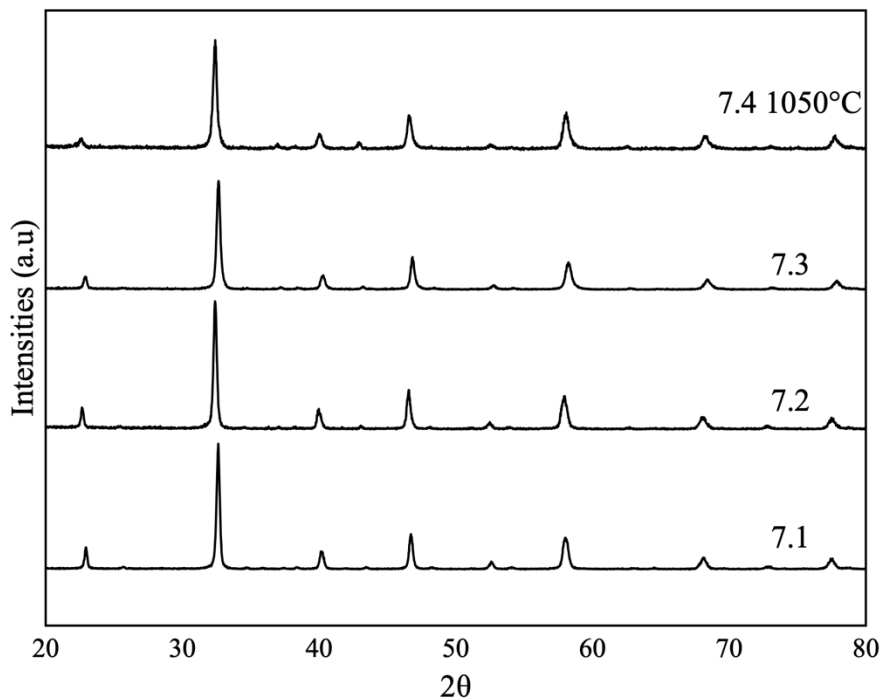
Figure 8-1 XRD spectra of system 7 samples 7.1-7.3 calcined at 950°C for 9 hours and 7.4 calcined at 1050°C for 10 hours
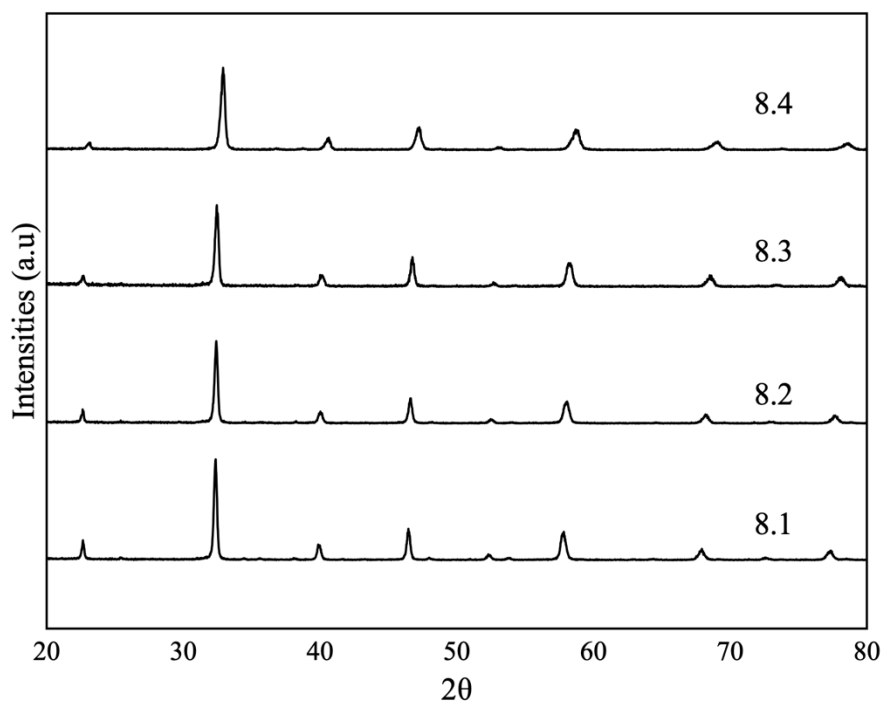
Figure 8-2 XRD spectra of system 8 calcined at 950°C for 9 hours
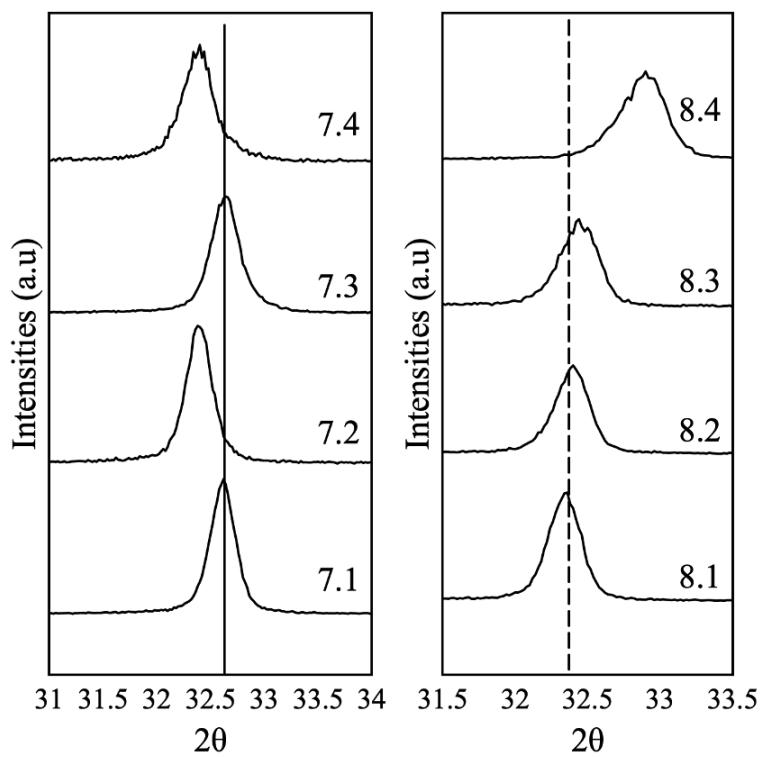
Figure 8-3 Magnified view of the highest peak of systems 7 and 8

8.2.1 Pseudo cubic lattice constant

The pseudo cubic lattice constant was found using the equation 9 and their results are shown in Table 8-1. The calculated pseudo cubic lattice constants of system 7 follow a similar trend as their unit cell volume. While the pseudo cubic lattice constant for system 8 decreases linearly.

8.2.2 Crystallite size

The average crystallite size extracted using the Scherrer equation is given in Table 8-1. The average crystalline sizes of the two systems reduced in a linear fashion with the addition of Ca. The largest size was for the sample 8.1 at 26nm, and the least was for the sample 8.4 at 18nm.

Table 8-1 Unit cell parameters, unit cell volume, crystallite size, and pseudo cubic lattice of MEPO systems 7 and 8

Compositions	Space group	a (Å)	b (Å)	c (Å)	Unit cell volume (Å^3)	Crystallite size (nm)	Pseudo cubic lattice a$_0$ (Å)
7.1	Pbnm	5.47	5.64	7.79	240.289	24.1296	3.91644
7.2	Pbnm	5.58	5.65	7.67	241.839	22.5493	3.92484
7.3	Pbnm	5.47	5.59	7.76	237.393	21.5048	3.90064
7.4	Pbnm	5.49	5.61	7.77	239.305	19.7989	3.91108
8.1	Pbnm	5.52	5.7	7.8	245.329	26.1611	3.94363
8.2	Pbnm	5.51	5.64	7.77	241.732	25.3106	3.92426
8.3	Pbnm	5.51	5.63	7.75	240.37	23.0376	3.91688
8.4	Pbnm	5.43	5.58	7.7	233.232	18.0291	3.87772

8.3 Sintering studies

Figure 8-4 and Figure 8-5 show the SEM images of the polished thermally etched pellets of MEPO systems 7 and 8. The overall grain size of the pellets of system 7 increased with an increase in sintering temperatures and decreased with Ca doping levels at all sintering temperatures, as shown in Table *8-3*. The largest grain size of 2.3μm was obtained for the pellet of 7.3 sintered at 1400°C, while the smallest grain size of 0.4μm was calculated for the pellet of 7.4 sintered at 1200°C.

The grain sizes of the pellets of system 8 (see Table *8-3*) did not follow a specific trend and varied widely. They were found to be increased with respect to sintering temperature. The average grain size of the pellets sintered at 1200°C had the lowest value. This increase in average grain size with varying temperature is due to the formation of oxygen vacancies by the dopant Ca [80]. The smallest and largest average grain sizes of 0.8 and 6.2μm were observed for pellet 8.4 sintered at 1200 and 1400°C, respectively, and this rapid growth is due to the high doping level of Ca that enhanced the grain growth. A similar behavior was observed for Ca-doped systems discussed in previous chapters.

Sintered relative densities of systems 7 and 8 are given in Table 8-2. Sample 7.2 (Ca 10 mol%) reached 99% TD at 1400°C, and an increase in Ca level for 7.3 helped reach the sintered density to 99% TD at 1300°C. Hence, the partial substitution of acceptor Ca in system 7 improved the sinterability by forming a sufficient liquid phase in the lower sintering temperature and densified the pellets.

	1200 °C	1300 °C	1400 °C
7.1			
7.2			
7.3			
7.4			
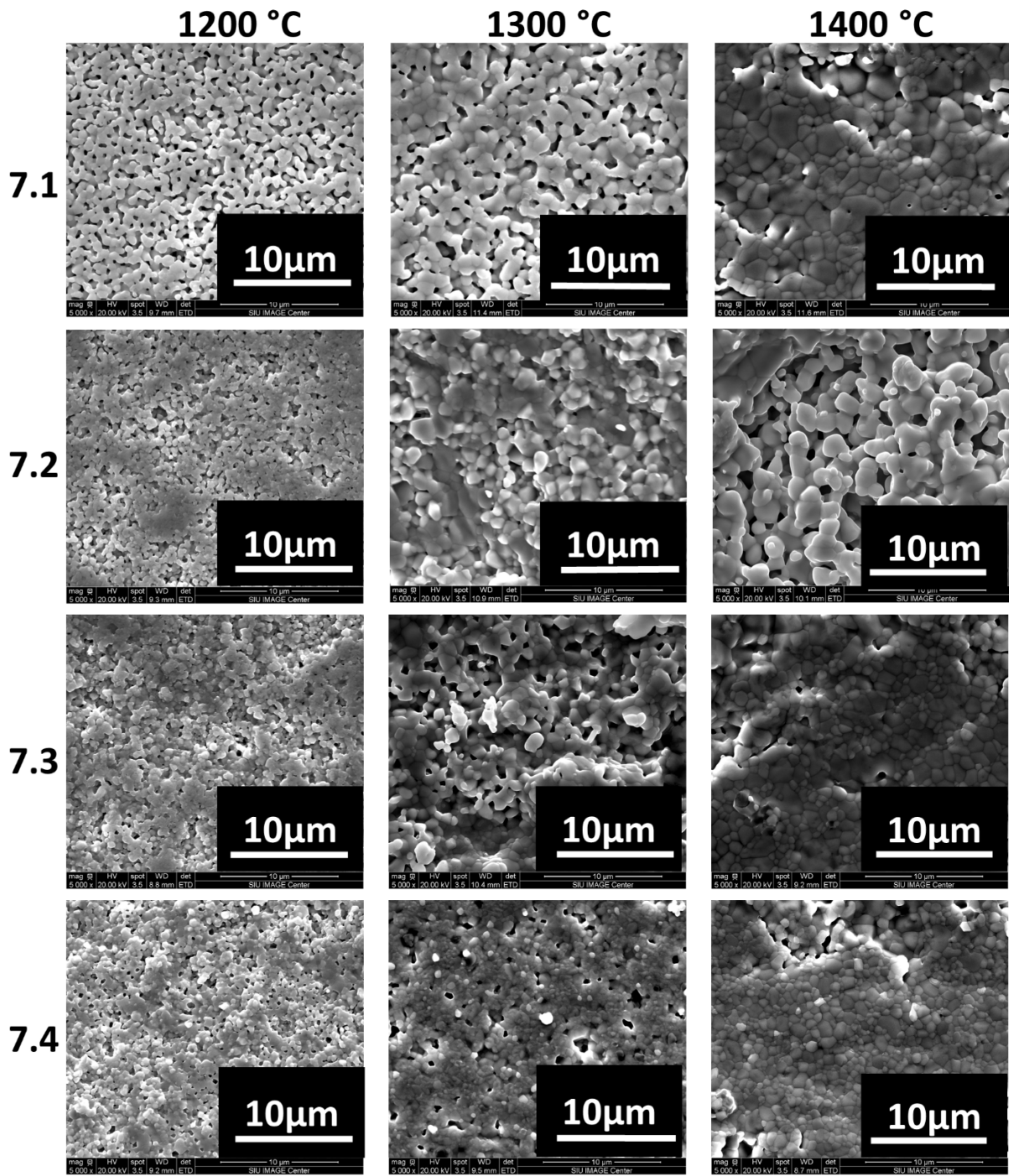
Figure 8-4 SEM images of polished and thermally etched pellets of MEPO systems 7
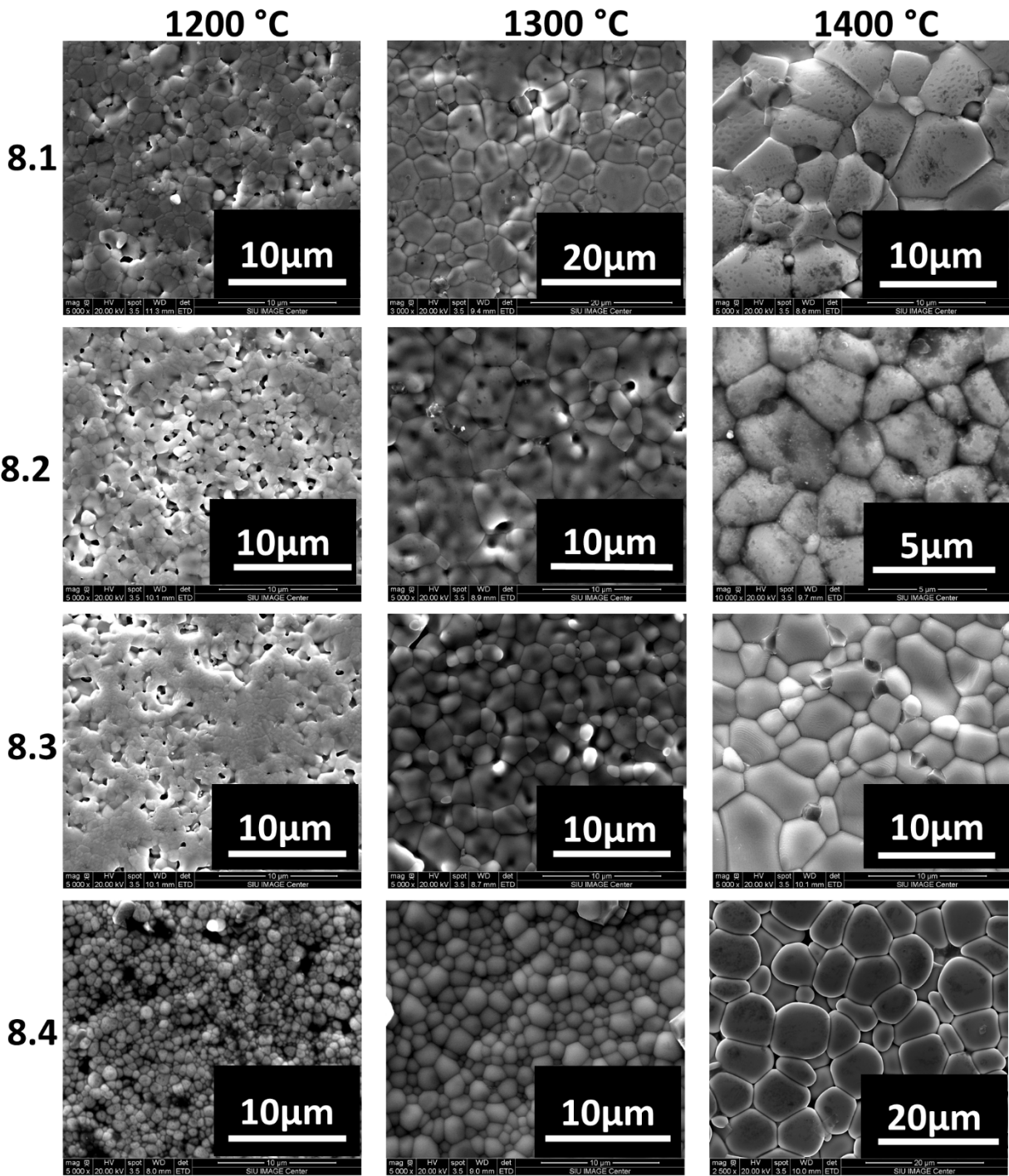
Figure 8-5 SEM images of polished and thermally etched pellets of MEPO system 8

The sintered densities of system 8 increased with the partial doping of Ca for the sintering temperatures of 1200 and 1300°C, while the samples sintered at 1400°C showed the opposite effect (see Table 8-2). Their sintered densities decreased with increased Ca levels, which could be due to the evaporation of the liquid phase due to the increase of temperature that reduced the sintering densities. SEM images of 8.4 agree with this interpretation as the grains showed visible gaps (see Figure 8-5). System 8 sintered better after sintering at 1300°C and reached 97-98% TD, compared to the samples sintered at 1400°C.

Table 8-2 Sintered densities of MEPO systems 7 and 8 sintered at 1200, 1300, and 1400°C in atmospheric air for 2 hours

MEPO samples	Sintered densities (%)		
	1200°C	1300°C	1400°C
7.1	69	84	97
7.2	87	93	99
7.3	92	99	99
7.4	94	99	99
8.1	90	97	98
8.2	91	97	99
8.3	91	97	97
8.4	96	98	93

Table 8-3 The average grain size of MEPO systems 7 and 8 sintered at 1200, 1300, and 1400°C in atmospheric air for 2 hours

MEPO samples	Average grain size (μm)		
	1200°C	1300°C	1400°C
7.1	0.61	0.96	1.75
7.2	0.5	1.03	1.7
7.3	0.5	0.9	2.3
7.4	0.4	0.9	1.7
8.1	1.06	3.4	3.45
8.2	1	3.8	2.3
8.3	1.86	2.45	3.6
8.4	0.8	1.73	6.2

8.4 EDS maps

The data in Figure 8-6 and Table 8-4 show the EDS spectra and elemental compositions of MEPO systems 7 and 8 sintered at 1400°C. The EDS spectra and elemental compositions confirm the presence of La, Ca, Co, Fe, Mn, and Ni. These results align well with the XRD results and confirm the phase purity of all compositions. Additionally, it can be seen that as the Ca substitution level increases, the La concentration decreases, indicating that Ca is replacing La.
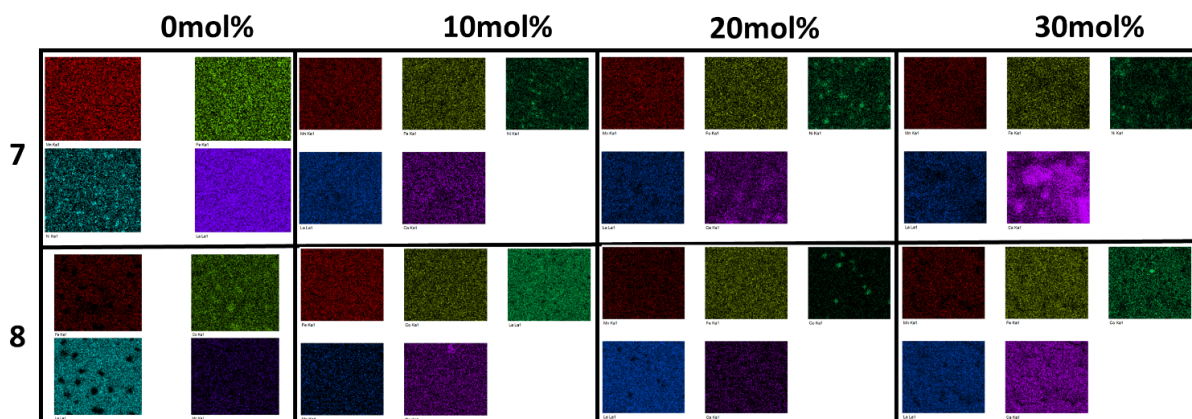
Figure 8-6 EDS elemental analysis of 7 MEPO systems 7 and 8, sintered at 1400℃

Table 8-4 Elemental compositions of MEPO systems 7 and 8 sintered at 1400℃

MEPO samples	La (wt%)	Ca (wt%)	Co (wt%)	Fe (wt%)	Mn (wt%)	Ni (wt%)
7.1	48.41	-	-	17.47	16.9	17.21
7.2	43.95	5.11	-	18.05	16.51	16.38
7.3	38.12	12.09	-	17.37	15.8	16.61
7.4	33.24	18.27	-	17.65	15.48	15.36
8.1	48.54	-	17.55	16.34	17.57	-
8.2	44.36	5.29	16.97	18.09	15.29	-
8.3	40.34	10.21	14.56	17.11	17.78	-
8.4	37.75	13.95	11.91	18.31	18.07	-

8.5 Temperature dependence electrical conductivity

Figure 8-7 gives the electrical conductivity plots of 7 MEPO systems 7 and 8 atmospheric within a temperature range of 300-900°C. The linearity of Arrhenius plots (shown in Figure 8-8) indicates that the electrical conductivity in systems 7 and 8 is due to small polarons hopping along the B-site ions. Equation 10 describes the small polaron conduction mechanism in systems 7 and 8.
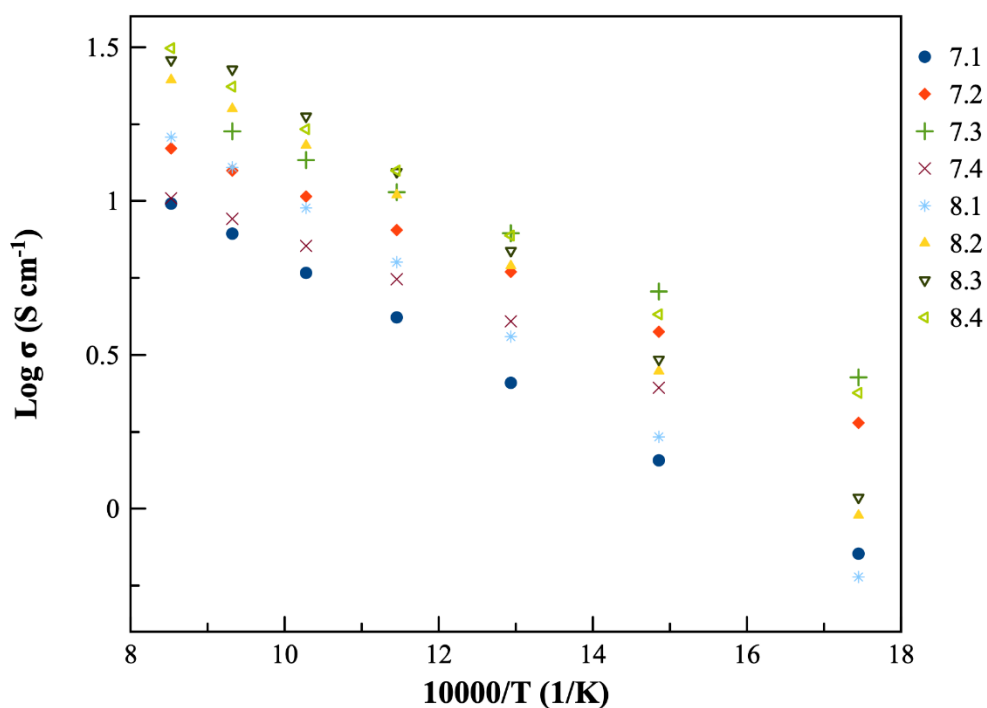
Figure 8-7 Electrical conductivity graphs of MEPO systems 7 and 8 measured in atmospheric air
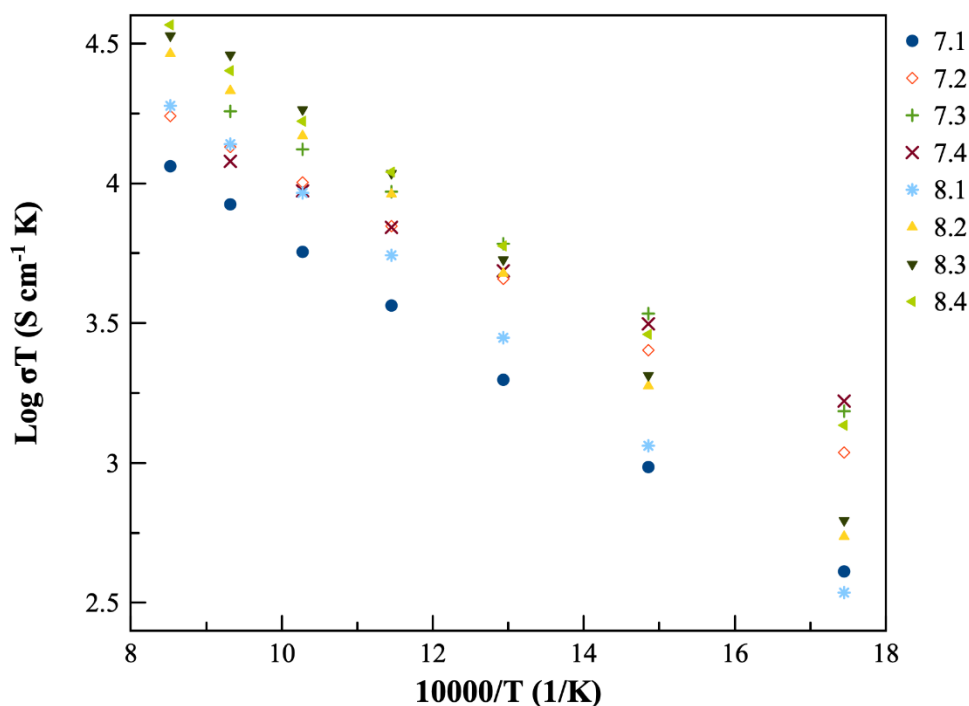
Figure 8-8 Arrhenius plots of MEPO systems 7 and 8 measured in atmospheric air

In system 7, the conductivity was observed to increase with the addition of Ca^{+2} on the A-site until it reached 20 mol% (17 S/cm for 7.3 sample). However, the conductivity then reduced for the sample with 30 mol% Ca^{+2} (11 S/cm for the 7.4 sample). This value is lower than the sample with 10 mol% of Ca^{+2} (13 S/cm for the 7.2 sample). The reduction in conductivity for the 7.4 sample can be associated to the trapping of charge carriers by chains of Fe^{+2}-Fe^{+4} and Mn^{+2}-Mn^{+4}, as previously observed in the parent members of system 7 ($LaMnO_3$ and $LaFeO_3$) by Tai [92]. The charge imbalance caused by the addition of divalent Ca in a tri-valent La site is balanced by either producing +4 valence states of B-site elements or oxygen ions. It is believed that the electrical conductivity increases when the electronic balance is maintained by forming the +4 valence states of B-site elements and decreases when oxygen ions are formed or increased. In this case, the addition of 10 and 20 mol% Ca^{+2} increased the conductivity by increasing the formation of +4 states of B-site elements that can be used for the mobility of the

charge carrier, resulting in improved conductivity. On the other hand, 30 mol% Ca formed

oxygen ions and inhibited the creation of +4 B-site elements, and Fe^{+2}-Fe^{+4} and Mn^{+2}-Mn^{+4} sites

(Fe and Mn traps) acted as traps and reduced the electrical conductivity [92].

For system 8, the electrical conductivity improved with the incremental addition of Ca^{+2}

on the A-site. The conductivity of high Ca^{+2} samples doubled that of the undoped samples (see

Figure 8-9 and Table 8-5). The substitution of Co in system 8 for Ni (used in system 7) increased

the electrical conductivity by controlling the formation of Fe and Mn traps.

The activation energies were calculated from the slope of the Arrhenius plots and are

presented in Table 8-5. The activation energies for system 7 reduced with the substitution of

Ca^{+2}, while for system 8 the activation energies followed an increasing trend with respect to the

substitution of Ca^{+2}. The activation energy values provide information about the mobility of a

charge carrier. The results show that the energy required for the charge carrier transportation in

system 7 is less than in system 8. This difference can also be attributed to the presence of Co^{+3} in
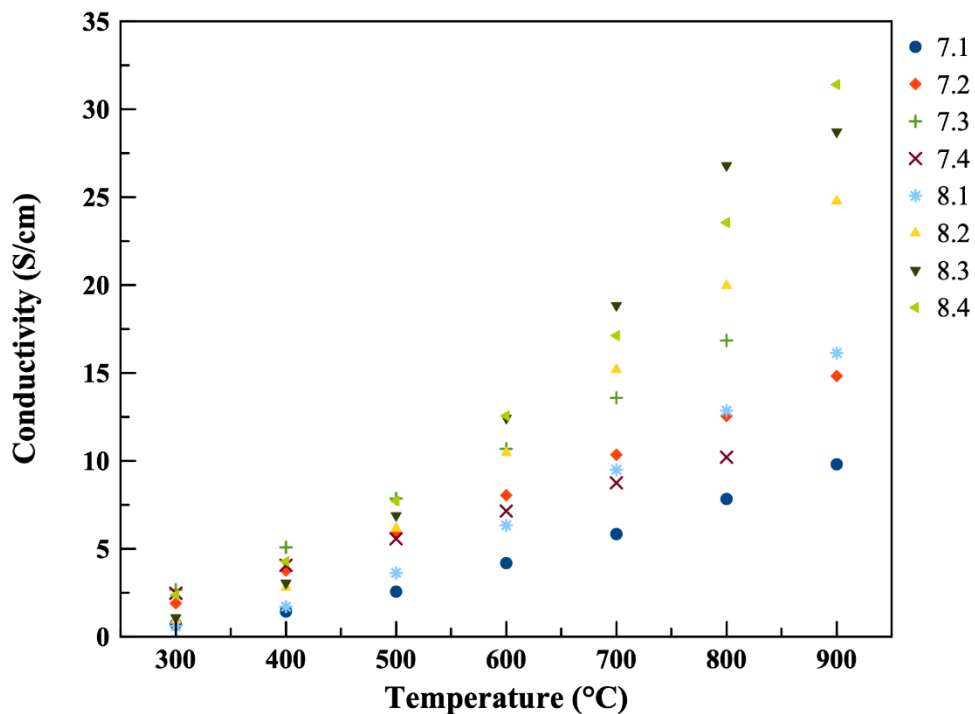
system 8.

Figure 8-9 Electrical conductivity vs. temperature of MEPO systems 7 and 8

Table 8-5 Electrical conductivity and activations energies of MEPO systems 7 and 8 at 800°C in atmospheric air

MEPO samples	Electrical conductivity at 800°C	Activation energies (eV)
7.1	8	1.41
7.2	13	1.15
7.3	17	1.12
7.4	11	1.15
8.1	12.9	1.68
8.2	20	1.69
8.3	26.8	1.76
8.4	31.4	1.73

8.6 Conclusions

The synthesized powders of systems 7 and 8 mainly crystallized into a single-phase perovskite structure after being calcined at 950°C for 9 hours. The XRD results show that the position of the reflections $2\theta=30\text{-}35°$ shift to lower or higher angles with increasing Ca substitution on the A-site. The unit cell volume, pseudo cubic lattice constant, and crystallite values of the samples were found to be linearly reducing in systems 7 and 8. EDS spectra confirmed the presence and homogeneous distribution of La, Ca, Co, Fe, Mn, and Ni in the respective samples.

The average grain size of the pellets of system 7 increased with an increase in sintering temperature and decreased with Ca doping level at all sintering temperatures. The grain sizes of the pellets belonging to system 8 varied widely and did not follow a specific trend. They were found to be increasing with respect to the sintering temperatures, which is due to the formation of oxygen vacancies by the dopant Ca. The sintered densities of system 8 samples increased with the partial doping of Ca for the sintering temperatures of 1200 and 1300°C, while the samples sintered at 1400°C showed the opposite effect. The sinterability of system 7 improved with the partial substitution of acceptor Ca, forming a sufficient liquid phase in the lower sintering temperature, and densifying the pellets. On the other hand, system 8 sintered better after sintering at 1300°C and reached 97-98% TD, compared to the samples sintered at 1400°C.

The electrical conductivity in systems 7 and 8 is due to the small polaron hopping mechanism. In system 7, the conductivity increased with the addition of Ca^{+2} on the A-site until it reached 20 mol%, but then reduced for the sample with 30 mol% Ca^{+2}. This reduction in conductivity is believed to be caused by the trapping of charge carriers by pairs of $Fe^{+2}\text{-}Fe^{+4}$ and $Mn^{+2}\text{-}Mn^{+4}$, as previously observed in the parent members of system 7. In system 8, the electrical

conductivity improved with the incremental addition of Ca^{+2} on the A-site. The substitution of Co in system 8 for Ni (system 7) increased the electrical conductivity by controlling the formation of Fe and Mn traps. The activation energies for system 7 reduced with the substitution of Ca^{+2}, while for system 8 the activation energies followed an increasing trend with respect to the substitution of Ca^{+2}. This difference can be attributed to the presence of Co^{+3} in system 8.

CHAPTER 9

DEVELOPMENT OF CALCIUM-DOPED La($Cr_{0.2}Co_{0.2}Fe_{0.2}Mn_{0.2}Ni_{0.2}$)$O_3$ HEPO SYSTEM

9.1 Introduction

This chapter introduces the novel La$_{1-x}$Ca$_x$($Cr_{0.2}Co_{0.2}Fe_{0.2}Mn_{0.2}Ni_{0.2}$)$O_3$ HEPO system and its synthesis process, crystal structure, and characterization. XRD, EDS, XPS, and electrical conductivity techniques were used to characterize and study the HEPO powders. This chapter also highlights the early results on sintering mechanism and electrical conductivity. This research is the first time that a divalent Ca was added to the A-site of La($Cr_{0.2}$ $Co_{0.2}$ $Fe_{0.2}$ $Mn_{0.2}$ $Ni_{0.2}$)O_3, which lowered sintering temperatures and improved electrical properties. Furthermore, for the first time a modified PPM is employed to produce nano sized HEPO powders.

9.2 XRD results

Figure 9-1 shows the XRD spectra of the synthesized La$_{1-x}$Ca$_x$ ($Cr_{0.2}$ $Co_{0.2}$ $Fe_{0.2}$ $Mn_{0.2}$ $Ni_{0.2}$)O_3 after calcination at 950°C for 9 hours. All the powders were well indexed based on orthorhombic perovskite structures of LaCrO$_3$ (Pnma, space group: 62, ID# 1526176) and La$_{0.8}$Ca$_{0.2}$CrO$_3$ (Pnma, space group: 62, ID# 1531964). The XRD results revealed that the powders were in a single phase. Lattice parameters were calculated from the peaks of (002), (112), (202), (004), (024), (025), and (116). The obtained results are presented in Table 9-1.
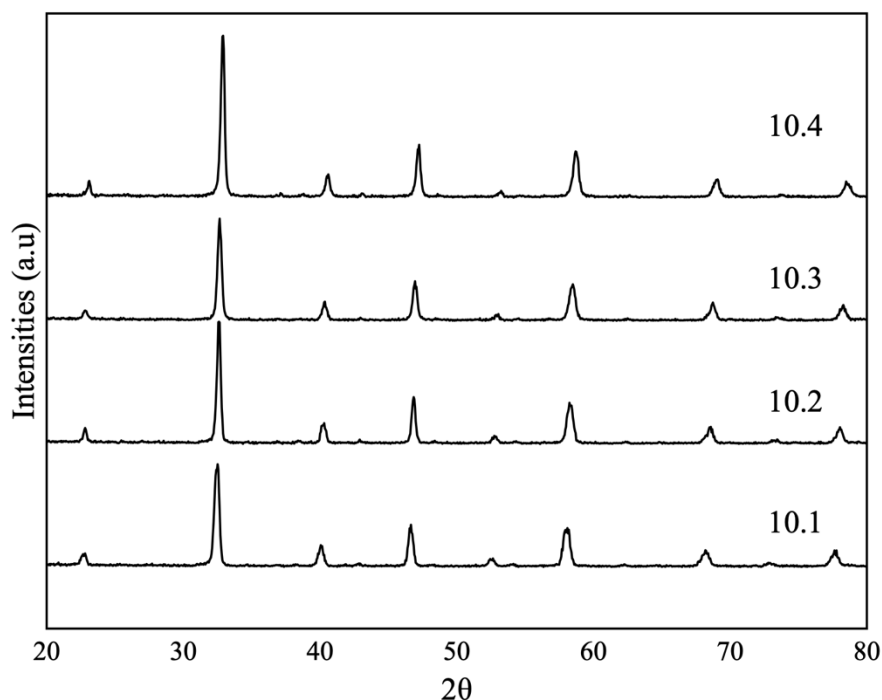
Figure 9-1 XRD patterns of system 10 calcined at 950°C

The partial addition of Ca^{+2} with La^{+3} does not affect the formation of a single-phase orthorhombic structure. To understand the influence of Ca with La, XRD spectra of $La_{1-x}Ca_x(Cr_{0.2} Co_{0.2} Fe_{0.2} Mn_{0.2} Ni_{0.2})O_3$ powders between the angles of 32-34 (2θ) were enhanced for comparison (see Figure 9-2). With low levels of Ca^{2+} doping (x=0.1), the peak slightly shifts toward a higher angle due to the smaller ionic radius of Ca (1.34 Å) compared to La (1.36 Å). As the Ca doping level increases (x=0.2, 0.3), the peak gradually shifts toward higher angles, indicating that the unit cell of $La_{1-x}Ca_x(Cr_{0.2} Co_{0.2} Fe_{0.2} Mn_{0.2} Ni_{0.2})O_3$ becomes smaller with higher Ca doping (see Table 9-1).
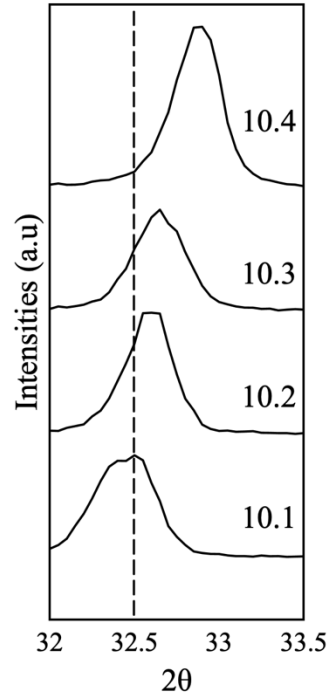
Figure 9-2 Magnified view of the major peak of system 10

Table 9-1 The lattice parameters (Å) and unit cell volume ($Å^3$) for different compositions of system 10 HEPO

Samples	a (Å)	b (Å)	c (Å)	Volume (Å)
10.1	5.5168	5.5401	7.8079	239
10.2	5.3646	5.4092	7.5851	220
10.3	5.3643	5.3897	7.5809	219
10.4	5.4273	5.401	7.6667	224

9.3 SEM

Figure 9-3 displays the SEM images of $La_{1-x}Ca_x (Cr_{0.2} Co_{0.2} Fe_{0.2} Mn_{0.2} Ni_{0.2})O_3$ pellets after they were sintered in air for 2 hours at 1400°C. The details of the sintered pellets, including their relative green density, relative sintered density, and average grain size, can be found in

Table 9-2. The green densities of the pellets were calculated using the pellets' mass and dimensions, while the sintered densities were determined using the Archimedes principle. The average grain size was determined using the line intercept method. Sintered densities of the pellets were increased through the substitution of calcium for lanthanum on the A-site. With an increase in sintering temperatures, the low melting point of calcium-rich phases melted and densified the pellets [97]. The SEM images imply that the pellets were sintered in a transient liquid phase, and the substitution of calcium also led to an increase in average grain size.
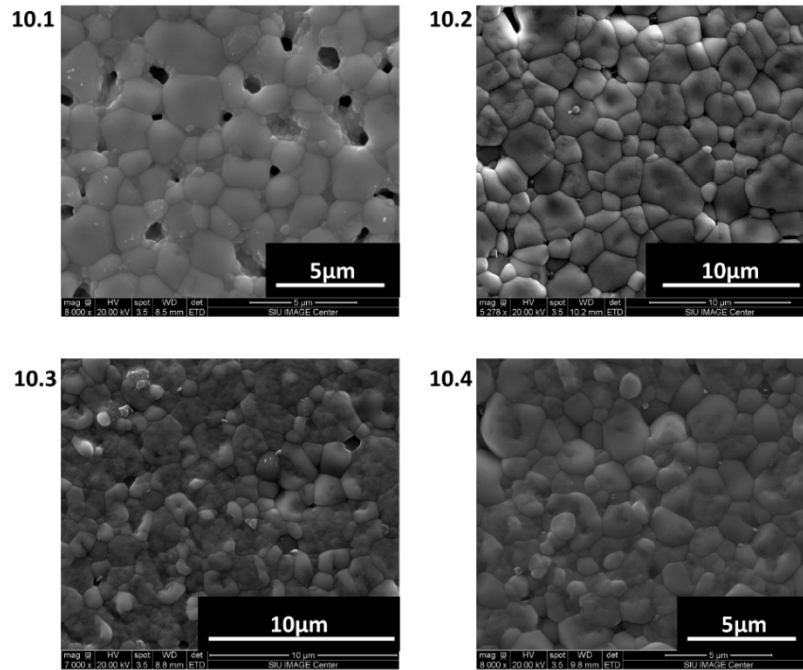
Figure 9-3 SEM images of system 10 HEPO sintered at 1400°C for 2 hours

Table 9-2 Relative sintered densities and average grain sizes

Sample	Relative Sintered density (%)	Average grain size (μm)
10.1	76	1.16
10.2	87	1.78
10.3	87	1.5
10.4	89	1.5

9.4 Temperature dependence electrical conductivity

The electrical conductivity and Arrhenius plots of the

$La_{1-x}Ca_x(Cr_{0.2}Co_{0.2}Fe_{0.2}Mn_{0.2}Ni_{0.2})O_3$ system are shown in Figure 9-4 and Figure 9-5,

respectively. Electrical conductivity was carried out in atmospheric air between the temperatures

of 300-900 °C. All four samples exhibited linear conductivity behavior, increasing as the

temperature rose. This behavior is attributed to the p-type small polaron hopping mechanism

along transition metal (B) - oxygen (O) - transition metal (B) bonds in perovskite oxides [105].
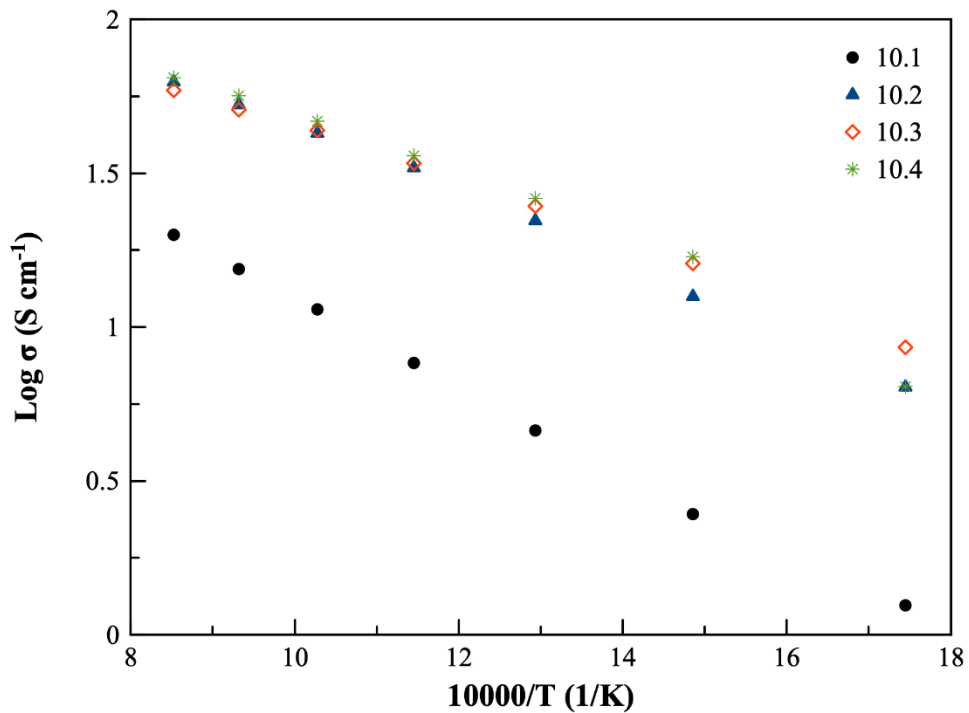
Figure 9-4 Electrical conductivity of system 10
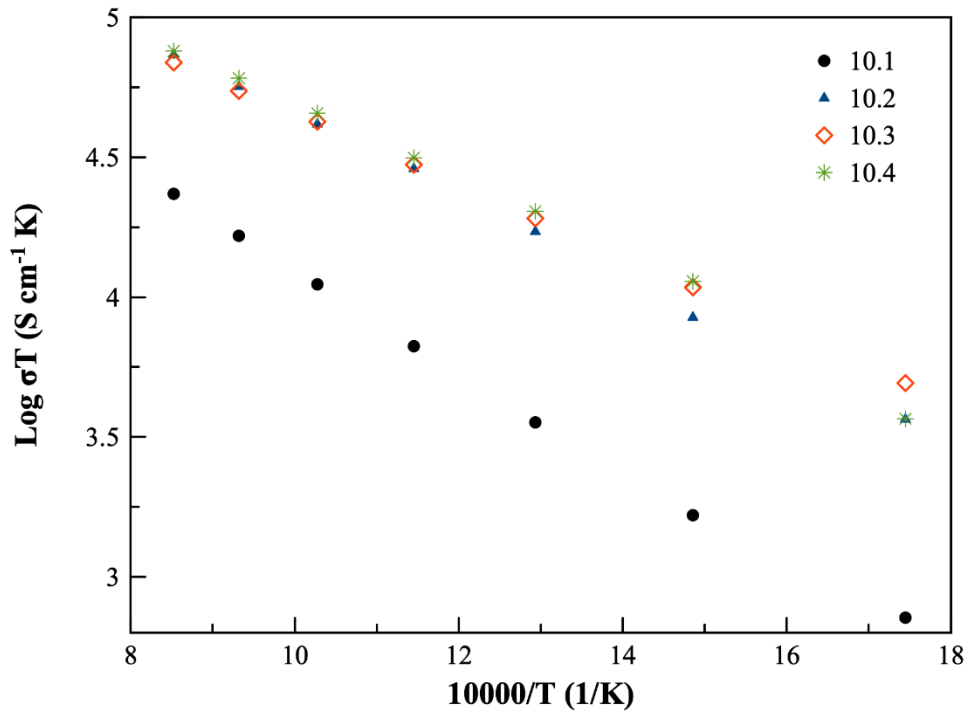
Figure 9-5 Arrhenius graphs of system 10

Table 9-3 shows the maximum electrical conductivity at 800°C along with associated activation energy. The electrical conductivity of the samples without Ca was 20 S/cm at 800°C. The addition of 10 mol% Ca with La improved the conductivity to 63 S/cm at 800°C in sample 10.2. Increasing the doping levels of Ca to 20 and 30 mol% slightly improved the conductivity in the samples of 10.3 and 10.4, to 64 and 65 S/cm at 800°C, respectively. The addition of Ca reduced the activation energies, and the activation energies of the Ca-doped samples were unchanged.

Table 9-3 Activation energies and electrical conductivity of the samples of HEPO system 10

Samples	Activation Energies (eV)	Electrical Conductivity at 800°C (S/cm)
10.1	1.5	20
10.2	1.3	63
10.3	1.3	64
10.4	1.4	65

The addition of Ca^{+2} in the present HEPO caused a charge disproportion, which was normalized by forming multivalent states (B^{+3} and B^{+4}) of B-site transition metals. When the charge imbalance is accommodated by increasing the B^{+3} and B^{+4} valence states, the electrical conductivity improves. B^{+3}/B^{+4} acts as the hopping sites for the charge carriers, causing conductivity to increase as Ca^{+2} doping creates more hopping sites. The highest conductivity is expected when the ratio of these couples is 1:1. This means that the electrical conductivity in the current perovskite oxides improves due to the formation of multiple valence states of the B-site cation along the B-O-B bonds. Equation 10 shows the electronic conduction of charge carriers along the B-O-B bonds [32].

$$B^{n+} - O^{-2} - B^{n+1} \rightarrow B^{n+1} - O^{-1} - B^{n+1} \rightarrow B^{n+1} - O^{-2} - B^{n+} \tag{11}$$
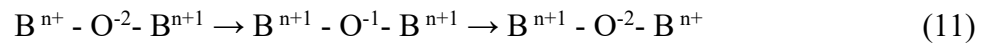
9.5 X-ray Photoelectron Spectroscopy of 10.4 HEPO powder

X-ray photoelectron spectroscopy (XPS) was used to characterize the chemical states of the transition metals present in the powder samples of $La_{0.7}Ca_{0.3}(Cr_{0.2}Co_{0.2}Fe_{0.2}Mn_{0.2}Ni_{0.2})O_3$ at room temperature. XPS is a highly sensitive device, making it an ideal choice for this analysis.

The survey spectrum of the sample with calcium concentration of 30% (Figure 9-6) showed the presence of La, Ca, Cr, Co, Fe, Mn, Ni, and O. The XPS fine scan of Cr 2p spectra given in Figure 9-7a, indicated the presence of peaks of Cr 2p1/2 and Cr 2p3/2 peaks at around

586 and 576eV, respectively. XPS data for Cr 2p was deconvoluted by considering the presence

of Cr, Cr^{+3}, and Cr-Oxide peaks. The Cr^{+3} peaks were present at 586.5 and 577.47eV, while the

peaks at 577.01eV were from Cr-Oxide, and the peaks at 583.9 and 574.5eV belonged to Cr.
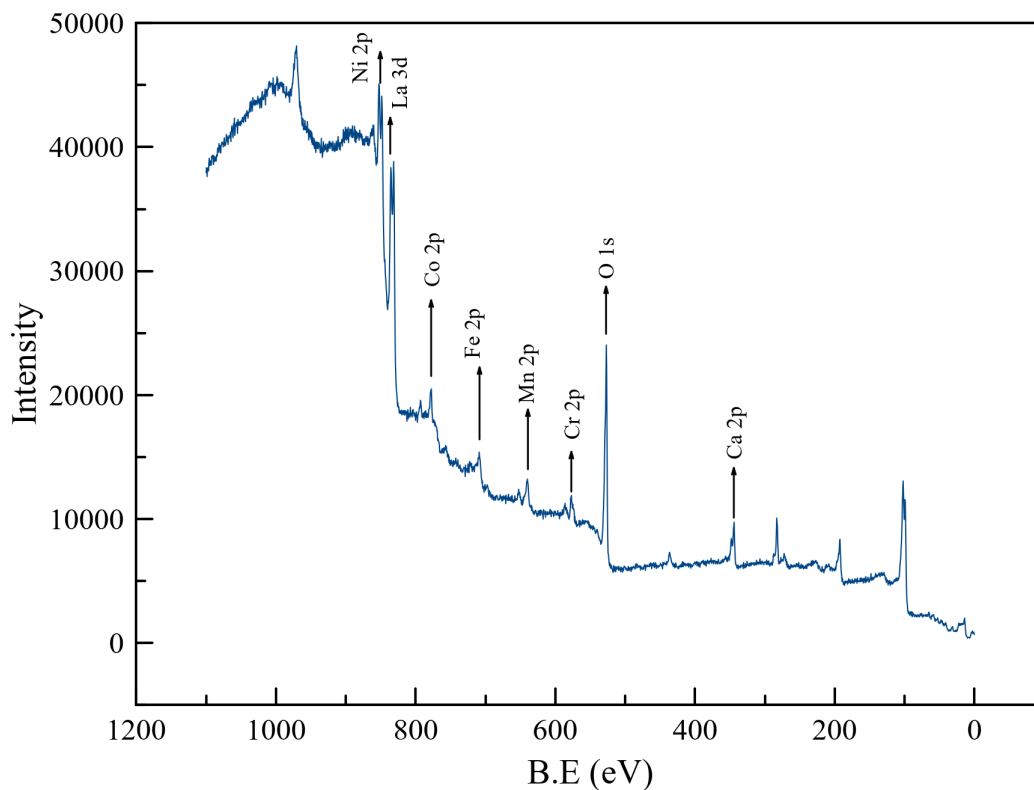
Figure 9-6 Survey spectrum of 10.4 HEPO powder
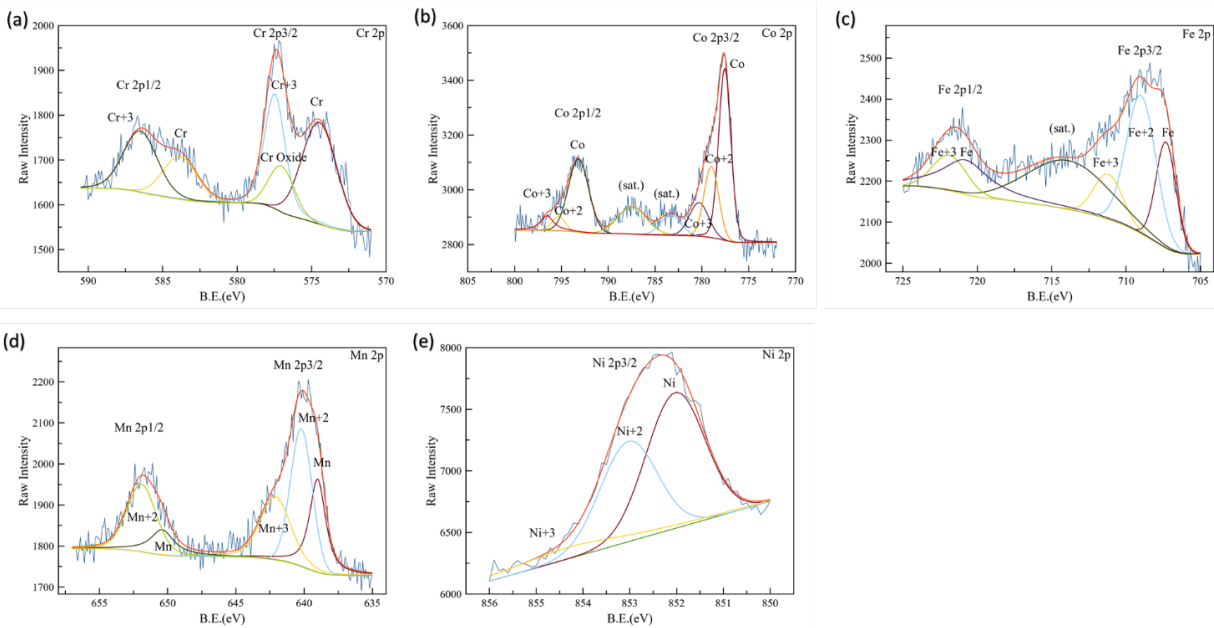
Figure 9-7 Fine scanning of transition metals in 10.4 HEPO powder

As shown in Figure 9-7b, Mn 2p1/2 and Mn 2p3/2 peaks are present at 652.5 and 640eV. Valence states of Mn^{+2} and Mn^{+3} peaks are obtained from deconvoluted peaks at 652, 640eV for Mn^{+2}, and 642eV for Mn^{+3}.

Figure 9-7c details the deconvoluted peaks of Co 2p spectra. The peaks of Co 2p1/2 and Co 2p3/2 are located at 795 and 778eV, respectively. Co^{+2} fitted peaks are located at 794 and 779eV, and Co^{+3} fitted peaks are located at 795.4 and 780eV.

In the fine scan of Fe 2p (see Figure 9-7d) spectra, the peaks of Fe 2p1/2 and Fe 2p3/2 can be observed at 721 and 708eV. Fitted peaks of Fe^{+3} are at 722 and 711eV, and the fitted peaks for Fe+2 are at 709eV.

A fine scan (Figure 9-7e) of Ni 2p spectra are deconvoluted into three peaks of Ni^{+3}, Ni^{+2}, and Ni. The tiny peak at 855eV belongs to Ni^{+3}, while the higher peak at 853eV is attributed to Ni^{+2}.

9.6 EDS maps

EDS analysis was performed on the HEPO of $La_{1-x}Ca_x(Cr_{0.2}Co_{0.2}Fe_{0.2}Mn_{0.2}Ni_{0.2})O_3$ sintered at 1400°C. The results are presented in Figure 9-8 and Table 9-4. The analysis showed complete dispersion of the dopants, Cr, Co, Fe, Mn, and Ni on the B-site equiatomic ratios and La and Ca on the A-site. The images from the EDS analysis confirmed that the doping was successful.
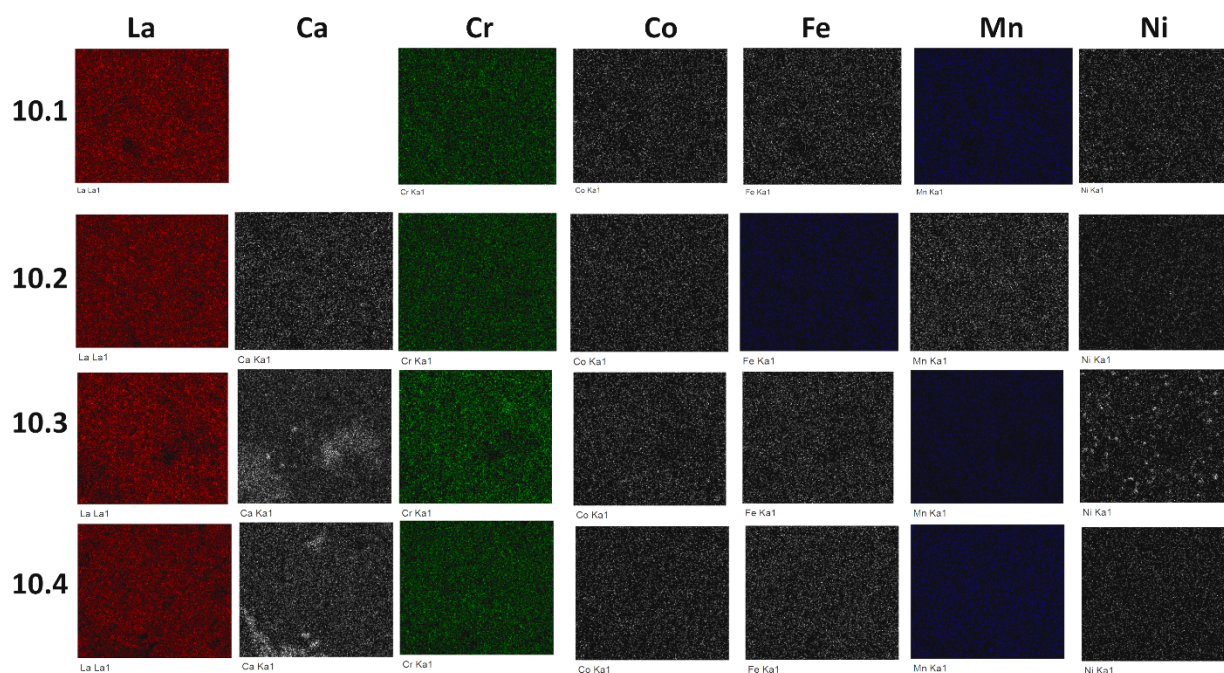
Figure 9-8 EDS elemental analysis of 10 $La_{1-x}Ca_x(Cr_{0.2}Co_{0.2}Fe_{0.2}Mn_{0.2}Ni_{0.2})O_3$ system sintered at 1400°C

Table 9-4 EDS analysis of system 10 sintered at 1400°C

HEPO sample	La (wt%)	Ca (wt%)	Cr (wt%)	Co (wt%)	Fe (wt%)	Mn (wt%)	Ni (wt%)
10.1	49	-	9.79	10.43	10.01	9.9	10.87
10.2	43.1	6.91	9.91	10.25	10.11	9.96	10.02
10.3	40.83	10.89	9.23	9.83	9.77	9.67	9.77
10.4	38.53	14.52	11.4	8.64	10.58	9.34	7

9.7 Conclusions

For the first time, the possibility of using a high-entropy approach to develop Ca-doped high-entropy perovskite oxides were investigated. This method demonstrated/showed potentiality to synthesize single-phase materials. A range of new $La_{1-x}Ca_x(Cr_{0.2}Co_{0.2}Fe_{0.2}Mn_{0.2}Ni_{0.2})O_3$ (with x values ranging from 0 to 0.3) perovskite-type oxides were created using modified PPM. This method of synthesis, which had not been used before for high-entropy perovskite oxides, enabled the production of nanosized powders of present compositions. Structural analysis shows the presence of phase-pure, Pnma structure in Ca-free and Ca-doped materials. The XRD and XPS data indicate that the charge compensation taking place as a result of addition of Ca into La lattice sites occur due the change of valence states of B-site elements. Additionally, XPS spectra confirmed the formation of various valence states of B-site elements. Samples of calcium-doped high-entropy perovskite oxide $La_{1-x}Ca_x (Cr_{0.2}Co_{0.2}Fe_{0.2}Mn_{0.2}Ni_{0.2})O_3$ prepared by PPM [70] are phase pure with orthorhombic perovskite structure. Sintered densities, electrical conductivities, and activation energies significantly improved after doping Ca with La. The measured electrical conductivity values of all materials at 800°C are in the range of 20-65 S/cm. The highest sintered density of 91% and electrical conductivity of 65 S/cm are observed for the sample with Ca^{+2} 30 mol%. The hopping of charge carriers along transition metal-oxygen bonds is responsible for electronic conduction in all materials, and it is improved by the creation of higher valence states of B-site cations through Ca^{+2} doping into the A-site. Electronic conduction in all materials occurs when charge carriers hop along the transition metal-oxygen bonds and is improved due to the creation of higher valence states of B-site cations as a result of Ca^{+2} doping into the A-site.

CHAPTER 10

CONCLUDING REMARKS

This dissertation presented a comprehensive investigation of various medium- and high-entropy perovskite oxide systems, aimed at gaining insights into the relationship between composition, Goldschmidt tolerance factor (GSTF), synthesis, material purity, sinterability, and electrical conductivity. The findings are summarized below.

10.1 MEPO and HEPO preparation and material purity

The modified polymerizable precursor technique was utilized to synthesize various MEPO and HEPO systems. Initial calcination at 850°C resulted in secondary phases, while increasing the calcination temperature to 950°C (for most of the materials) or 1050°C (for system 4 and sample 7.4) produced a single-phase material. Materials with 40 mol% Ca could not be synthesized as a single-phase material due to the insolubility of a high amount of Ca ($\geq$30 mol%) with La in the A-site.

10.2 Materials characterization, GSTF and crystal structure properties

Most of the synthesized powders showed an orthorhombic phase, except for the powders of systems 6 and 9. Under low calcium doping levels, systems 6 and 9 displayed a rhombohedral phase, but later transitioned to an orthorhombic structure as the Ca doping level increased. The addition of Ca reduced the unit cell volume, crystallite size, and pseudo cubic lattice constant, due to its smaller ionic radius compared to La in the same sublattice site. Ca doping also shifted the prominent XRD peak. Additionally, there is no observed correlation between the crystal structure predicted by modified GSTF and the crystal structure identified by XRD.

10.3 Sintering studies

A series of new MEPO and HEPO materials have been synthesized, and sintering mechanism, sintered density and average grain sizes have been presented. The sintered density of the pellets gradually increased with sintering temperature and Ca level. Only specific compositions with Ca on A-site produced fully dense pellets. The substitution of Ca facilitated the sintering process through transient liquid phase sintering, by forming a temperature-sensitive melting phase with B-site TM ions. No clear correlation is observed between grain size, sintering temperature, and Ca doping level.

10.4 Electrical conductivity

The electrical conductivity in the materials is believed to be due to the hopping of charge carriers along the B-site TM ions. With the exception of materials 6.4 and 9.4, all of the materials showed semiconductor behavior. For materials 6.4 and 9.4, the conductivity transitioned from a semiconductor to a metallic conductor at elevated temperatures (800-1000°C). The doping of Ca improved the electrical conductivity in most of the materials, but in certain materials (3.2, 4.2, and 7.4), it reduced the conductivity due to the trapping of charge carriers in the B-site TM ion pairs. Additionally, the doping of Ca with La increased the electrical conductivity of the MEPOs and HEPOs in the initial electrical conductivity temperature of 300°C as shown in Figure 10-1.

Figure 10-1 Electrical conductivity of MEPOs and HEPO in the range of 300-1000°C

Due to their exceptional electrical conductivity, sinterability, and stability during synthesis, these materials are suitable for further investigation as high temperature catalysts, oxygen sensors, interconnects, cathodes, and anodes in SOFCs, and solid oxide electrolysis cells (SOECs).

REFERENCES

[1] Yeh, J. W., Chen, S. K., Lin, S. J., Gan, J. Y., Chin, T. S., Shun, T. T., Tsau, C. H., and Chang, S. Y., 2004, "Nanostructured High-Entropy Alloys with Multiple Principal Elements: Novel Alloy Design Concepts and Outcomes," Adv. Eng. Mater., **6**(5), pp. 299-303+274.

[2] Cantor, B., Chang, I. T. H., Knight, P., and Vincent, A. J. B., 2004, "Microstructural Development in Equiatomic Multicomponent Alloys," Mater. Sci. Eng. A, **375**–**377**(1-2 SPEC. ISS.), pp. 213–218.

[3] Miracle, D. B., and Senkov, O. N., 2017, "A Critical Review of High Entropy Alloys and Related Concepts," Acta Mater., **122**, pp. 448–511.

[4] Murty, B. S., 2014, High-Entropy Alloys, Butterworth-Heinemann.

[5] Rost, C. M., Sachet, E., Borman, T., Moballegh, A., Dickey, E. C., Hou, D., Jones, J. L., Curtarolo, S., and Maria, J. P., 2015, "Entropy-Stabilized Oxides," Nat. Commun., **6**.

[6] Bérardan, D., Franger, S., Dragoe, D., Meena, A. K., and Dragoe, N., 2016, "Colossal Dielectric Constant in High Entropy Oxides," Phys. Status Solidi - Rapid Res. Lett., **10**(4), pp. 328–333.

[7] Bérardan, D., Franger, S., Meena, A. K., and Dragoe, N., 2016, "Room Temperature Lithium Superionic Conductivity in High Entropy Oxides," J. Mater. Chem. A, **4**(24), pp. 9536–9541.

[8] Zhao, Z., Xiang, H., Dai, F. Z., Peng, Z., and Zhou, Y., 2019, "$(La_{0.2}Ce_{0.2}Nd_{0.2}Sm_{0.2}Eu_{0.2})_2Zr_2O_7$: A Novel High-Entropy Ceramic with Low Thermal Conductivity and Sluggish Grain Growth Rate," J. Mater. Sci. Technol., **35**(11), pp. 2647–2651.

[9] Jiang, S., Hu, T., Gild, J., Zhou, N., Nie, J., Qin, M., Harrington, T., Vecchio, K., and Luo, J., 2018, "A New Class of High-Entropy Perovskite Oxides," Scr. Mater., **142**(February), pp. 116–120.

[10] Zhou, Y., Zhou, D., Jin, X., Zhang, L., Du, X., and Li, B., 2018, "Design of Non-Equiatomic Medium-Entropy Alloys," Sci. Rep., **8**(1), pp. 1–9.

[11] Zhang, R. Z., Gucci, F., Zhu, H., Chen, K., and Reece, M. J., 2018, "Data-Driven Design of Ecofriendly Thermoelectric High-Entropy Sulfides," Inorg. Chem., **57**(20), pp. 13027–13033.

[12] Wang, Q., Sarkar, A., Wang, D., Velasco, L., Azmi, R., Bhattacharya, S. S., Bergfeldt, T., Düvel, A., Heitjans, P., Brezesinski, T., Hahn, H., and Breitung, B., 2019, "Multi-Anionic and -Cationic Compounds: New High Entropy Materials for Advanced Li-Ion Batteries," Energy Environ. Sci., **12**(8), pp. 2433–2442.

[13] Dąbrowa, J., Olszewska, A., Falkenstein, A., Schwab, C., Szymczak, M., Zajusz, M., Moździerz, M., Mikuła, A., Zielińska, K., Berent, K., Czeppe, T., Martin, M., and Świerczek, K., 2020, "An Innovative Approach to Design SOFC Air Electrode Materials: High Entropy $La_{1-x}Sr_x(Co,Cr,Fe,Mn,Ni)O3-\delta(x = 0, 0.1, 0.2, 0.3)$ Perovskites Synthesized

by the Sol-Gel Method," J. Mater. Chem. A, **8**(46), pp. 24455–24468.

[14]   Witte, R., Sarkar, A., Kruk, R., Eggert, B., Brand, R. A., Wende, H., and Hahn, H., 2019, "High-Entropy Oxides: An Emerging Prospect for Magnetic Rare-Earth Transition Metal Perovskites," Phys. Rev. Mater., **3**(3), pp. 1–8.

[15]   Sarkar, A., Wang, Q., Schiele, A., Chellali, M. R., Bhattacharya, S. S., Wang, D., Brezesinski, T., Hahn, H., Velasco, L., and Breitung, B., 2019, "High-Entropy Oxides: Fundamental Aspects and Electrochemical Properties," Adv. Mater., **31**(26).

[16]   Cheng, J., Navrotsky, A., Zhou, X. D., and Anderson, H. U., 2005, "Thermochemistry of $La_{1-x}Sr_xFeO_{3-\delta}$ Solid Solutions ($0.0 \leq x \leq 1.0$, $0.0 \leq \delta \leq 0.5$)," Chem. Mater., **17**(8), pp. 2197–2207.

[17]   Minh, N. Q., 1993, "Ceramic Fuel Cells," J. Am. Ceram. Soc., **76**(3), pp. 563–588.

[18]   Kreuer, K. D., 2003, "Proton-Conducting Oxides," Annu. Rev. Mater. Res., **33**(1), pp. 333–359.

[19]   Wrighton, M. S., Ellis, A. B., Wolczanski, P. T., Morse, D. L., Abrahamson, H. B., and Ginley, D. S., 1976, "Strontium Titanate Photoelectrodes. Efficient Photoassisted Electrolysis of Water at Zero Applied Potential," J. Am. Chem. Soc., **98**(10), pp. 2774–2779.

[20]   Wang, Z., Cao, M., Zhang, Q., Hao, H., Yao, Z., Wang, Z., Song, Z., Zhang, Y., Hu, W., and Liu, H., 2015, "Dielectric Relaxation in Zr-Doped $SrTiO_3$ Ceramics Sintered in N2 with Giant Permittivity and Low Dielectric Loss," J. Am. Ceram. Soc., **98**(2), pp. 476–482.

[21]   Eerenstein, W., Mathur, N. D., and Scott, J. F., 2006, "Multiferroic and Magnetoelectric Materials," Nature, **442**(7104), pp. 759–765.

[22]   Goldschmidt, V. M., 1926, "Die Gesetze Der Krystallochemie," Naturwissenschaften, **14**(21), pp. 477–485.

[23]   Ramadass, N., 1978, "ABO3-Type Oxides-Their Structure and Properties-A Bird's Eye View," Mater. Sci. Eng., **36**(2), pp. 231–239.

[24]   Tanaka, H., and Misono, M., 2001, "Advances in Designing Perovskite Catalysts," Curr. Opin. Solid State Mater. Sci., **5**(5), pp. 381–387.

[25]   Yamazoe, N., and Teraoka, Y., 1990, "Oxidation Catalysis of Perovskites --- Relationships to Bulk Structure and Composition (Valency, Defect, Etc.)," Catal. Today, **8**(2), pp. 175–199.

[26]   Peña, M. A., and Fierro, J. L. G., 2001, "Chemical Structures and Performance of Perovskite Oxides," Chem. Rev., **101**(7), pp. 1981–2017.

[27]   Simner, S., Anderson, M., Bonnett, J., and Stevenson, J., 2004, "Enhanced Low Temperature Sintering of (Sr, Cu)-Doped Lanthanum Ferrite SOFC Cathodes," Solid State Ionics, **175**(1–4), pp. 79–81.

[28]   Cherif, K., Dhahri, J., Vincent, H., Zemni, S., Dhahri, E., and Oumezzine, M., 2002, "X-

Ray Diffraction, Magnetic and Electrical Properties in the Manganites $(La_{1-x}Nd_x)_{0.7}Sr_{0.3}MnO_3$," Physica B: Condensed Matter, North-Holland, pp. 48–53.

[29] Kolotygin, V. A., Tsipis, E. V, Patrikeev, M. V, Ivanov, A. I., and Kharton, V. V, 2016, "Stability, Mixed Conductivity, and Thermomechanical Properties of Perovskite Materials for Fuel Cell Electrodes Based on $La_{0.5}A_{0.5}Mn_{0.5}Ti_{0.5}O_{3-\delta}$, $La_{0.5}Ba_{0.5}Ti_{0.5}Fe_{0.5}O_{3-\delta}$, and $(La_{0.5}A_{0.5})_{0.95}Cr_{0.5}Fe_{0.5}O_{3-\delta}$ (A = Ca, Ba)," Russ. J. Electrochem., **52**(7), pp. 628–641.

[30] Rodriguez-Martinez, L. M., Ehrenberg, H., and Attfield, J. P., 2000, "Disorder Effects on Structural and Electronic Transitions in High Tolerance Factor Manganite Perovskites," Solid State Sci., **2**(1), pp. 11–16.

[31] Ecija, A., Vidal, K., Larrañaga, A., Martínez-Amesti, A., Ortega-San-Martín, L., and Arriortua, M. I., 2011, "Characterization of $Ln_{0.5}M_{0.5}FeO_{3-\delta}$ (Ln = La, Nd, Sm; M = Ba, Sr) Perovskites as SOFC Cathodes," Solid State Ionics, **201**(1), pp. 35–41.

[32] Richter, J., Holtappels, P., Graule, T., Nakamura, T., and Gauckler, L. J., 2009, "Materials Design for Perovskite SOFC Cathodes," Monatshefte für Chemie - Chem. Mon., **140**(9), pp. 985–999.

[33] Duan, C., Tong, J., Shang, M., Nikodemski, S., Sanders, M., Ricote, S., Almansoori, A., and O'Hayre, R., 2015, "Readily Processed Protonic Ceramic Fuel Cells with High Performance at Low Temperatures," Science (80-.)., **349**(6254), pp. 1321–1326.

[34] Gorte, R. J., 2015, "Cooling down Ceramic Fuel Cells," Science (80-.)., **349**(6254), p. 1290.

[35] Yang, L., Wang, S., Blinn, K., Liu, M., Liu, Z., Cheng, Z., and Liu, M., 2009, "Enhanced Sulfur and Coking Tolerance of a Mixed Ion Conductor for SOFCs: $BaZr_{0.1}Ce_{0.7}Y_{0.2}Yb_xO_3$" Science (80-.)., **326**(5949), pp. 126–129.

[36] Zinkevich, M., and Aldinger, F., 2004, "Thermodynamic Analysis of the Ternary La–Ni–O System," J. Alloys Compd., **375**(1–2), pp. 147–161.

[37] Chiba, R., Yoshimura, F., and Sakurai, Y., 1999, "An Investigation of $LaNi_{1-x}Fe_xO_3$ as a Cathode Material for Solid Oxide Fuel Cells," Solid State Ionics, **124**(3), pp. 281–288.

[38] Tsipis, E. V, Kiselev, E. A., Kolotygin, V. A., Waerenborgh, J. C., Cherepanov, V. A., and Kharton, V. V, 2008, "Mixed Conductivity, Mössbauer Spectra and Thermal Expansion of $(La,Sr)(Fe,Ni)O_{3-\delta}$ Perovskites," Solid State Ionics, **179**(38), pp. 2170–2180.

[39] Kononyuk Tolochko, S.P., Surmach, N.G., I. F., 1986, "Production and Electrical Properties of $La_{1-x}Ca_xCr_{1-Y}Ni_yO3$," Neorg Mater, **22**, p. 98.

[40] Weber, A., and Ivers-Tiffée, E., 2004, "Materials and Concepts for Solid Oxide Fuel Cells (SOFCs) in Stationary and Mobile Applications," J. Power Sources, **127**(1–2), pp. 273–283.

[41] Takeda Ryoji; Noda, Muneyoshi; Yamamoto, Y. K., and Osamu, 1986, "Perovskite Electrodes for High Temperature Solid Electrolyte Cells," Bull. Inst. Chem. Res. Kyoto Univ., **64**(4), pp. 157–169.

[42] Orlovskaya, N., Lugovy, M., Pathak, S., Steinmetz, D., Lloyd, J., Fegely, L., Radovic, M., Payzant, E. A., Lara-Curzio, E., Allard, L. F., and Kuebler, J., 2008, "Thermal and mechanical properties of $LaCoO_3$ and $La_{0.8}Ca_{0.2}CoO_3$ perovskites," J. Power Sources, **182**(1), pp. 230–239.

[43] Ralph, J., Rossignol, C., and Kumar, R., 2003, "Cathode Materials for Reduced-Temperature SOFCs," J. Electrochem. Soc., **150**(11), pp. A1518–A1522.

[44] Simner, S. P., Bonnett, J. F., Canfield, N. L., Meinhardt, K. D., Sprenkle, V. L., and Stevenson, J. W., 2002, "Optimized Lanthanum Ferrite-Based Cathodes for Anode-Supported SOFCs," Electrochem. Solid-State Lett., **5**(7), pp. A173–A175.

[45] Koc, R., and Anderson, H. U., 1995, "Electrical and Thermal Transport Properties of $(La,Ca)(Cr,Co)O_3$," J. Eur. Ceram. Soc., **15**(9), pp. 867–874.

[46] Bongio, E. V, Black, H., Raszewski, F. C., Edwards, D., McConville, C. J., and Amarakoon, V. R. W., 2005, "Microstructural and High-Temperature Electrical Characterization of $La_{1-x}Sr_xFeO_{3-\delta}$," J. electroceramics, **14**(3), pp. 193–198.

[47] Zhou XD, A. H. U., 2005, "SOFC-IX: Solid Oxide Fuel Cells," Electrochem. Soc. Proc., pp. 1479–1486.

[48] Dusastre, V., and Kilner, J. A., 1999, "Optimisation of Composite Cathodes for Intermediate Temperature SOFC Applications," Solid State Ionics, **126**(1–2), pp. 163–174.

[49] Waller, D., Lane, J. A., Kilner, J. A., and Steele, B. C. H., 1996, "The Effect of Thermal Treatment on the Resistance of LSCF Electrodes on Gadolinia Doped Ceria Electrolytes," Solid State Ionics, **86**, pp. 767–772.

[50] L. Kindermann H. Nickel, K. Hilpert, C. C. Appel and F. W. Poulson, D. Das, 1997, "Chemical Compatibility of ($La_{0.6}Ca_{0.4})_xFe_{0.8}M_{0.2}O_3$ with Yttria-Stabilized Zirconia," J. Electrochem. Soc., **144**(2), pp. 717–720.

[51] Steele, B. C. H., 2000, "Appraisal of $Ce_{1-y}Gd_yO_{2-y/2}$ Electrolytes for IT-SOFC Operation at 500°C," Solid State Ionics, **129**(1–4), pp. 95–110.

[52] Kostogloudis, G. C., and Ftikos, C., 1999, "Properties of A-Site-Deficient $La_{0.6}Sr_{0.4}Co_{0.2}Fe_{0.8}O_{3-\delta}$-Based Perovskite Oxides," Solid State Ionics, **126**(1–2), pp. 143–151.

[53] Koc, R., Anderson, H.U., 1992, "Liquid Phase Sintering of $LaCrO_3$," J. Eur. Ceram. Soc, **9**(4), pp. 285–292.

[54] E. Konyshevaa E. Wessela, J. Mertensb, U. Seelingc, L. Singheisera and K. Hilperta,z, H. P., 2006, "Chromium Poisoning of Perovskite Cathodes by the ODS Alloy $Cr_5Fe_1Y_2O_3$ and the High Chromium Ferritic Steel Crofer22APU," J. Electrochem. Soc, **153**(4), pp. A765–A773.

[55] Zhu, W. Z., and Deevi, S. C., 2003, "Development of Interconnect Materials for Solid Oxide Fuel Cells," Mater. Sci. Eng. A, **348**(1–2), pp. 227–243.

[56] Koc, R., and Anderson, H. U., 1992, "Investigation of Strontium-Doped La(Cr, Mn)O$_3$ for Solid Oxide Fuel Cells," J. Mater. Sci., **27**(21), pp. 5837–5843.

[57] Ghosh, S., Sharma, A. Das, Basu, R. N., and Maiti, H. S., 2007, "Influence of B Site Substituents on Lanthanum Calcium Chromite Nanocrystalline Materials for a Solid-Oxide Fuel Cell," J. Am. Ceram. Soc., **90**(12), pp. 3741–3747.

[58] Ozcan, S., and Koc, R., 2006, "Microstructure and Electrical Conductivity Studies of (La, Sr)(Cr, Mn, Co)O$_3$," Developments in Solid Oxide Fuel Cells and Lithium Ion Batteries, John Wiley & Sons, Ltd, pp. 13–20.

[59] Kolisetty, A., 2016, "Development of Interconnect and Cathode Material for SOFC."

[60] Gajjala, S. R., Fu, Z., and Koc, R., 2019, "Investigation of (La$_{1-x}$,Ca$_x$)(Ni$_{0.25}$Fe$_{0.25}$Cr$_{0.25}$ Co$_{0.25}$)O$_3$ For Solid Oxide Fuel Cells Cathode Materials," John Wiley & Sons, Ltd, pp. 85–97.

[61] Zenati, R., Bernard, C., Calmet, C., Guillemet, S., Fantozzi, G., and Durand, B., 2005, "Internal Friction Investigation of Phase Transformation in Nearly Stoichiometric LaMnO3+δ," J. Eur. Ceram. Soc., **25**(6), pp. 935–941.

[62] Kumar, M. D. S., Srinivasan, T. M., Ramasamy, P., and Subramanian, C., 1995, "Synthesis of Lanthanum Aluminate by a Citrate-Combustion Route," Mater. Lett., **25**(3–4), pp. 171–174.

[63] Hong, L., Guo, F., and Lin, J., 1999, "From Chelating Precursors to La$_{0.05}$Sr$_{0.95}$CoO$_{3-y}$ Oxide," Mater. Res. Bull., **34**(12), pp. 1943–1958.

[64] Garrido Pedrosa, A. M., Souza, M. J. B., Marinkovic, B. A., Melo, D. M. A., and Araujo, A. S., 2008, "Structure and Properties of Bifunctional Catalysts Based on Zirconia Modified by Tungsten Oxide Obtained by Polymeric Precursor Method," Appl. Catal. A Gen., **342**(1–2), pp. 56–62.

[65] Silva, G. R. O., Santos, J. C., Martinelli, D. M. H., Pedrosa, A. M. G., de Souza, M. J. B., and Melo, D. M. A., 2010, "Synthesis and Characterization of LaNi$_x$Co$_{1-x}$O$_3$ Perovskites via Complex Precursor Methods," Mater. Sci. Appl., **01**(02), pp. 39–45.

[66] Zhou, D., Huang, G., Chen, X., Xu, J., and Gong, S., 2004, "Synthesis of LaAlO$_3$ via Ethylenediaminetetraacetic Acid Precursor," Mater. Chem. Phys., **84**(1), pp. 33–36.

[67] Huang, Y. H., Xu, Z. G., Yan, C. H., Wang, Z. M., Zhu, T., Liao, C. S., Gao, S., and Xu, G. X., 2000, "Soft Chemical Synthesis and Transport Properties of La$_{0.7}$Sr$_{0.3}$MnO$_3$ Granular Perovskites," Solid State Commun., **114**(1), pp. 43–47.

[68] Popa, M., and Kakihana, M., 2002, "Synthesis of Lanthanum Cobaltite (LaCoO$_3$) by the Polymerizable Complex Route," Solid State Ionics, Elsevier, pp. 251–257.

[69] Nakayama, S., Okazaki, M., Aung, Y. L., and Sakamoto, M., 2003, "Preparations of Perovskite-Type Oxides LaCoO$_3$ from Three Different Methods and Their Evaluation by Homogeneity, Sinterability and Conductivity," Solid State Ionics, **158**(1–2), pp. 133–139.

[70] Pechini, M. P., 1967, "Method of Preparing Lead and Alkaline Earth Titanates and

Niobates and Coating Method Using the Same to Form a Capacitor."

[71] Campagnoli, E., Tavares, A., Fabbrini, L., Rossetti, I., Dubitsky, Y. A., Zaopo, A., and Forni, L., 2005, "Effect of Preparation Method on Activity and Stability of $LaMnO_3$ and $LaCoO_3$ Catalysts for the Flameless Combustion of Methane," Appl. Catal. B Environ., **55**(2), pp. 133–139.

[72] Liu, S., Tan, X., Li, K., and Hughes, R., 2002, "Synthesis of Strontium Cerates-Based Perovskite Ceramics via Water-Soluble Complex Precursor Routes," Ceram. Int., **28**(3), pp. 327–335.

[73] Leontiou, A. A., Ladavos, A. K., and Pomonis, P. J., 2003, "Catalytic NO Reduction with CO on $La_{1-x}Sr_x(Fe^{3+}/Fe^{4+})O_{3\pm\delta}$ Perovskite-Type Mixed Oxides (x = 0.00, 0.15, 0.30, 0.40, 0.60, 0.70, 0.80, and 0.90)," Appl. Catal. A Gen., **241**(1–2), pp. 133–141.

[74] Kleveland, K., Einarsrud, M. A., and Grande, T., 2000, "Sintering of $LaCoO_3$ Based Ceramics," J. Eur. Ceram. Soc., **20**(2), pp. 185–193.

[75] Kumar, A., Devi, P. S., and Maiti, H. S., 2006, "Effect of Metal Ion Concentration on Synthesis and Properties of $La_{0.84}Sr_{0.16}MnO_3$ Cathode Material," J. Power Sources, **161**(1), pp. 79–86.

[76] Debye, P., and Scherrer, P., 1916, "Interference of Irregularly Oriented Particles in X-Rays," Phys. Zeit, **17**, pp. 277–283.

[77] Ullmann, H., Trofimenko, N., Tietz, F., Stöver, D., and Ahmad-Khanlou, A., 2000, "Correlation between Thermal Expansion and Oxide Ion Transport in Mixed Conducting Perovskite-Type Oxides for SOFC Cathodes," Solid State Ionics, **138**(1–2), pp. 79–90.

[78] Trofimenko, N., and Ullmann, H., 1999, "Transition Metal Doped Lanthanum Gallates," Solid State Ionics, **118**(3–4), pp. 215–227.

[79] Shannon, R. D., 1976, "Revised Effective Ionic Radii and Systematic Studies of Interatomic Distances in Halides and Chalcogenides," Acta Crystallogr. Sect. A, **32**(5), pp. 751–767.

[80] Hung, M.-H., Rao, M. V. M., and Tsai, D.-S., 2007, "Microstructures and Electrical Properties of Calcium Substituted $LaFeO_3$ as SOFC Cathode," Mater. Chem. Phys., **101**(2), pp. 297–302.

[81] Yokokawa, H., Sakai, N., Kawada, T., and Dokiya, M., 1992, "Thermodynamic Stabilities of Perovskite Oxides for Electrodes and Other Electrochemical Materials," Solid State Ionics, **52**(1–3), pp. 43–56.

[82] Mori, M., Hiei, Y., and Sammes, N. M., 2000, "Sintering Behavior of Ca- or Sr-Doped $LaCrO_3$ Perovskites Including Second Phase of $AECrO_4$ (AE = Sr, Ca) in Air," Solid State Ionics, **135**(1–4), pp. 743–748.

[83] Chick, L. A., Liu, J., Stevenson, J. W., Armstrong, T. R., McCready, D. E., Maupin, G. D., Coffey, G. W., and Coyle, C. A., 1997, "Phase Transitions and Transient Liquid-Phase Sintering in Calcium-Substituted Lanthanum Chromite," J. Am. Ceram. Soc., **80**(8), pp. 2109–2120.

[84] German, R. M., Suri, P., and Park, S. J., 2009, "Review: Liquid Phase Sintering," J. Mater. Sci., **44**(1), pp. 1–39.

[85] Konysheva, E., Irvine, J. T. S., and Besmehn, A., 2008, "Electrical Conductivity and Structure of Solid Solutions Formed in the $La_{0.8}Sr_{0.2}MnO_3$-$La_{0.95}Ni_{0.6}Fe_{0.4}O_3$ System," Solid State Ionics, **179**(27–32), pp. 1432–1435.

[86] Abbas, S. K., Atiq, S., Riaz, S., and Naseem, S., 2017, "Thermally Activated Variations in Conductivity and Activation Energy in $SrMnO_3$," J. Mater. Sci. Mater. Electron., **28**(10), pp. 7171–7176.

[87] Yáng, Z., Harvey, A. S., Infortuna, A., Schoonman, J., and Gauckler, L. J., 2011, "Electrical Conductivity and Defect Chemistry of $Ba_xSr_{1-x}Co_yFe_{1-y}O_3$ perovskites," J. Solid State Electrochem., **15**(2), pp. 277–284.

[88] Ciambelli, P., Cimino, S., Lisi, L., Faticanti, M., Minelli, G., Pettiti, I., and Porta, P., 2001, "La, Ca and Fe Oxide Perovskites: Preparation, Characterization and Catalytic Properties for Methane Combustion," Appl. Catal. B Environ., **33**(3), pp. 193–203.

[89] Kong, L., and Shen, Y., 1996, "Gas-Sensing Property and Mechanism of $Ca_xLa_{1-x}FeO_3$ Ceramics," Sensors Actuators B Chem., **30**(3), pp. 217–221.

[90] Taguchi, H., Masunaga, Y., Hirota, K., and Yamaguchi, O., 2005, "Synthesis of Perovskite-Type $(La_{1-x}Ca_x)FeO_3$ ($0 \leq x \leq 0.2$) at Low Temperature," Mater. Res. Bull., **40**(5), pp. 773–780.

[91] Raffaelle, R., Anderson, H. U., Sparlin, D. M., and Parris, P. E., 1990, "Evidence for a Crossover from Multiple Trapping to Percolation in the High-Temperature Electrical Conductivity of Mn-Doped $LaCrO_3$" Phys. Rev. Lett., **65**(11), pp. 1383–1386.

[92] Tai, L.-W., Nasrallah, M. M., Anderson, H. U., Sparlin, D. M., and Sehlin, S. R., 1995, "Structure and Electrical Properties of $La_{1-x}Sr_xCo_{1-y}Fe_yO_3$. Part 1. The System $La_{0.8}Sr_{0.2}Co_{1-y}Fe_yO_3$," Solid State Ionics, **76**(3), pp. 259–271.

[93] Raffaele, R., Anderson, H. U., Sparlin, D. M., and Parris, P. E., 1991, "Transport Anomalies in the High-Temperature Hopping Conductivity and Thermopower of Sr-Doped $La(Cr, Mn)O_3$," Phys. Rev. B, **43**(10).

[94] Sehlin, S. R., Anderson, H. U., and Sparlin, D. M., 1995, "Electrical Characterization of the $(La,Ca)(Cr,Co)O_3$ System," Solid State Ionics, **78**(3), pp. 235–243.

[95] DeBarr, M. J., 1991, "Investigation of the Conduction Mechanism in $La_{1-y}Ca_yAl_{1-x}Mn_xO_3$."

[96] Chiba, R., Yoshimura, F., and Sakurai, Y., 1999, "An Investigation of $LaNi_{1-x}Fe_xO_3$ as a Cathode Material for Solid Oxide Fuel Cells," Solid State Ionics, **124**(3), pp. 281–288.

[97] Lin, B., Wang, S., Liu, X., and Meng, G., 2010, "Simple Solid Oxide Fuel Cells," J. Alloys Compd., **490**(1), pp. 214–222.

[98] Kim, S., Yang, Y. L., Christoffersen, R., and Jacobson, A. J., 1997, "Oxygen Permeation, Electrical Conductivity and Stability of the Perovskite Oxide $La_{0.2}Sr_{0.8}Cu_{0.4}Co_{0.6}O_{3-\delta}$,"

Solid State Ionics, **104**(1), pp. 57–65.

[99]   Karim, D. P., and Aldred, A. T., 1979, "Localized Level Hopping Transport in La(Sr)CrO$_3$" Phys. Rev. B, **20**(6), pp. 2255–2263.

[100] King, H. W., Castelliz, K. M., Murphy, G. J., and Rizkalla, A., 1986, "Crystal structure and electrical resistivity of ceramics with compositions La$_2$MO$_4$, La$_{1.5}$Sr$_{0.5}$MO$_4$ AND LaSrMO$_4$.," J. Can. Ceram. Soc., **55**, pp. 10–14.

[101] Thornton, G., Tofield, B. C., and Williams, D. E., 1982, "Spin State Equilibria and the Semiconductor to Metal Transition of LaCoO$_3$," Solid State Commun., **44**(8), pp. 1213–1216.

[102] Mizusaki, J., Tabuchi, J., Matsuura, T., Yamauchi, S., and Fueki, K., 1989, "Electrical Conductivity and Seebeck Coefficient of Nonstoichiometric La$_{1-x}$Sr$_x$CoO$_{3-\delta}$," J. Electrochem. Soc., **136**(7), pp. 2082–2088.

[103] Sarma, D. D., and Chainani, A., 1994, "Electronic Structure of Perovskite Oxides, LaMO$_3$ (M = Ti-Ni), from High-Energy Electron Spectroscopic Investigations," J. Solid State Chem., **111**(1), pp. 208–216.

[104] Petitjean, M., Caboche, G., Siebert, E., Dessemond, L., and Dufour, L.-C., 2005, "(La$_{0.8}$Sr$_{0.2}$)(Mn$_{1-y}$Fe$_y$)O$_{3\pm\delta}$ Oxides for ITSOFC Cathode Materials?: Electrical and Ionic Transport Properties," J. Eur. Ceram. Soc., **25**(12), pp. 2651–2654.

[105] Khan, W., Naqvi, A. H., Gupta, M., Husain, S., and Kumar, R., 2011, "Small Polaron Hopping Conduction Mechanism in Fe Doped LaMnO$_3$," J. Chem. Phys., **135**(5), pp. 1–7.

VITA

Graduate School
Southern Illinois University Carbondale

Sai Ram Gajjala

Sairam.gajjala@gmail.com

Jawaharlal Nehru Institute of Technology Hyderabad
Bachelor of Technology, Mechanical Engineering, May 2014

Southern Illinois University Carbondale
Master of Science in Mechanical Engineering, May 2017

Dissertation Paper Title:
    Synthesis, sintering, and electronic conductivity studies of medium- and high-entropy
    perovskite oxides

Major Professor: Rasit Koc